Compatibility of Reduced Activation Ferritic/Martensitic Steel with Liquid Lithium

Xu, Qi

Doctor of Philosophy

Department of Fusion Science

School of Physical Sciences

The Graduate University for Advanced Studies

2008

.

Abstract

Development of breeding and structural materials for blankets is the key issue of fusion reactors. Fe-Cr-W based RAFM (Reduced Activation Ferritic/Martensite) steels are widely regarded as promising blanket structural materials, because of its low activation properties, radiation resistance and industrial maturity. Blanket concepts with liquid lithium (Li) breeder/coolant provide attractive options for high tritium breeding ratio, high efficiency and simplicity of blanket system.

One of the critical issues for RAFM/Li blanket is the compatibility of RAFM steel with liquid Li. As to the corrosion of ferritic steels in Li, only studies on conventional Fe-Cr-Mo are available. In those studies, however, investigation on microstructure and micro-chemical processes are quite limited. Any data are not available for RAFM (Fe-Cr-W) steels yet.

The purpose of the present study is to examine the compatibility of RAFM steels with liquid Li with respect to corrosion rate and the degradation of mechanical properties and to classify the underlying mechanism based on the element transfer and change of microstructure during the corrosion process.

In this study, the compatibility of JLF-1(Fe-9Cr-2W-0.1C), a RAFM steel developed in Japan, with static and flowing Li was investigated. The coupon specimens (16×4×0.25mm) were exposed in an isothermal pot for static tests and thermal convection SS316 (Fe-Cr-Ni) loop for flowing tests. After exposure, the corrosion characteristics were examined by fine scale weight measurement, SEM/EDS (Scanning Electron Microscope/Energy Dispersive X-ray Spectrometer), TEM (Transmission Electron Microscopy) and Vickers hardness test.

In the static test, the weight loss of JLF-1 specimens increased with temperature. After exposure at 700ºC for 100h, JLF-1 specimens suffered severe corrosion and the corrosion rate was 0.18mm/yr. The kinetics of weight loss at temperature of 500ºC and 600 ºC showed that the corrosion of JLF-1 became saturated with the exposure time. This is possibly due to the formation of saturated layer of dissolved elements in liquid

lithium near the specimen surface. In the corrosion test in a thermal convection loop, the corrosion rate at 500ºC for 250h was significantly larger than that obtained in the static test in an identical condition. After Li exposure, the phase transformation from martensite to ferrite was found on the samples. This is the first time that the phase change from martensite to ferrite is observed after Li attack. The chemical analysis results and the depletion of carbides suggested that the phase change should be caused by the depletion of carbon. At the same time, selective depletion of other alloy elements, such as Cr and W, was detected by EDS on the surface. Vickers hardness results showed that obvious softening occurred on the surface of the specimens after Li exposure and the depth of the softened region was consistent with that of the phase transformation. The flowing Li enhanced the weight loss, phase change and reduction of hardness due to the mass transfer effect.

The influence of alloy composition on the corrosion was investigated by comparing the corrosion behavior of JLF-1, binary Fe-Cr and pure iron at 700°C for 100hr. The corrosion of JLF-1 is more significant than that of Fe-9Cr and pure iron at 973K. The selective dissolution of Cr, W and C into lithium seems to enhance the corrosion. Significant phase transformation from martensite to ferrite to the depth of 100μm was observed on the JLF-1 specimens after exposure in Li at 700°C for 100h. The phase change resulted in drastic hardness drop from 250 to 140Hv. For the Fe-9Cr, the softened layer (~5μm) was found on the surface of the specimen after Li attack due to the depletion of Cr and W. This was verified by the EDS line scan on the cross section of specimens. No mechanical change was observed on the pure Fe specimen before and after exposure.

To study the influence of container materials, the coupon specimens of JLF-1 were exposed in Mo, SS316 and Nb crucibles separately at 600°C for 250h. The corrosion characteristics in different crucible were compared. After exposure, the specimens exposed in Mo and Nb crucible lost weight, while the specimens in SS316 crucible gained weight due to the precipitation of Ni dissolved from crucible materials. The phase transformation was observed on cross section of specimens exposed in Nb

crucible (~20μm) and Mo crucible (~10μm). No phase change was found in the case of SS316 container. The phase change caused a corresponding reduction of hardness on JLF-1 samples in depth. It is clear that the Nb container enhanced the depletion of carbon and the phase transformation by trapping C and achieving a very low C concentration in Li.

Analysis of the experimental results was carried out based on the thermodynamic and kinetic modeling. The results showed that the driving force of corrosion is the level of Fe and Cr in Li. Saturation of those elements in Li results in the suppression of corrosion. However, production of compounds of N, Li and alloy elements was shown to determine the level of Fe and Cr in Li. The loss of C leads to the phase change. The driving force of decarburization is the level of C in Li. The trapping of C by the container materials can enhance the phase transformation. The diffusion of C in the martensite controls the extension of phase change region.

In conclusion, expected influences of Li attack to RAFM steel are the loss of materials by dissolution of the constituent elements and the degradation of mechanical properties caused by phase transformation from martensite to ferrite as the result of dissolution of C. Based on the data obtained, the compatibility of RAFM steel in Li seems not to be a serious issue once the level of N in Li is kept low. The phase transformation will be reduced by avoiding the use of materials which has high affinity with C.

CONTENTS

Chapter 1

Introduction

1.1 Fusion reactor and blanket system

1.1.1 The energy crisis and fusion

Energy is essential in modern society. It was used everywhere, lighting, heating transport, industry and agriculture. At present, around 80% energy is produced by burning the fossil fuels, some come from the nuclear fission, and a few amount come from the renewable energy source, such as hydro, solar and wind.[1]

Following the growth of the world's population and the rising of living standards in many developing countries, the worldwide energy demand will increase in the coming decades. However, the burning of the fossil fuel releases CO_2, which is pointed out to result in global warming and climate change. The nuclear fission faces the problem of the radioactive waste with long half time. The development of renewable resources cannot meet the demand of energy. Furthermore supplement of fossil fuels is limited. It was predicted by Donald L. Klass [2] that oil reserves will be used up within 20-70 years at an annual growth rate of 2.3% in consumption and 30-70 years for the natural gas at an annual growth rate of 3.2%.

The depletion of worldwide resources will inevitably lead the political instability and conflict. The global warming caused by emission of green house gases could lead to environmental disaster. Sustained development of human being requires a safe and long term energy resource. The controlled fusion seems to be a promising answer to these demands. [3-5] The advantages of the fusion reactor include:

• The basic fuels (deuterium and tritium) are abundant everywhere;

• No greenhouse gas emissions;

• Day-to-day operation of a fusion power station does not require the transport of radioactive materials;

• Fusion power stations can be made inherently safe. "Runaway" or "meltdown" accidents are impossible; and

• Waste will not prove to be a long-term burden on future generations.

1.1.2 Fusion reaction

Nuclear fusion is a process where two or more nuclei combine to form an element with a higher atomic number (more protons in the nucleus). Fig.1.1-1 shows the reaction between deuterium and tritium. Fusion of light elements (the reactants) into heavier elements (the products) releases energy, (as does fission of heavy elements into lighter elements). For fusion, the energy release occurs when the total mass of the fusion products is smaller than the reactants. The difference between the total masses of all the protons and neutrons of a nucleus and the mass of the nucleus itself can be expressed in terms of the binding energy. The energy released is proportional to the difference in the masses as predicted by Einstein's famous equation,

$$E = mc^2. \tag{1.1-1}$$

where E is energy, m is mass and c is the speed of light (3×10^8m/ sec.).
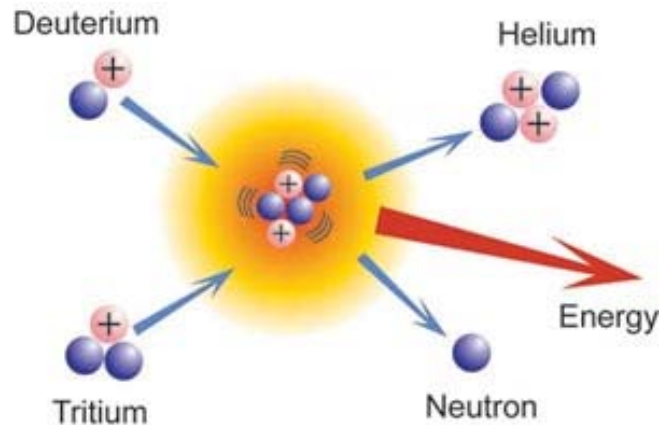

Fig.1.1-1 The D-T fusion reaction, is the most efficient reaction known in terms of energy released (*from ITER homepage*)

There are many kinds of fusion reactions, practical ones for energy nowadays are shown in Fig. 1.1-2.[6] The figure indicates that the most effective reaction occurs between deuterium (D) and tritium (T), at the lowest ignition temperature, because D-T

reaction has the largest fusion cross-section among the reactions.

Reaction		Ignition Temperature		Output Energy
Fuel	Product	(millions of °C)	(keV)	(keV)
D + T	⁴He + n	220	20	17,600
D + ³He	⁴He + p	350	30	18,300
D + D	³He + n	400	35	~4,000
	T + p	400	35	~4,000

Fig. 1.1-2 Different fusion reactions require different temperatures and have different energy yields

To achieve a fusion reaction, it is necessary to bring the reactants so close together that nuclear forces become important and "glue" the reactants together. But, the distance of interaction of the nuclear force is very small (10^{-15} meters), and the reactants (positively charged nuclei) repel each other because of the electrostatic force. For these reasons fusion most easily occurs in a high density, and high temperature environment.

On Earth, nuclear fusion was reached first in the explosion of the Hydrogen bomb. In a non-destructive manner, fusion has also been reached in different experimental devices aimed at studying the possibility of producing energy in a controlled fashion. The D-T reaction is presently the best candidate for implementing a controlled fusion power station in the near future.

There are several experiments worldwide where the conditions for nuclear fusion reactions have been achieved in a controlled manner. The two main methods are being explored are Magnetic Confinement Fusion (MCF) and Inertial Confinement Fusion (ICF). [7]

1) In MCF, a (Deuterium-Tritium) plasma is kept confined (typically within a doughnut shaped container) by a strong magnetic field and heated up to temperatures where the fusion reactions start to occur at a significant rate.

2) In ICF, high-energy lasers impact and compress a solid (frozen) Deuterium-Tritium pellet producing an implosion that eventually raises the temperature of the pellet (that has become plasma) enough to trigger nuclear fusion reactions.

These two methods are quiet different in the standpoint of physics or engineering. Here only the research works on MCF are introduced.

1.1.3 Fusion reactor

To realize the MCF, several devices were developed, such as Tokamak, Stellarator and Magnetic Mirror etc. In a Tokamak device, the magnetic field confines the plasma within a torus vessel and keeps the high-temperature plasma away from the vessel wall. The research on Tokamak principle have been performed widely and got many achievements, such as TFTR in the U.S [8,9], JET in Europe [10] and JT-60U in Japan [11], et al. Now a great effort is being made on a Tokamak type International Thermonuclear Experimental Reactor (ITER).[12,13] Fig. 1.1-3 shows the cutaway of ITER.

The function of parts or system in ITER is:

1) First wall

First wall directly faces the plasma and protect other components, such as blanket and vacuum system. It suffers from the high flux of heat and neutron. Because the impurities produced by sputtering of plasma poison the plasma, the choice of first wall materials is still a concern. The candidates for first wall are low Z materials C and high Z materials W.
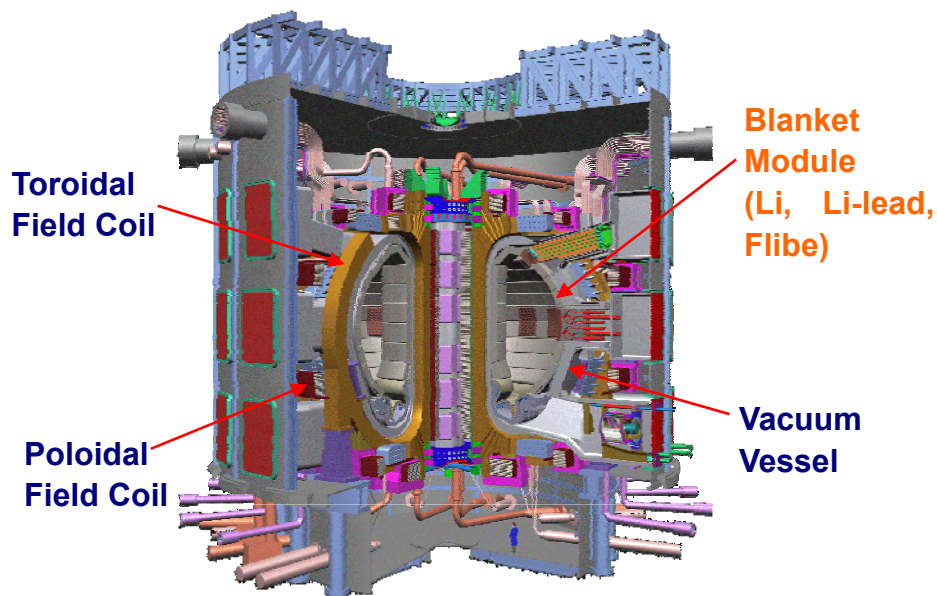
Fig. 1.1-3 ITER Tokamak cutaway (*from ITER homepag*e)

2) Divertor

The function of divertor is to remove the impurities and fusion product helium. These particles are guided by the magnetic field to divertor. After neutralization, the fusion wastes are derived out by pump. Considering the high heat flux, the W may be the most promising candidate materials for divertor. The concepts of liquid metal divertor were proposed [14], but it still faces some technical problems.

3)   Vacuum vessel

Vacuum vessel provides high vacuum boundary for the plasma and the first line of confinement against radioactive release within the vessel. Very high vacuum is achieved to prevent the impact of plasma. At the same time, vacuum system should be strong enough to support the first wall, blanket and divertor inside.

4)   Superconducting magnet systems,

Superconducting magnet system include the toroidal field (TF) coil, poloidal field (PF) coil and central solenoid (CS) coil, produce a strong magnetic field to confine the plasma. In ITER the predicted maximum magnetic field is 13T, the candidate of coil

material is Nb_3Sn. [15]

5) Cryostat

The Cryostat is used to ultra-low temperature to superconducting magnet.

6) Blanket

In real fusion reactor, the 80% heat is released by neutron after the D-T reaction. The blanket transforms the neutron energy to heat and transports the heat to the outside. Furthermore, the fuel to fusion reaction, tritium, is produced in blanket. To achieve the above purposes, the blanket consists in breeder, coolant, neutron multiplier. The structure materials of blanket are the main concern of this work. It will be discussed in detail later. ITER will have only "shield blanket". DEMO blanket concept will be tested in ITER as ITER Test Blanket Module (TBM).

The ultimate goals of ITER are to demonstrate ignition and extended burns of D-T plasmas with steady-state and serve as a test facility for advanced components such as blankets [16]. ITER is just an experimental reactor with the fusion power of 0.5-0.7GW. The power is much lower than the fusion reactor (3-4GW) in the future [17]. Also the lower neutron wall load in ITER has much lower fusion power and neutron wall load. This allows the application of traditional steels, such as SS316 as structural materials. In the future, the neutron wall load would be high up to 3 MW/m^2,[17] and hence advanced structural materials should be used.

1.1.4 Blanket system

The blanket is located between the plasma and vacuum vessel and provides the main thermal and nuclear shielding to the vessel and other components. The blanket also works as tritium producer and thermal generator in the fusion reactor. To realize these goals, many different concepts were proposed. All of the DEMO concepts could be classified with regard to the breeding materials into two categories [18-23]: solid

ceramic and liquid breeders with the options of self-cooled or separately cooled versions. These concepts also depend on development of structure materials and the design parameters, such as thermal exchange ratio, neutron flux and Tritium Breeding Ratio (TBR). The main functions of blanket are:

(1) The recycle of tritium

As mentioned before, the D-T reaction is the most effective fusion reaction. There is abundant deuterium on earth. The concentration of deuterium in sea water is around 160ppm. However the natural tritium does not exist. The economical way of tritium production is to generate tritium during the operation of fusion reactor bases on the following equations:[24]

$$^6\text{Li} + \text{n} \longrightarrow\ ^4\text{He} + \text{T} + 4.78\text{MeV} \qquad\qquad 1.1\text{-}2$$
$$^7\text{Li} + \text{n} \longrightarrow\ ^4\text{He} + \text{T} + \text{n} - 2.47\text{MeV} \qquad\qquad 1.1\text{-}3$$
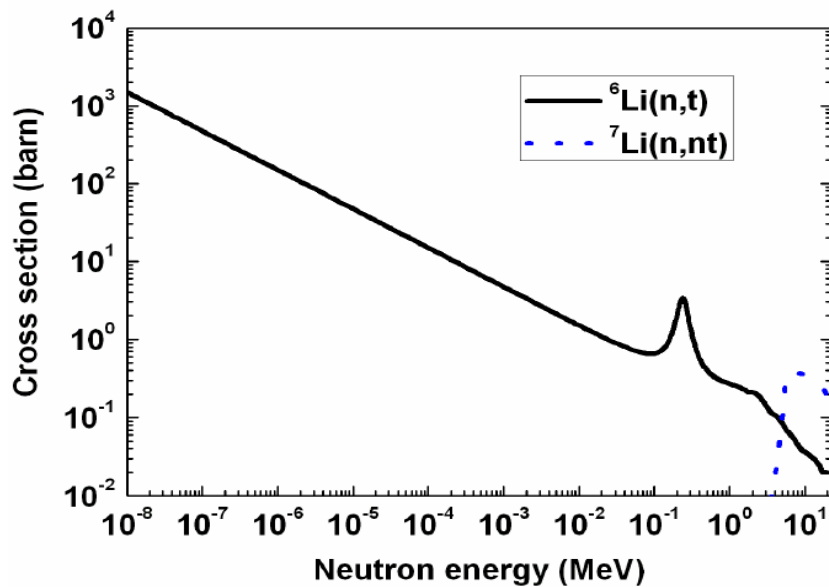
Figure 1.1-4 the cross section of ^{6}Li and ^{7}Li [25]

The percentage of Li isotopic, ^{6}Li and ^{7}Li is 7.42% and 92.58% on earth separately. But it is clear that ^{7}Li is only active during high neutron energy and the

reaction of 1.1-2 dominates tritium production in most case, according to the Fig. 1.1-4. On the other hand, the space for blanket is so small in fusion reactor, that the neutron absorbed by Li is limited. So the neutron multiplier is necessary in some blanket designs. Usually the beryllium (Be) or lead (Pb) is involved to achieve the purpose:

$$^9Be + n \longrightarrow 2n + 2^4He - 2.5MeV \qquad\qquad 1.1\text{-}4$$
$$^APb + n \longrightarrow 2n + {}^{A\text{-}1}Pb - 7MeV \qquad\qquad 1.1\text{-}5$$

Another concern related to the recycle of tritium is how to transport and extract tritium generated in the blanket. Nowadays the most promising method is to bring the tritium out using flow of the coolant or by arranging a separate gas flow for purging, then extract the tritium outside the reactor. The inventory of tritium in coolant and the penetration of tritium should be evaluated before this method is selected.

(2) The neutron shield

Another important function of blanket is to slow down the neutrons and protect the vessel and other components, especially the magnet. The irradiation with neutrons heats up the coil of magnet and results in the failure of superconductivity. Long time irradiation also leads to the degradation of superconductivity and reduces the life time of structural and insulating materials in the blanket system.

(3) The generation and transport of heat

The irradiation of neutron heats up the blanket system. To protect the blanket and transform the energy to electricity, the coolant is involved in the blanket. The potential candidates of coolant are helium, water or liquid metal, etc. The choice of coolant depends on the energy exchange efficiency and the concept of blanket design.

1.2 Candidate materials for blanket

1.2.1 Structural materials

It has been recognized that the development of blanket structural components is the key issue to the successful attainment of safety, environmental and economical advantages of fusion power system. It is essential that the materials satisfy requirements on basic physical and chemical properties which allow a reactor design with high power density, high power conversion efficiency, high availability and attractive safety and environmental attributes. [26]

1.2.1.1 The requirement for structure materials

The structural materials of first wall and blanket in D-T tokamak reactor suffer from:

· High surface heat flux causes mechanical and electromagnetic loading and alternating thermal stresses.

· High energy (14.1 MeV) fusion neutrons produce displaced atoms and helium, hydrogen, and solid transmutation products, leading to changes in bulk properties.

The blanket systems are large systems with combined thermal, hydraulic and mechanical loading, irradiation, corrosion etc. The requirements for fusion structural materials are [27]:

1) The material could withstand high neutron wall loads under temperatures and coolant pressure conditions necessary to drive efficient thermodynamic cycles in a blanket;

2) The lifetime of structural material must be long enough to minimize the necessary replacements of near-plasma components;

3) The material should be of low activation in order to achieve the ultimate environmental attractiveness of fusion power.

Among them, the "low activation" is highlighted because of the rising concern on the environment. Different from fission reactors, no high level radioactive nuclides will be produced from fusion reactors. The concerns of activation mainly focus on the induced radioactivity of the structural materials. By careful selection of the alloy elements, the amount of long half-life radioactivity of the structural materials can be reduced to the point that the materials can be recycled after 50 or 100 yr decay period. The comparison of recycle ability among different candidate materials is shown in Fig.1.2-1.[28] In fact, reduction of the impact on environment is another attractive advantage of fussion comparing to fission reactor.
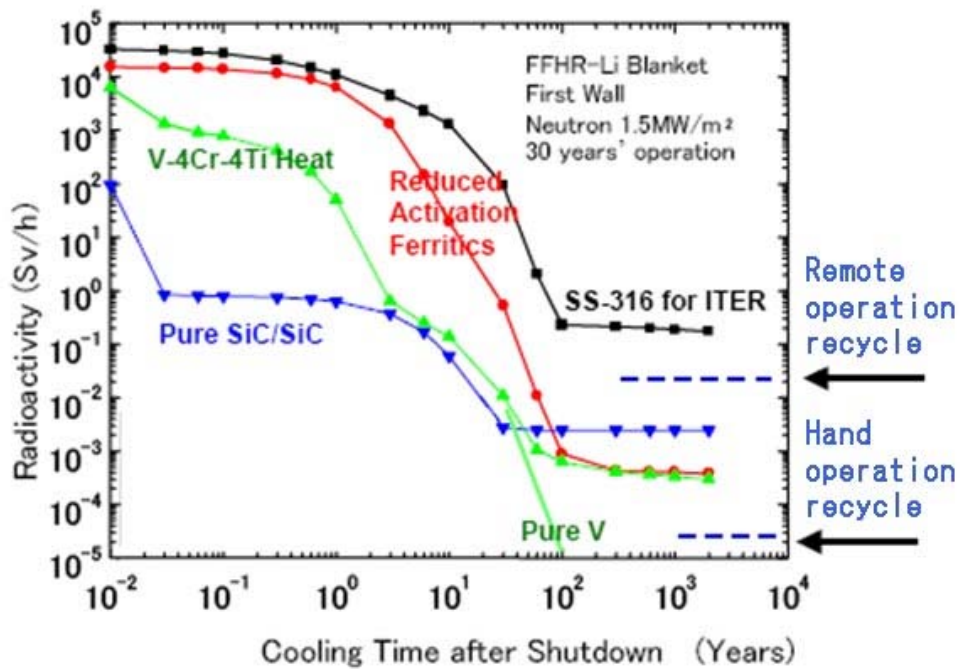

Figure. 1.2-1 Comparison of recycle potential of different materials

1.2.1.2 Candidate structural materials for blanket

(1) Reduced activation Ferritic Steels (RAFM) [26]

RAFM steels have the most advanced technological base relative to other candidate materials. They are a modified composition of conventional Fe-(8-12)Cr-(1-2)Mo steels by exchanging Mo, Ni and Nb with W, V and Ta for the

purpose of obtaining low activation characteristics. Since the Fe-Cr-Mo steels were widely used in many fields, the experience of manufacture, heat treatment and welding can be used for the development of RAFM. Furthermore, Fe-Cr-Mo steels were candidates for cladding materials in LMFBR, and extensive irradiation database is available. The optimum composition of Cr was reported to be 8-9%, based on a series of irradiation tests [29,30]. The advantage of RAFM steels is the high resistance to irradiation, while the disadvantage is the limit of application temperature. The strength of RAFM steels decreases when the temperature is over 600ºC. This limits the operation temperature of blanket. The RAMF steels were developed world wide, such as EUROFER97 in Europe, F82H and JLF-1 in Japan, etc. The compositions of the RAFM are presented in table 1-1.

Table 1-1 Chemical composition of RAFM steels [61]

wt.%	C	Si	Mn	Cr	W	V	Ta	Mo	Ni	Nb
F82H	0.09	0.13	0.16	7.7	1.95	0.16	0.04	–	0.04	–
JLF-1	0.09	-	-	8.92	2.0	0.2	-	-	–	–
EUROFER 97	0.1	0.05	0.44	8.8	1.15	0.2	0.07	0.003	–	0.002
Optifer Ia	0.11	0.06	0.57	8.5	1.16	0.23	0.07	0.005	0.005	0.009
ClAM	0.11	0.01	0.40	8.98	1.55	0.21	0.15	-	-	-

(2) Vanadium Alloys

Vanadium alloys have been identified as one of the leading candidate materials for fusion applications to fusion first-wall-blanket. Certain vanadium alloys exhibit favorable safety and environmental characteristics, such as good fabricability, high temperature and heat load capability, good compatibility with liquid metals and resistance to irradiation damage effects. On the other hand, the vanadium alloy is sensitive to the impurities, such as oxygen, nitrogen, carbon and hydrogen. The existence of these impurities in vanadium alloys leads to degradation of mechanical properties and resistance to irradiation. Especially, the corrosion of vanadium alloys

with lithium would be enhanced by the impurities. Comparing with RAFM steels, the R&D on the vanadium alloy is still limited and progress in the data base of vanadium alloys is necessary.

Efforts have been made recently in National Institute for Fusion Science to produce new V-4Cr-4Ti heats (NIFS-HEATs) with improved purity [33]. The efforts on vanadium alloy development have been focused on characterizing V-4Cr-4Ti, which is regarded as a reference material, to establish performance limit and operation window, and exploring new alloys by changing composition or applying new fabrication processes. The efforts of characterizing V-4Cr-4Ti include improvement of the alloy properties by optimization of thermal and mechanical treatments, evaluation of low temperature and high temperature mechanical properties with and without irradiation, and interaction with environmental impurities.

(3) SiC/SiC Composites

SiC/SiC composites have been developed for aerospace applications and fossil power generation plants because of their high temperature strength, strength to weight ratio and high corrosion resistance. The application of SiC/SiC composites as materials for blanket structural component can significantly increase the upper operation temperature with the advantage of high thermodynamic efficiency. However, some issues are remaining, such as fabrication of massive components, hermetic joining, radiation induced swelling and creep, and radiation induced degradation of thermal conductivity [34]

1.2.2 The candidates for breeder

The breeder materials are classified into two types, the solid ceramics and liquid breeder. They have own advantages and disadvantages. Usually the ceramics containing Li is called solid breeder, such as Li_2TiO_3, Li_2O, Li_2ZrO_3 and Li_2SiO_4. They have less corrosion problem with structure materials, but the irradiation damage and the extraction of tritium are still the concern. A coolant such as gas or pressurized water is

necessary to be introduced in addition to the tritium extraction lines from system.

The liquid breeder includes liquid Li, Li-Pb and LiF-BeF$_2$. They exhibit several features that make them attractive candidates for both near-term and long-term fusion applications. The properties of these liquid metals are list in Table 1-2

Table 1-2 The properties of liquid metal breeder [24]

Candidate	Li	Li-Pb	Flibe(2LiF-BeF$_2$)
Density (g/cm^3)	0.48	9.0	2.0
Heat conductivity ratio (W/m/K)	42	14	1
Melting point (K)	453	508	732
Thermal capability (J/g/K)	0.50	0.17	2.3
Resistance(Ω cm)	2.9×10^{-5}	1.3×10^{-4}	0.65
Reaction with water	Strong reaction	Reaction	No reaction
Tritium recycle	Difficult	Easy	Difficult (TF) Easy(HT)
Tritium inventory	High	Low	Easy(HT) Difficult(TF)
MHD concern	High (self-cooled)	Normal	low

1.2.3 The proposal for blanket system

The breeding blankets need to satisfy some requirements such as tritium breeding ratio, heat removal efficiency, neutron shielding capability and safety characteristics. A number of options are explored for materials and structure of the blanket to satisfy the demands.

The ITER blanket is operated at a low temperature (423-523 K) and lower integrated wall loading (0.3-1 MW/m^2). Type 316LN austenitic steel was selected as the main structural materials for the ITER vacuum vessel and components (shielding blanket, divertor cassettle body) mainly because of the engineering maturity. However, for DEMO and future reactors, the irradiation dose and operation temperature are much higher than that for ITER. 316SS austenite steels cannot be applied to design high

power density blanket because of its low thermal conductivity. Furthermore, the safety and environmental demands require the use of low activation materials for the structural components of DEMO.

Several fusion reactor blanket concepts for DEMO are being developed and are proposed as ITER test module (Table 1-3). All of them can be classified with regard to the breeding materials into two categories: solid ceramic and liquid metal breeders with the options of self-cooled or separately cooled versions

Table 1-3 Proposed ITER test module

TBM	Country	Structure materials	Breeder	Multiplier	coolant
HCSB	China,EU, Japan, Korea RF,US	F82H or Eurofer	Li4SiO4 or Li2TiO3	Be or Be12Ti pebbles	He
WCSB	Japan	F82H	Li2TiO3 or others	Be or Be12Ti pebbles	H2O
DFLL	China	CLAM	Pb–17Li	-	He
HCLL	EU	Eurofer	Pb–17Li	-	He
DCLL	US	F82H	Pb–17Li	-	He
HCML	**Korea**	**Eurofer**	**Li**	**-**	**He**
SCLi	RF	V–4Cr–4Ti	Li	Be	-

1.3 The concept of Li/RAFM blanket and the compatibility issue

1.3.1 Li/RAFM blanket

Liquid lithium is regarded as an attractive breeding material because of its high tritium-breeding rate, high thermal conductivity and so on. Vanadium alloys have mainly been proposed as structural materials for lithium blanket.[36] However, use of Fe-Cr-W based reduced activation ferritic-martensitic steels (RAFM) was proposed

recently as an alternative concept for lithium blanket.[37]

The RAFM is more industrial matured materials relative to vanadium alloys, because of the long application history of Fe-Cr-Mo steels. The experience of manufacture, heat treatment and welding on Fe-Cr-Mo can be transplanted on the development of RAFM. Furthermore, the irradiation database of Fe-Cr-Mo is available, during the research on the cladding materials of LMFBR.[29, 30] But the maximum operation temperature of RAFM is limited because of their strength at high temperature.

Li has several advantages comparing to other breeder candidates.[38] Li is more competitive than solid breeder because:

(1) Immunity of liquids to radiation damage;

(2) Potential for tritium self-sufficiency without a beryllium neutron multiplier. Beryllium is an expensive material and the resources are limited.

(3) Tritium extraction can be performed outside the blanket. Since a liquid can be circulated, it is not necessary to remove the tritium with additional circulation flow for purging tritium.

(4) Low-pressure operation.

(5) Attractive heat transfer and heat removal; without burnout limit like water coolant

Comparing to other liquid metal breeders (Li-Pb and Flibe), Li has:

(1) High TBR(tritium breeding ratio), multiplier is not necessary

(2) Good thermal conductivity and low viscosity

On the other hand, the concerns on the Li/RAFM blanket concept are remaining such as MHD problem, the safety issue due to high reactivity of Li with water and the compatibility with structural materials. Nowadays, some advantages are being made on developing insulatator coating to solve the MHD problem. The safety issue was investigated in the development of fast neutron fission reactor in which the coolant is liquid sodium. The compatibility issue is the theme of this paper.

1.3.2 The compatibility issue for blanket

The application of a liquid breeder and structure material for blanket requires assessment of their compatibility. The two major compatibility concerns arising from the use of liquid metals are:

(1) Corrosion and mass transfer;

(2) Degradation of mechanical properties of the containment material.

Corrosion results in (a) significant wall thinning/wastage and (b) deposition of corrosion products that may cause flow restrictions and excessive accumulation of radioactive material in unshielded regions. The former consequence results in a loss of mechanical integrity and the latter could increase requirements for pumping power, decrease the energy conversion efficiency, and complicate system maintenance. The severity of the corrosion and mass transfer problem varies for different combinations of containment material and liquid metals and depends on many material and process variables.

Degradation of the mechanical properties of structural materials can be caused by the influence of the environment itself and the effects of microstructural and compositional changes that occur in the material during long-term high-temperature exposure to the liquid metal environment. Liquid metals can influence the surface-active properties of the material through liquid metal embrittlement (LME), oxidation, nitridation, or carburization-decarburization phenomena, all of which can alter the near-surface deformation behavior and thus affect mechanical properties such as fatigue crack propagation, creep ductility, etc.

Actually, since the RAFM is relative new materials, the corrosion data about the RAFM steel in Li is quite limited. The previous compatibility researches mainly focused on the corrosion behavior of Fe based steel, such as austenite steels and convectional ferritic steels.

1.3.3 The methods for testing corrosion performance of materials in Li

The corrosion behavior can be studied from static isothermal liquid-metal in vessels or capsules as well as from circulating systems such as thermal-convection loops (TCLs) and forced circulation loops (FCLs), as shown in Fig. 1.3-1.

Exposure to static lithium systems have been carried out to investigate the characteristics of the various reactions between the environment and the material and to study the exposure condition and material variables on the interactions. Exposure to flowing lithium in a loop test has been carried out to investigate the dissolution and mass transfer behavior of structural materials. TCLs, with low flow speed, were used to study the corrosion behavior and mass transfer under temperature gradient. On the other hand FCLs with pump can makes the velocity of Li flow controllable. The corrosion behavior in FCLs is more similar to self-cooled blanket systems.
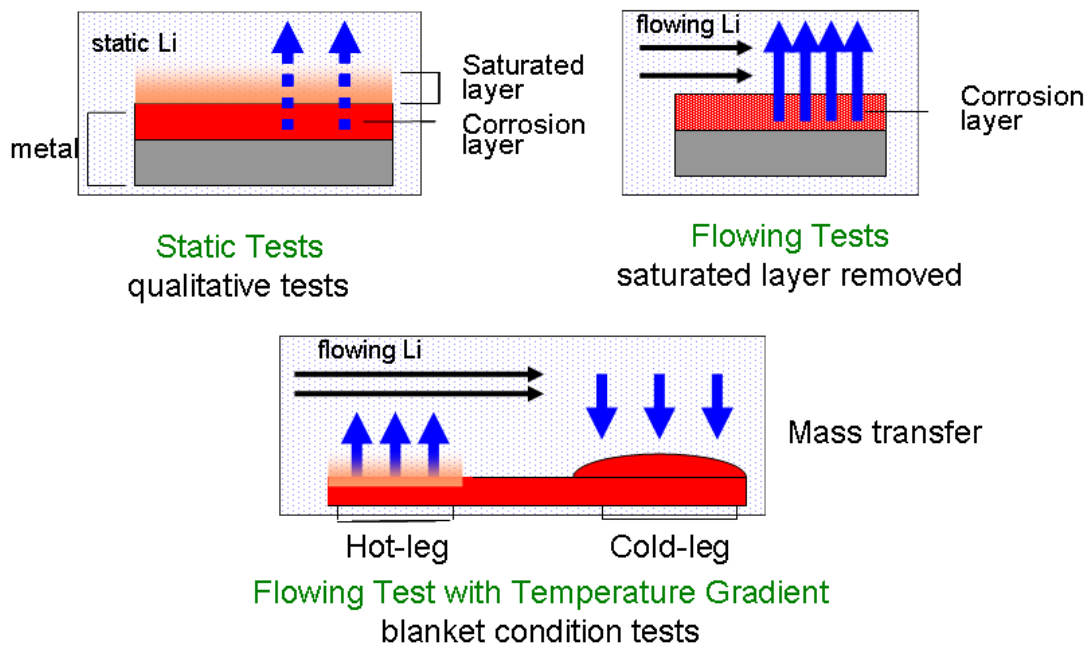
Figure 1.3-1 Methods for corrosion test

1.4 Research status of compatibility of iron based materials in Li

1.4.1 Corrosion

Several studies have been conducted to evaluate the influence of material and system parameters on the corrosion behavior of austenitic and ferritic steels in liquid lithium environment. The principal mechanisms of corrosion of materials in a liquid metal environment are dissolution, intergranular penetration, interstitial-element transfer, and mass transfer due to thermal and concentration gradients.

Table 1-4 the corrosion data of ferritic and austenitic steel in liquid Li

Metal	Materials	Temp. (ºC)	Flow rate	Exposure time (h)	Estimated corrosion depth (μm/year)	Reference
Ferrite steels	Fe-9Cr-Mo	372	1 L/min	6000	0.05	[56]
	Fe-12Cr-1Mo	372	1 L/min	6000	0.09	[56]
	Fe-9Cr-Mo	427	1 L/min	7000	0.15	[41]
	Fe-12Cr-1Mo	427	1 L/min	7000	0.17	[41]
	Fe-9Cr-Mo	538	1 L/min	3500	0.6	[56]
	Fe-12Cr-1Mo	538	1 L/min	3500	0.7	[56]
	Fe-12Cr-1MoVW	600	0.025m/s	7000	3.3	[40]
Austenite steels	Fe-17Cr-13Ni-2Mo-	427	1 L/min	7000	6.3	[41]
	Fe-14Cr-16Ni-2Mo	427	1 L/min	7000	9.5	[41]

The corrosion rate of ferritic and austenitic steels in Li was presented in Table 1-4. According to previous results, the corrosion rate of the ferritic steels in lithium is more than one order of magnitude lower than that of austenitic steels. The corrosion behavior of ferritic steel, Fe-12Cr-1MoVW, was investigated by P.F.Tortorelli in a convection loop made by the same materials. [39, 40] The N concentration was controlled to 30~100Wppm by a cold trap. The dissolution kinetic of ferrite steels in Li obeyed linear

law, as shown in Fig. 1.4-1. O.K.Chopra's experiment agreed that the weight loss of ferrite followed a linear increase with the exposure time.[41]
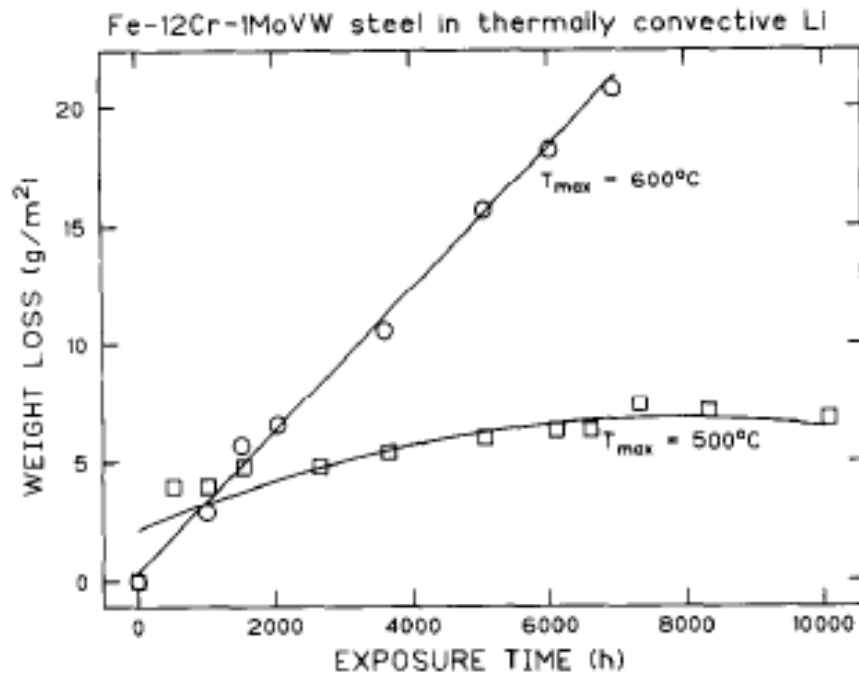

Figure 1.4-1 The weight loss versus exposure time for Fe-12Cr-1MoVW in Li[40]

The dissolution rates for austentic stainless steels reached steady-state (time-independent) values after an initial period of 1500 to 3000h [42-44] This type of dependence was described in Fig. 1.4-2. The initial stage (stage A) of high dissolution rates corresponds to the formation of a ferrite layer which results from preferential dissolution of nickel from the surface of the austenitic steels. The steady-state regime (stage B) is characteristic of the dissolution of an austenitic stainless steel having a ferritic surface layer that is depleted of nickel.
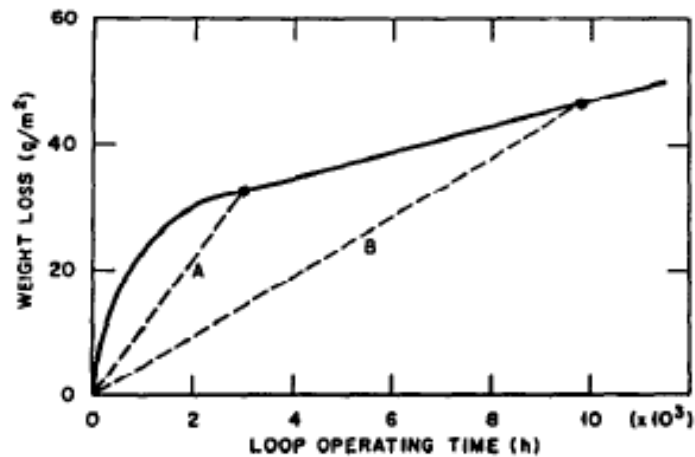
Figure 1.4-2 corrosion of austenite steel in Li [39]

It was also reported that the 9Cr-steel (Fe-9Cr-Mo) showed better resistance than the HT-9(Fe-12Cr-Mo) by O.K.Chopra.[41] The average dissolution rates for both HT-9 and Fe-9Cr-1Mo steels are 6.3 and 0.15μm/yr at 427ºC, respectively, when N concentration was lower than 100wppm. In another experiment [45], these values of dissolution rates obtained in a cold-trapped forced-circulation lithium loop are consistent with the rate of 0.5μm/yr observed for HT-9 alloy in a lithium thermal convection loop at 460ºC. The N concentration in lithium in the latter test was reported to be < 100 wppm.

1.4.2 The effect of impurities in Li

The impurities, such as N, O, H, in Li affect the corrosion behavior of steels in liquid Li. The solubility of transition metals is enhanced by the presence of dissolved non-metals. Among them, the strong impact of N was highlighted. Experimental results showed that austenitic and ferritic steels were very sensitive to the N concentration in both flowing and static condition.[41,46-48] Chopra pointed out that when the N content increases from 100ppm to 300ppm, the dissolution rate increase by factors of 1.5 to 3 in a lithium FCL system operating at 360 to 482ºC[41]   A nitrogen-alloyed Cr-Mn steel exposed to static lithium at 873 K formed a Li-Cr-N compound at the grain

boundaries.[49] A ternary nitride, Li_9CrN_5, was found on the surface of Type 316 SS that was exposed at 475°C to nitrogen-saturated lithium.[50,51] These could lead to possible selective dissolution of Cr when the structure materials are exposed in Li containing high level of N.

The C transfer between the steel and Li has a strong impact on the mechanical properties of structural materials. The carburization or decarburization phenomena are caused by the difference in chemical potential of C in Li. The chemical reaction between N and C in Li could enhance the C dissolution from the steels. The chemical reaction of N in Li was investigated by R.J. Pulham[51]:

$4 Li_3N + Li_2C_2 = 2 Li_2NCN + 10 Li$

$2 Li_3N + Fe = Li_3FeN_2 + 3 Li$

$5 Li_3N + Cr = Li_9CrN_5 + 6 Li$
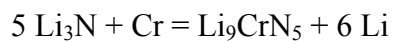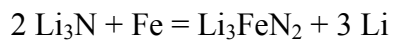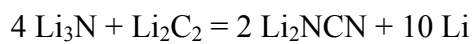
1.4.3 The influence of steel composition on corrosion in Li

Because of different solubility of alloy elements in Li, the composition of steel influences the weight loss and corrosion rate of materials in Li. Without the effect of impurities, the solubility of elements in Li dominates the corrosion behavior of steels. The solubility values of the major steel elements are shown in Fig 1.4-3 [52-53].
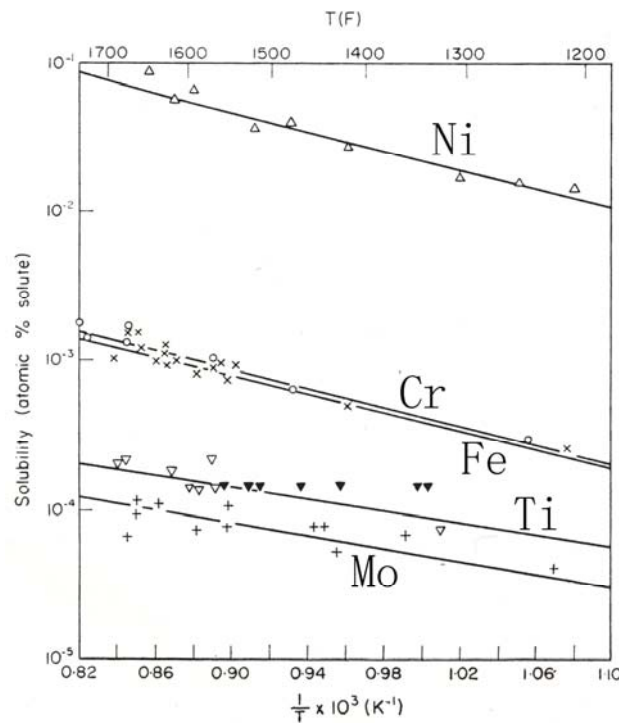
Figure 1.4-3 the solubility of main alloy element in Li

The N concentration: 50~100ppm [52]

As shown in the figure, the solubility of element in liquid metal increases with the temperature. So the increase of temperature generally enhances the corrosion. The different solubility of various alloys elements is the main reason for the selective dissolution during the exposure in liquid metal. The high solubility of Ni indicates that the corrosion rates increase with an increase in the nickel content of the material.[54,55]

The selective dissolution of alloy element causes not only weight loss, but also microstructure change and degradation of mechanical properties. The microstructure of 316SS after exposure to lithium at 600ºC for 8000h was presented in Fig. 1.4-4.[39] A porous ferrite layer was observed on the surface of specimens. It was reported that loss of Ni was the main reason caused the phase change from austenite to ferrite. The ferrite layer was very weak because of the high porosity, and it can easily spall under high liquid velocities, thermal transients, or cyclic straining. The formation of a porous ferrite layer has a significant effect on the mechanical behavior of the structural components made by austenitic stainless steels.
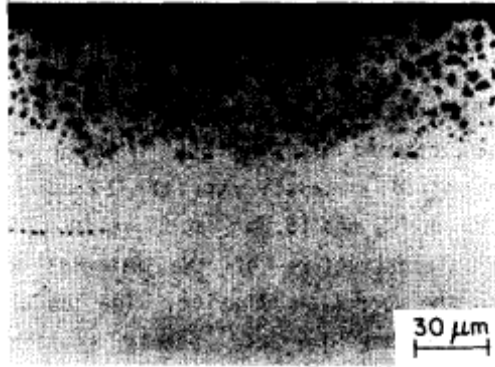
Figure 1.4-4 316 stainless steel exposed for 8000h in flowing Li at 600ºC

1.4.4 Compatibility of RAFM with Pb-Li

Studies were carried out on compatibility of RAFM steels with flowing Pb-Li. The past data are summarized in Table 1-5.[57–61] At 480ºC, the evaluated corrosion rate of RAFM steels is less than 100μm/yr in Pb-Li, although the test periods changed from 4500h-12000h. It indicates that the weight loss of RAFM increases linearly with the exposure time. It should be noticed the corrosion rate significantly increases with increasing the test temperature: 700μm/yr at 550ºC. [58] As for the flow rate effect, high flow rates resulted in a high corrosion rate, indicating that the flow rate needs to be suppressed to reduce the corrosion rate.

Table 1-5 corrosion data of RAFM steels in Pb-Li

Materials	Temp. (ºC)	Flow rate	Exposure time (h)	Estimated corrosion depth (μ m/year)	Reference
EUROFER 97	480	0.3 m/s	12000	90	[57]
EUROFER 97	550	0.3 m/s	1000	700	[58]
Optifer, MANET1, F82H-mod.	480	0.3 m/s	6000	100	[59]
EUROFER 97	480	0.01 m/s	4500	40	[60]

It was reported that it took time for Pb-Li alloy to wet whole surface of specimen during exposure. The wetting issue could result in an apparent low corrosion rate at the first stage of experiment because the corrosion might only occur in the section where the steels contacted with Pb-Li. The period of wetting depends on the temperature [57] and surface condition of specimen, such as original oxide layer [62]. Fig.1.4-5(a) and (b) shows the metallographic observations of EUROFER 97 after typical corrosive Pb-Li attack for different exposure time. As shown in 1.4-5(a), the surface of sample was all covered with the Pb-Li alloy, indicating that the specimen was completely wetting with Pb-Li alloy after exposure for 1500h. In Figs.1.4-5(b), the SEM micrographs obtained on the cross-section of the 3000h tested samples are reported. As presented in the figures, a layer about 1 μm thick seems to detach from the surface of the steel. At the interface between the layer and the bulk material, voids could be observed, and the EDX analysis indicated that the layer was Cr depleted. The experiment in other system also proves that the dissolution of Cr and Fe from RAFM in Pb-Li is the major mechanism.
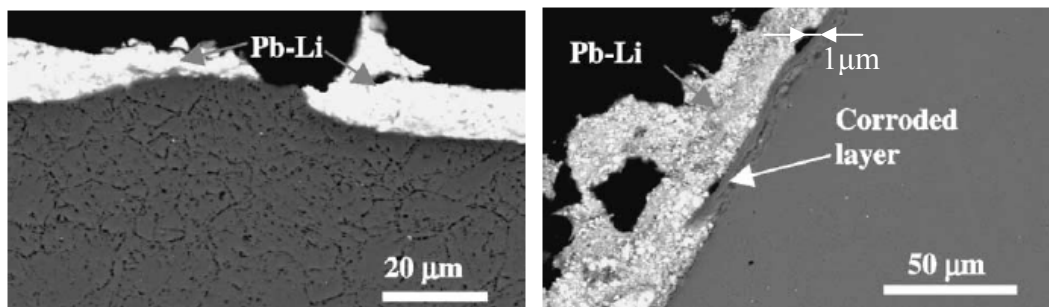
1.4-5 Cross section of Eurofer97 after exposure in Pb-Li [60]

The corrosion of different RAFM in Pb- Li was compared by Konny.[58] A summary of the maximal corrosion attack result from MANET I, Optifer IVa, F82H-mod. and EUROFER 97 was given in Fig.1.4-6. The lines for each alloy type were inserted by optical fitting to illustrate the time dependency. According to figure, the corrosion line of Eurofer97 is 10-20% lower than other RAFM steels. This cannot be explained by the chemical dissolution of alloy elements, because these alloys have very similar alloy composition. Probably the minor alloy elements, such as Ti and N, or low impurity level in steel are responsible for the difference. It is also influenced by

initial oxide layer on the surface of specimens. It was reported that the initial oxide layer delayed the onset of corrosion.[62]
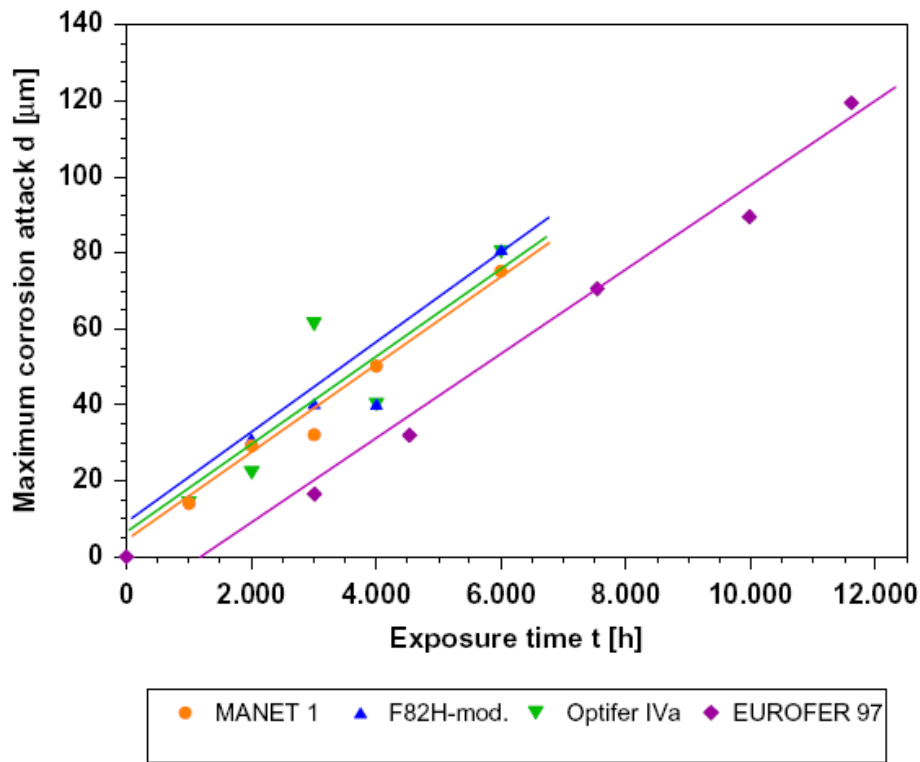

Figure 1.4-5 comparison of RAFM steels in Pb-Li

1.5 The object of this work

1) The purpose of the present study is to examine the compatibility of RAFM steels with liquid Li in static and flowing conditions with respect to :

   - Corrosion rate

   - Mass transfer and compositional change

   - Microstructure

   - Mechanical properties

2) Based on the experimental results, mechanism of the compatibility will be explored, including model analysis

3) Feasibility, critical issues and emphasis in the development of RAFM-Li blanket will be discussed

Chapter 2

Experiment

The compatibility issue of structure materials RAFM steel with liquid Li was studied in several aspects,

1) Comparison of different materials to investigate the influence of alloy elements

2) Static experiments to explore the kinetic weight loss of RAFM steel in Li

3) The corrosion behavior of RAFM steel in flowing Li

4) The compositional effect of the container materials on corrosion behavior of RAFM steel in Li

2.1 The composition and pretreatment of specimen

In this study, Fe-Cr-W based RAFM steel, JLF-1, was selected as the test material. The composition of JLF-1 is listed in table 2-1. For comparison, pure Fe and Fe-9Cr were also used in this experiment. Their compositions are presented.

Table 2-1 the composition of materials (EDS analysis, wt %)

	Fe	Cr	W
JLF-1	balance	8.9	2.0
9Cr	balance	9.11	0.11
Pure iron	99.99	-	-

JLF-1 specimens were heat-treated at 1050ºC /3.6ks/air cooled (normalizing) and 780ºC /3.6 ks/air cooled (tempering). Pure Fe and Fe-9Cr were rolled, annealed at 700 ºC. All materials were prepared as coupon specimens. The size of coupon specimens was 26×5×0.25mm, as shown in Fig. 2-1. The surfaces of the specimens were mechanically polished with No.180, No.40 and No.600 sand paper before the experiment.
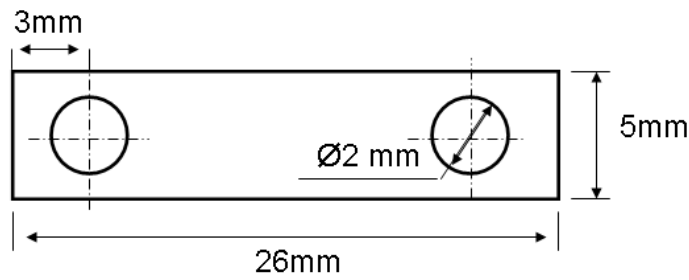
Figure 2-1 the size of coupon specimens

2.2 The procedure of the experiments

2.2.1 The application of Li

The high purity Li was ordered from market. The composition provided by company is showed in table 2-2. It is well known that the Li is very sensitive to air and water. Li can strongly react with water in room temperature and absorb O_2 and N_2 to form compounds. Especially, the N has a strong impact on the corrosion behavior of steel in Li.[48-50] To suppress the effect of impurities, the preparing work of experiment was carried out in glove box filled with argon whose nitrogen level was less than 1ppm., as shown in Fig. 2-2.

Table 2-2 Chemical composition of Li (wppm)

	Na	Ca	Fe	K	Si	N
Li	40	40	10	10	50	40

After the experiment, flowing water was used to remove the Li adhere to the specimens and the experiment systems. As the result of strong reaction between H_2O and Li, heat and irritant gas was released during the cleaning. The cleaning with water not only removes Li, but also dissolves probable corrosion products formed on the specimens. It was reported that the corrosion products, such as Li_9CrN_5 and $LiFeN_2$, may play an important role during the Li exposure.[49] The corrosion product layer can

isolate the metal substrate from liquid Li and prevent the development of corrosion. To investigate the effect of the corrosion products, some specimen was cleaned by dry ammonia to reserve the corrosion products. The Li dissolves in ammonia and form a dark blue solution and the corrosion products remained on the surface of specimen.

Figure 2-2 The glove box

2.2.2　Expsoure to static Li

After Li was melted, the coupon specimens were doped into the Li in a container. Holders or wires were used to fix the specimen to prevent them from attaching with each other. In most cases, the static exposure experiments to liquid Li were carried out in a Mo container which was placed in a stainless steel autoclave. Fig.2-3 shows the Mo container, holder and autoclave. For each experiment, 10 specimens were exposed in 100ml Li, and the ratio of Li volume V_{Li} (cm^3) to total surface area of specimens S (cm^2) was around 4 (cm).

Glove box and experiment system   The pot and Mo container

Container (Mo)

Specimen holder (Mo)

10 JLF-1 Specimens for each experiment

3cm
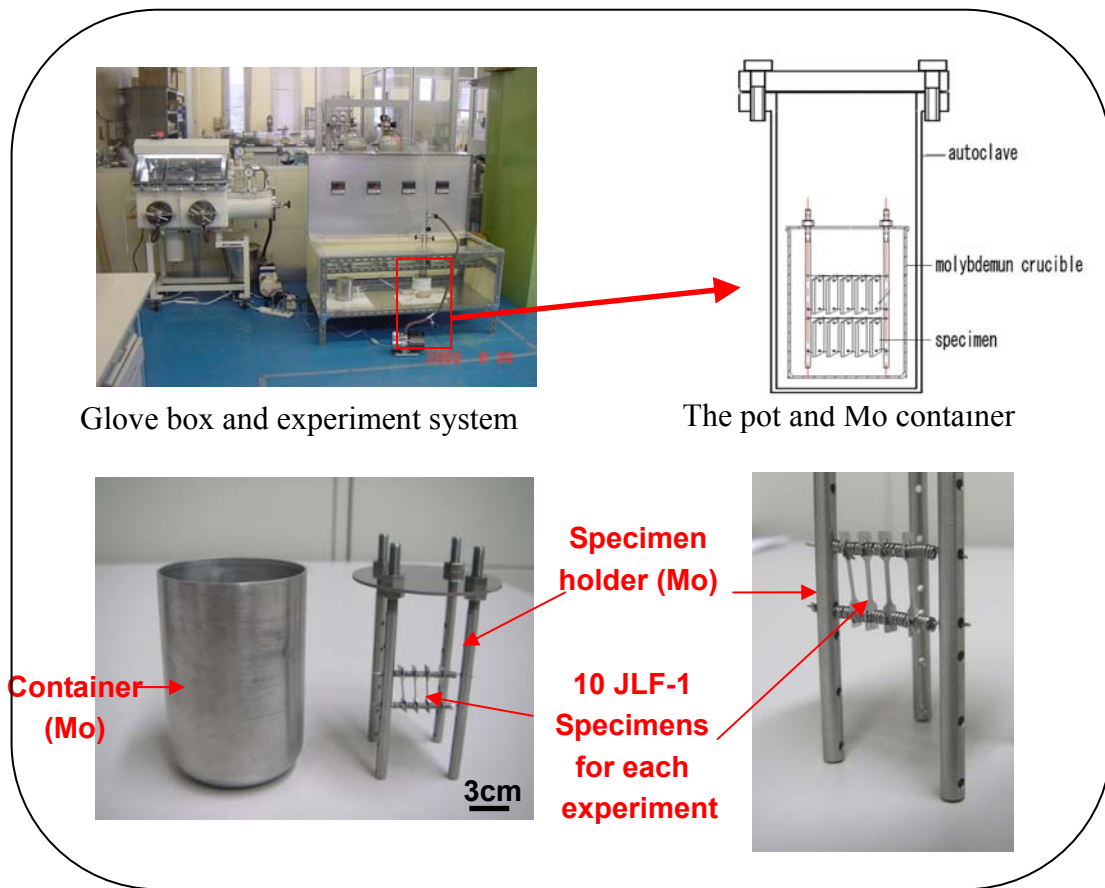
Figure 2-3 the Mo container, holder and autoclave

2.2.3 Exposure to flowing Li

The corrosion behavior in flowing condition is different from that in static condition. The corrosion process, such as erosion and mass transfer in flowing Li, are closer to the reality in reactor. In this work, Flowing tests were carried out in a thermal convection Li loop facility, which was made of SS 316L stainless steel and was composed of the loop, a Li tank and a heating system. The detail of the loop was reported in a reference.[24] A schematic diagram of the facility is shown in Fig. 2-4.
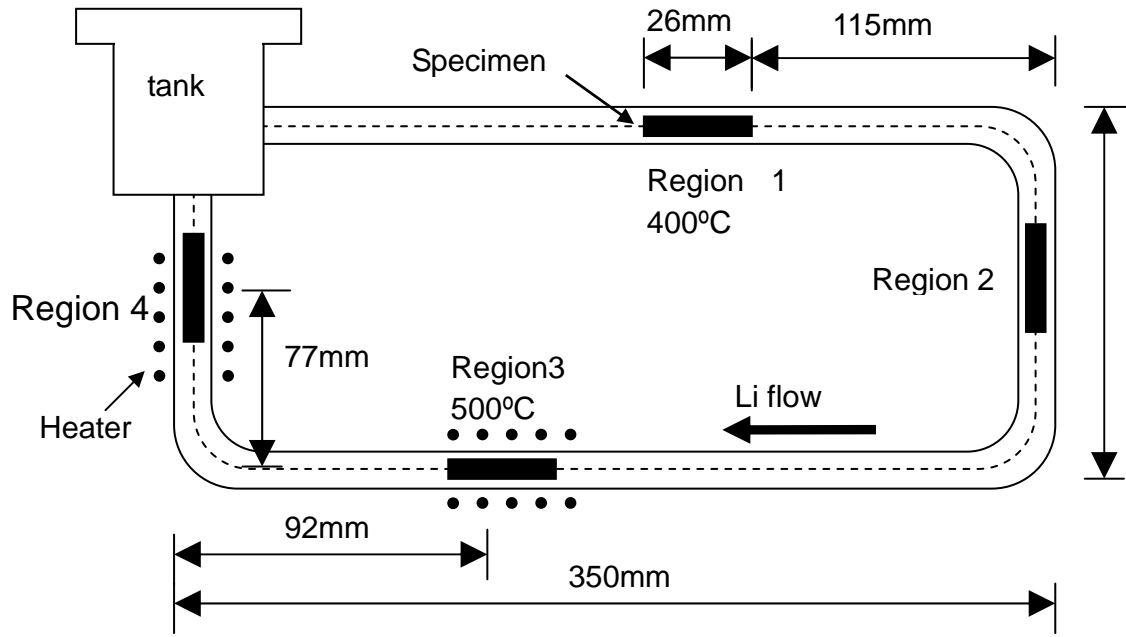
Figure. 2-4 The thermal convection loop

The inventory of Li in the loop was 200ml and the estimated flowing velocity was 0.05 m/s. The loop was divided into four regions by the temperature difference: hot-leg region 3; cold-leg region 1; transition temperature parts, region 2 and region 4. Specimens were fixed by Mo wires at each position. The impurity concentration in the loop test was expected to be comparable with the static experiment because of the similar preparing procedure. The size and surface condition of the specimens were common to those for the static exposure. After Li exposure for 250h, liquid Li drained away from the loop to the drain tank. The loop was disassembled and Li remained on surface of the specimens and the loop interior was cleaned by water.

The velocity of loop was given by following equation[24]:

$$v = \frac{-\mu_{\mathrm{m}} + \sqrt{\mu_{\mathrm{m}}^2 - 2gh(\rho(T_2) - \rho(T_1))\sum \zeta\rho}}{\sum \zeta\rho}$$

μ_m　　— the loss of friction

g　　— the gravity

h　　— the height of vertical part

ρ(T₁) — the density of Li in high temperature

ρ(T₂) — the density of LI in low temperature

ζ　　— the loss of shape of loop

:

2.2.4 The methods of analysis

Many analytical methods were applied to characterizations of corrosion. The change of weight before and after exposure was measured by the electro-balance with accuracy to 0.01mg. The microstructure and composition were analyzed by transmission electron microscopy (TEM), electron diffraction (ED) and scanning electron microscopy (SEM) with energy dispersive X-ray spectroscopy (EDS). The change of hardness was detected by Vickers hardness meter with a load of 10gf. The contents of C and N in JLF-1 alloys at various conditions were analyzed by chemical method. The surface of specimen was analyzed by X-ray diffraction (XRD) to identify the structure of corrosion product.

Chapter 3

Comparison of corrosion behavior of JLF-1,
pure Fe and Fe-9Cr in liquid Li

In this study, the compatibility of RAFM with lithium was investigated including comparative examinations using binary Fe-Cr alloy and pure iron.

3.1 The experimental condition

JLF-1(Fe-9Cr-2W-0.1C), a pure iron and a Fe-9Cr binary alloy were used for the experiment. The facility for static experiment and the pretreatment of specimen and were introduced in chapter 2.

The experimental conditions were listed in table 3-1. Pure iron, Fe-9Cr and JLF-1 were exposed to lithium at 700ºC for 100h (test A) to study the influence of alloy elements. Another group of JLF-1 specimens were exposed in lithium for 100h at 600 ºC and 700 ºC (test B) to study the influence of temperature.

Table 3-1 The experimental condition

Materials	Group A			Group B	
	JLF-1	Fe-9Cr	Pure Fe	JLF-1	
Temperature	700 ºC	700 ºC	700 ºC	600 ºC	700 ºC
Exposure time	100h	100h	100h	100h	100h
Clean method	NH_3	NH_3	NH_3	NH_3, H_2O	NH_3, H_2O

The specimens in group A were cleaned by ammonia after the exposure in static Li followed by surface analysis. In group B, the specimens were cleaned by ammonia and water in turn and the weight change was measured after each step. In addition, JLF-1 as received was annealed in vacuum for 100h at 600 and 700ºC to examine the effects of thermal history.

3.2 The results and discussion

3.2.1 Weight loss and selective dissolution

The weight changes during the tests at 600ºC and 700ºC for 100h are shown in Table 3-2. After exposure for 100h, pure iron and Fe-9Cr gained weight, while JLF-1 lost weight. This indicates that faster corrosion took place at JLF-1 during lithium exposure. Small corrosion occurred on JLF-1 specimen at 600ºC. The corrosion rate after water cleaning is 0.0046mm/a. (Note that constant dissolution rate is assumed for the estimate). In the present experiment, water cleaned specimen had higher weight loss than ammonia cleaned ones, due to removal of the surface corrosion products by water.

Table 3-2 Weight loss and the surface composition of specimens exposed to Li for

Materials/exposure temp.	Ammonia cleaning	Water cleaning	Surface composition (EDS result)			
	Weight loss (g/m^2h)*	Weight loss (g/m^2h)*	Fe	Cr	W	C
JLF-1/bef.experiment	−	−	89.0	8.9	2.0	0.1
Fe/ 700ºC	-0.021	Not available	96.4	1.7**	−	−
Fe-9Cr/ 700ºC	-0.0075	Not available	92.1	6.3	−	−
JLF-1/ 700ºC(A)	0.0075	Not available	93.5	5.4	1.	−
JLF-1/ 700ºC(B)	0.0327	0.1667	90.7	7.5	0.8	−
JLF-1/ 600ºC(B)	-0.065	0.0041	92.1	6.8	0.7	−

* Constant weight change rate during the immersion was assumed

** This seems to be the result of Cr deposition from Li during the cooling period

(A) JLF-1, pure iron and 9Cr were exposed in the same lithium pot

(B) Only JLF-1 was exposed in lithium pot

The surface composition change derived by EDS measurement from the normal direction to surface is listed in Table 3-2. As shown in Table 3-2, depletion of chromium

and tungsten was observed on the surfaces of all specimens exposed in liquid lithium except pure iron. Increase in Cr on the surface of the pure iron seems to be caused by the deposition from lithium during the cooling period. The depth of Cr depletion was about 5μm according to EDS line scan as shown in Fig. 3-1. The selective dissolution of both Cr and W is thought to enhance the weight loss of JLF-1 relative to that of Fe-9Cr and pure iron.
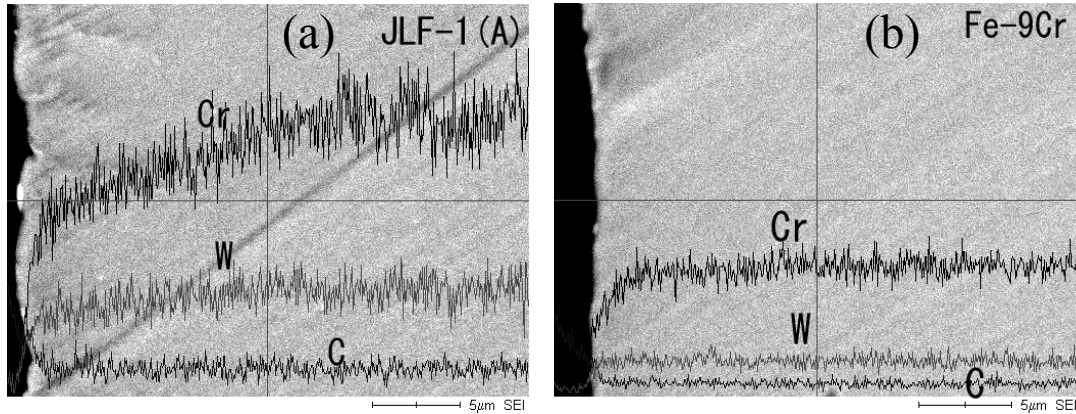

Figure. 3-1 Cross section EDS line scan on JLF-1 (Test A) and Fe-9Cr after exposure to Li at 700°C for 100h

3.2.2. Phase transformation and hardness reduction

The surface morphology of JLF-1 (ammonia clean) exposed at 700 ºC is shown in Fig. 3-2. Clear grain structure was observed on the surface of the specimen exposed in Li for 100h at 700ºC. Spongy corrosion product layer covered the surface of the specimen after cleaning with ammonia. XRD was carried out to find out the composition of the corrosion products, as shown in Fig. 3-3. XRD result showed that the surface corrosion products were mainly composed of Li_2CO_3. Triple compound Fe-Mo(W)-C was also detected on the surface of specimens These corrosion products disappeared during cleaning with water. It is clear that phase transformation occurred at the surface of JLF-1 with martensite structure changing into a ferritic phase. This phenomenon was not found on the specimen that was annealed in vacuum at the same temperature for 100h, as shown in Fig. 3-2. No phase transformation was observed on JLF-1 after exposure at 600ºC.
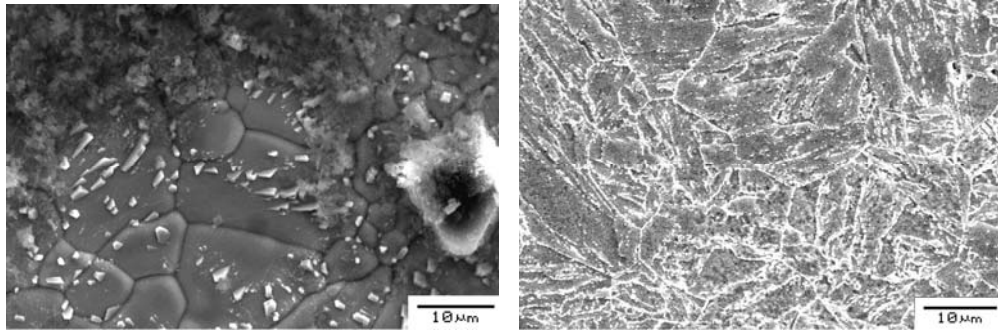
a. JLF-1 exposed in Li at 700ºC for 100h   b.   JLF-1 annealed in vacuum at 700ºC for 100h
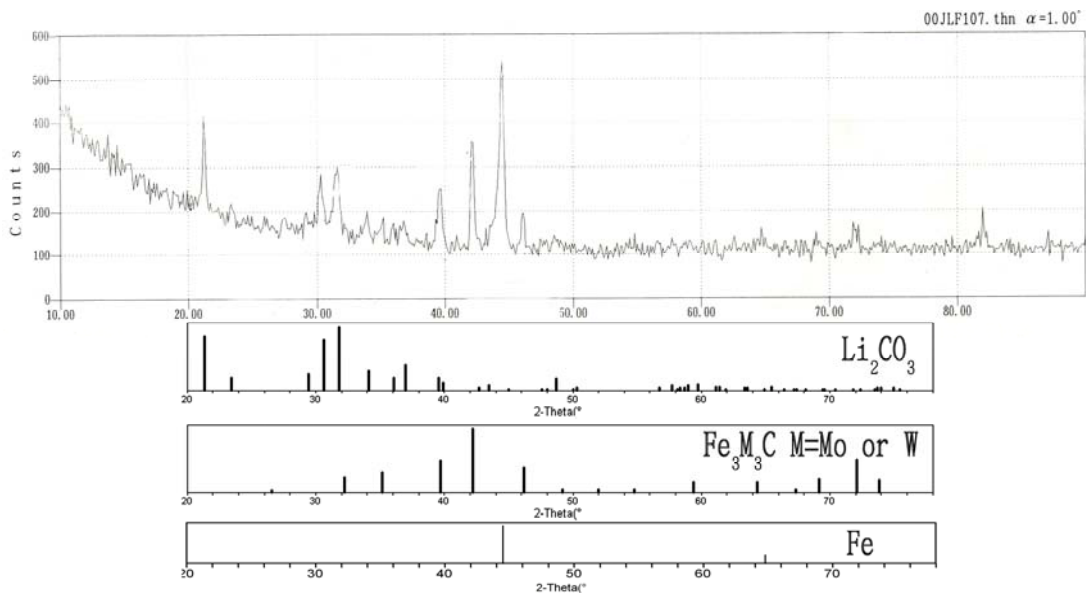
Fig.3-2. SEM micrographs of JLF-1

Figure 3-3 XRD result of corrosion products on the surface of specimen exposed at

700ºC for 100h

The phase transformation has also been observed inside the specimen. Fig. 3-4 (a) and (b) are the cross section SEM pictures of JLF-1 exposed at 700ºC in test A and test B respectively. The phase change from martensite to ferrite was observed in both A and B situation. Especially in test B, the phase transformation depth reached 100μm after exposure in Li at 700 ºC for 100h. The martensite structure only remained in the center of specimens as seen in Fig. 3-4 (b). The phase change from martensite to ferrite was supported by TEM results. Fig.3-5 (a), (b) and (c) showed the TEM picture of JLF-1 before exposure, after annealing in vacuum at 700ºC for 100h and after exposure in Li

at 700ºC for 100h (Test A) respectively. It is clear that the microstructure change occurred on JLF-1 specimen exposed in Li 700ºC for 100h. The fine lath structure converted to ferritic structure in the TEM picture. Furthermore, the carbide almost disappeared in the area of phase change area. On the other hand, the annealing in vacuum led almost no change on the microstructure of JLF-1. This indicated that the phase change from martensite to ferrite was not caused by heat treatment, but by the Li attack.

a. Test A   b. Test B
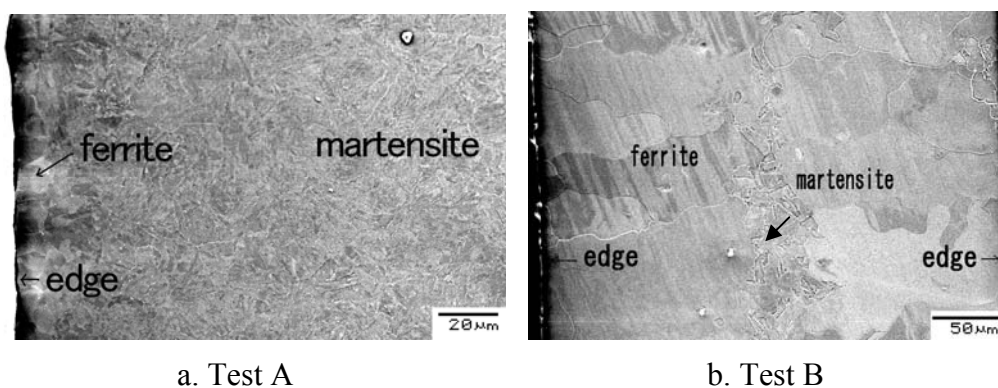
Fig.3-4. Cross section SEM and TEM images of JLF-1 exposed Li at 700ºC for 100h for the two tests.
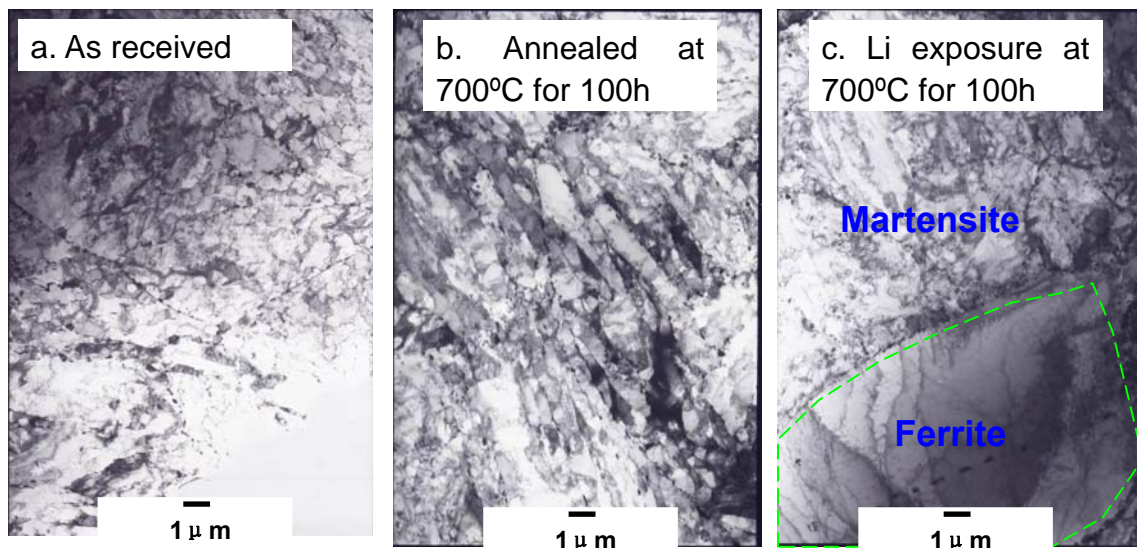
Figure 3-5 TEM picture of JLF-1 (a) as received (b) annealed at Annealed at 700ºC for 100h (c) after exposure in Li at 700ºC for 100h

3.2.3 Degradation of mechanical properties

Figure 3-6 shows hardness change with depth before and after exposure to lithium. The hardness reduction occurred on JLF-1 and Fe-9Cr at 700ºC. For Fe-9Cr, the softening seems to be caused by Cr depletion because the softening depth is close to Cr depletion range of 5μm. In JLF-1, phase transformation played a dominant role for the hardness. The depth of softening is consistent with the phase transformation depth. By the carbon dissolution and phase change, the hardness decreased from 250 to 140Hv. In the case of test B (700ºC), the hardness of JLF-1 at the area where the phase change occurred was close to that of Fe-9Cr.
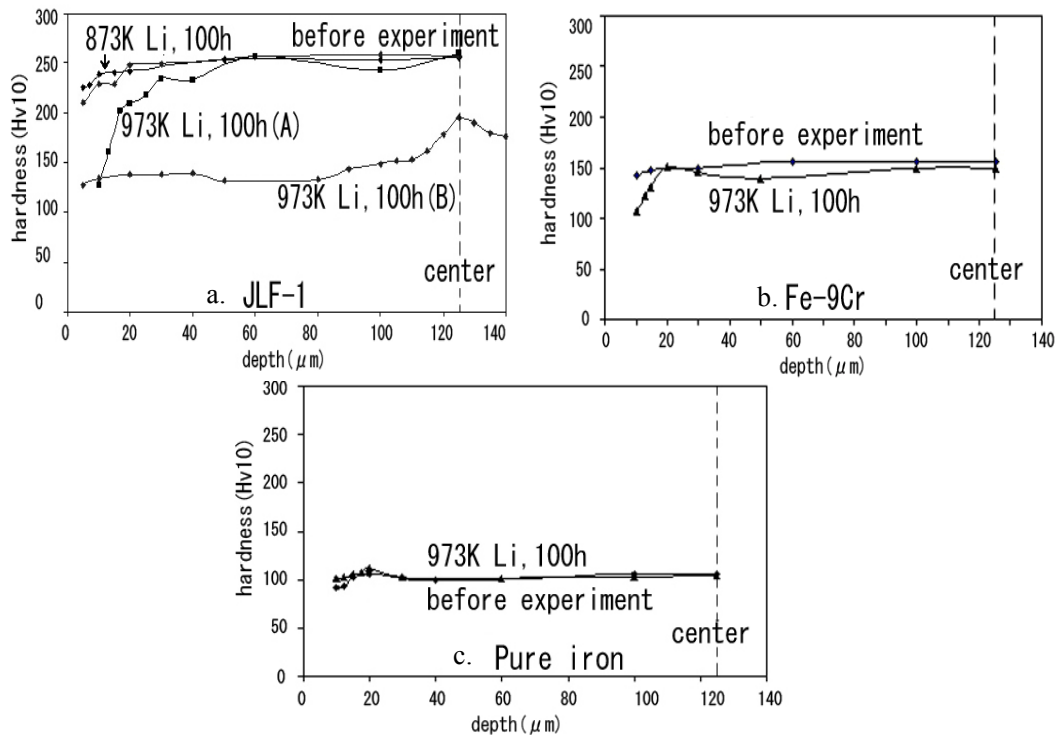
Fig.3-6. Depth dependence of hardness

This implies that W has small impact on hardness in single ferritic phase. The fact that the hardness at the center of the specimen in test B is between that of the martensitic and ferritic phase implies that the phase at the center is mixture of the two phases. For pure iron, hardness was kept constant because neither phase transformation nor selective

dissolution of alloying element occurred. Almost no hardness change was detected on JLF-1 exposed at 600ºC.

The chemical analysis of JLF-1 was carried out and the result is listed in Table 3-3. Two third of carbon in JLF-1 (test B) dissolved into liquid Li at 700ºC for 100h. Martensite can be converted to ferrite when carbon is removed. Thus, the loss of carbon is expected to be the major reason for the phase change in this experiment.

According to thermodynamics graph in Fig. 3-7,[8] the order of stability of these compounds is at $700^{o}C$ is $V_2C > VN > Li_3N > L_2C_2 > Fe_3C$. It indicates the tendency that V should get C and N, while Fe should lose C during lithium exposure.

Table 3-3. Chemical analysis result (wt %, JLF-1 specimens in test B)

Materials	C	Cr	W
Before exposure	0.09	8.92	2.00
Li 700ºC 100hr	0.03	8.88	1.95
Li 600° C 100hr	0.10	8.89	1.99
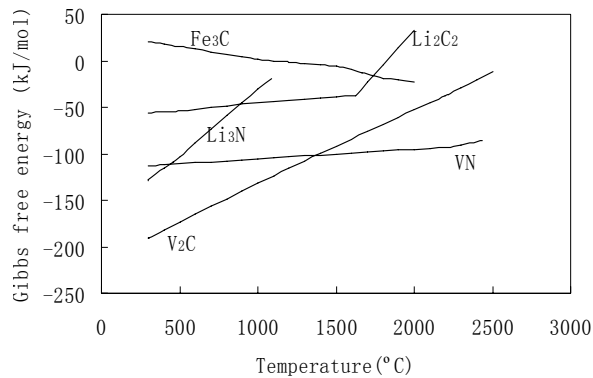
Fig.3-7   Thermodynamic data of several compounds in Li[8]

3.3 Summary

At 600ºC, relatively small corrosion occurred on JLF-1 exposed to lithium. Neither phase change, nor carbon depletion was found. On the other hand, JLF-1 was largely influenced by the exposure at 700ºC, including depletion of carbon and chromium and resulting phase transformation from martensite to ferrite. Hardness reduction was caused by the phase transformation and element dissolution

The corrosion of JLF-1 is more significant than that of Fe-9Cr and pure iron at 700ºC. The selective dissolution of Cr, W and C into lithium seems to enhance the corrosion.

Chapter 4

The compatibility of JLF-1 in static and flowing Li

The corrosion behavior of the RAFM steel, JLF-1, in a static Li was investigated preliminarily in chapter 3. The corrosion of the JLF-1 was summarized as selective dissolution of C, Cr and W, and phase transformation from martensite to ferrite because of C depletion. The depth of the phase transformation was estimated to be 100μm for JLF-1 exposed in Li for 100h at 700ºC, while no phase change occurred at 600ºC for 100h. The structure change was considered not to be the result of thermal history effects but the chemical effects, because no phase change was observed on the specimen after a vacuum anneal with the same temperature history. However, the corrosion and the depth of the phase change in the static experiment can be underestimated because saturation could be formed around the specimen, which might suppress further corrosion in the static test condition.

The purpose of the present study is to investigate further the corrosion characteristics and phase transformation phenomena of JLF-1 in blanket relevant conditions. Various static experiments were carried out at 500 ºC and 600 ºC for longer exposure time and a corrosion test for JLF-1 in flowing Li in a thermal convection loop was performed at 500 ºC.

4.1. Experimental condition

The detail of the static test facility was introduced in chapter 2. The surfaces of JLF-1 specimens were mechanically polished before the experiment. Static exposure experiments to liquid Li were carried out in a Mo container with Mo specimen holders, which were placed in a stainless steel autoclave. The experimental conditions are summarized in Table 4-1.

Table 4-1. Experiment condition

Static exposure				Flowing exposure
600 ºC		500 ºC		500 ºC
250h	750h	250h	750h	250h

The specimens were exposed at 500ºC and 600ºC for 250h and 750h. Considering the serious phase transformation observed only after 100h exposure at 700ºC in chapter 3, exposure time of 250h~750h was considered to be sufficient for comparative study. The Li was refreshed in every exposure test. After the experiment, the Li remained on the specimens and the holder was dissolved in water. In this case, most of corrosion products on the specimens were removed during the cleaning. The results at 600ºC and 700ºC, which were presented in the previous studies, are also presented for comparison.

Flowing tests were carried out in a thermal convection Li loop facility, which was made of SS 316L stainless steel and consisted of the loop, a Li tank and a heating system. The detail of a loop was reported in a reference.[24] A schematic diagram of the facility is shown in Fig. 4-1. The inventory of Li in the loop was 200ml and the estimated flowing velocity was 0.05 m/s.
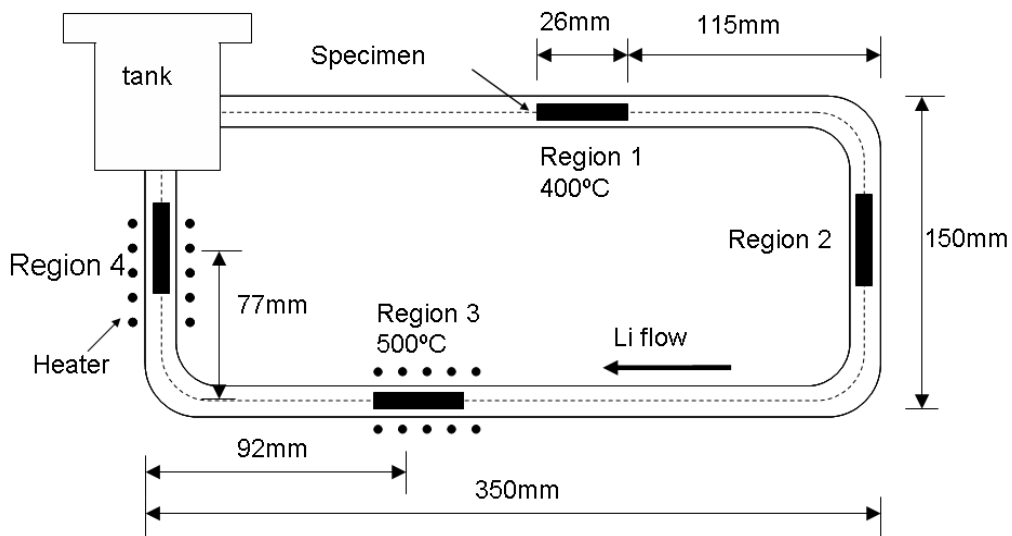
Figure 4-1. Illustration of the Li convection loop

During the corrosion tests, the operating temperatures for the loop system were divided as: hot-leg region 3 (500ºC); cold-leg region 1 (400 ºC); transition temperature parts, region 2 and region 4. Specimens were fixed by Mo wires in each position. The impurity concentration in the loop test was expected to be comparable with the static

experiment because of the similar preparing procedure. The size and surface condition of the specimens were common to those for the static exposure. After Li exposure for 250h, liquid Li drained away from the loop to the drain tank. The loop was disassembled and Li remained on surface of the specimens and the loop interior was cleaned by water.

The examinations of the specimens were carried out for weight loss measurements by electro-balance with the accuracy of 0.1mg, surface morphology and composition by SEM/EDS, microstructure by TEM, hardness by Vickers Hardness Testing Machine with the weight of 10g.

4.2 The corrosion characteristics in static and flowing condition

4.2.1 The weight loss kinetic of JLF-1 in Li

The corrosion rate was evaluated by measuring the change in the specimen weights before and after the exposure in static and flowing Li. The weight loss in static and flowing Li at 500 ºC and 600 ºC is shown in Fig. 4-2. Each symbol type in the figure represents weight loss for a specimen after various exposure conditions. The data of static tests at 600ºC and 700 ºC for 100h which were shown in the previous chapter were also presented. According to the figure, the weight loss became almost constant after exposure for ~250h at 500 ºC and 600 ºC in static test as average of the data. The specimens suffered from a serious corrosion at 700ºC. In flowing Li, the weight loss of JLF-1(hot-leg specimen) was one order of magnitude larger than that in static exposure.
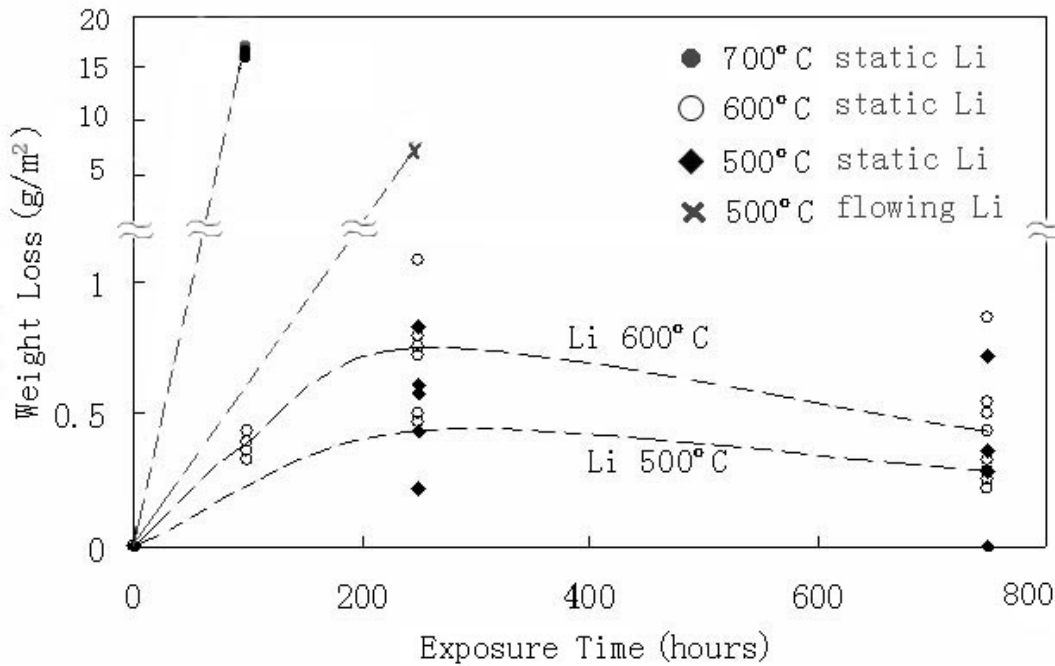
Figure 4-2. Weight loss versus exposure time

Table 4-2. Weight loss and EDS results after exposure to Li

	weight change (g/m²h)	Phase transformation	Surface EDS analysis			
			Cr	Fe	W	Ni
Before exposure	-	-	8.9	89.0	2.0	-
region 1(cold –leg 400 ℃)	0.038	No	1.7	32.3	0.7	65.3
region 2	0.014	No	2.6	40.3	0.9	55.4
region 3 (hot-leg 500 ℃)	-0.033	~10μm	4.0	59.8	1.2	3.3
region 4	0.001	No	2.3	39.5	0.8	56.5

The detail of the weight loss and the surface composition for the specimens exposed in the loop are presented in Table. 4-2. From the table, only the specimen located in hot-leg (region 3) lost weight, while other specimens placed in lower temperature area gained weight after the flowing Li exposure. The specimen located in cold-leg (region 1) gained weight most. The enrichment of Ni was detected by EDS on the surface of the specimens located in low temperature area, but almost no Ni was detected on the specimen exposed at hot-leg (region 3), as presented in Table. 4-2. It is thought that the nickel was originated from the tube materials of SS316L.

4.2.2 SEM/EDS observation

The surface configuration of the specimens exposed at 500 ℃ and 600 ℃ is shown in Fig. 4-3. Because of the cleaning with water, there was almost no corrosion products adhered on the surface. The possible corrosion products, such as Li_2O, Li_9CrN_5, etc., would have dissolved into the water. As shown in Fig.4-3 a-d, phase transformation from matensite to ferrite was observed on the surface of almost all specimens exposed in liquid Li, except the specimen exposed at 500 ℃ for 250h, where the martensite lath structure was observed. However, the phase change on the surface was found after exposure to flowing Li for 250h at 500 ℃, as shown in fig. 4-3e.
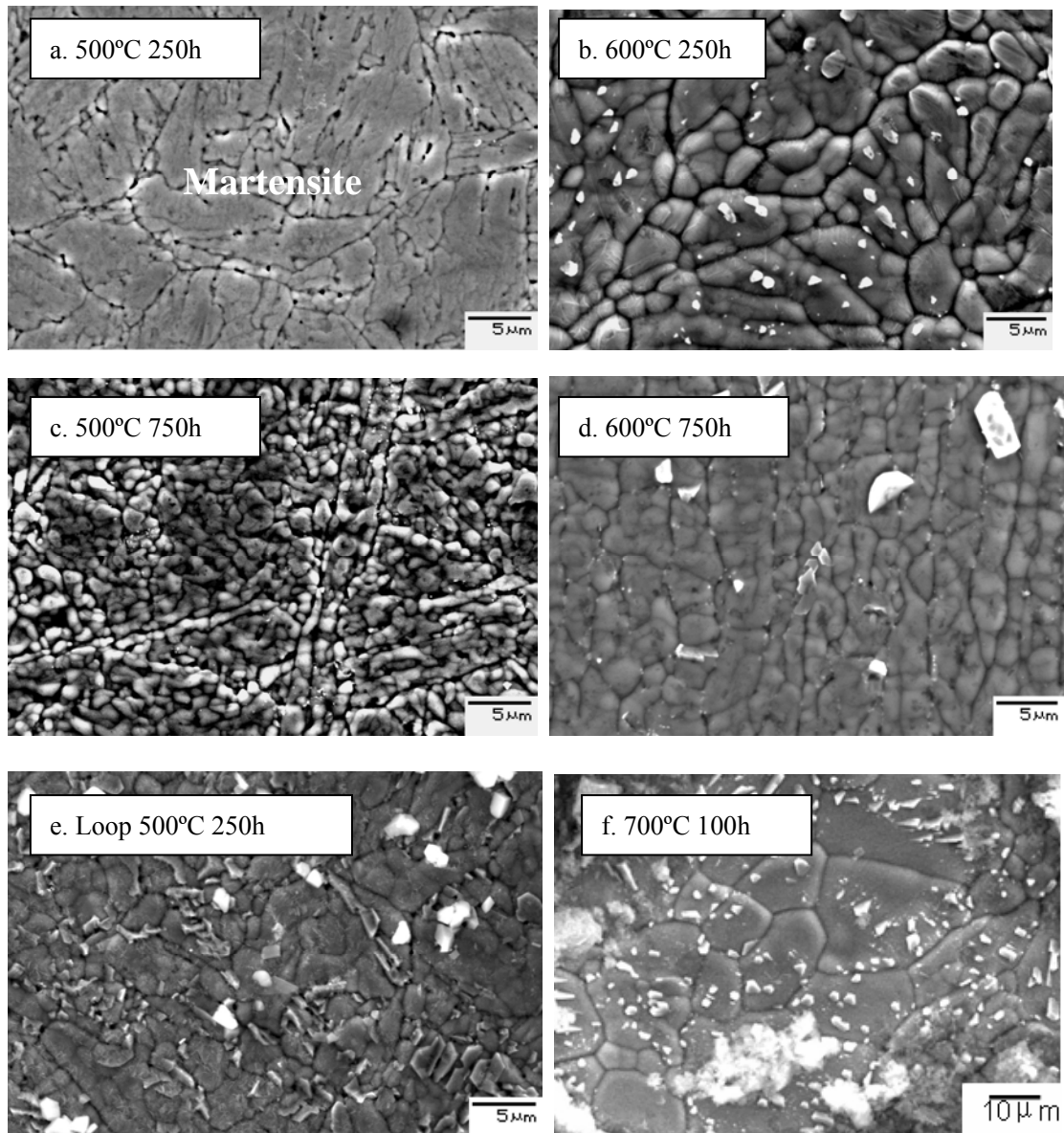
Figure 4-3. Surface of JLF-1 exposed in static Li

After the loss of the martensite structure, grain boundaries can be seen on the surface of the specimens. The grain size of the ferrite phase observed after exposure at 500ºC and 600ºC was much smaller than the original austenitic grain boundary (10μm), but close to martensitic lath size. On the other hand, after 700 ºC exposure for 100h, the surface of the specimens displayed large grains, whose size was close to those of austenitic boundary.

Phase transformation was also observed in depth of JLF-1 specimens. Fig. 4-4 shows the cross sections SEM micrographs of the specimens exposed at 600 ºC for 250h in static Li and at 500 ºC for 250h in flowing Li. The figures show that the depth of the

phase change on JLF-1 specimens is about 10μm in both cases. In the phase transformation zone, the density of carbide precipitates decreased drastically. In Fig. 4-5, local depletion of carbide was clearly observed on the specimens exposed at 600ºC for 750h. The dissolution of carbides into liquid Li resulted in holes near the surface. Neither phase change nor C depletion was observed by cross section SEM in the case of static exposure at 500ºC.
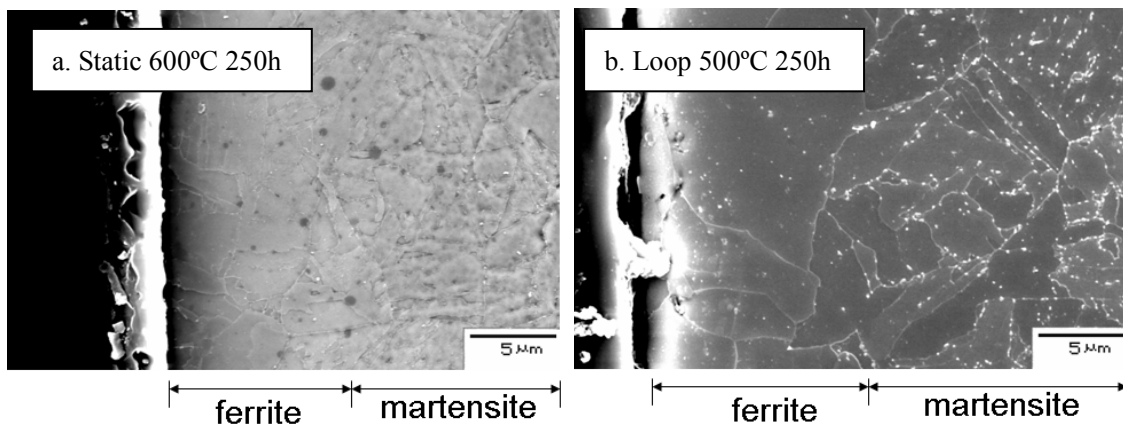
Figure 4-4. Phase change on cross section of JLF-1
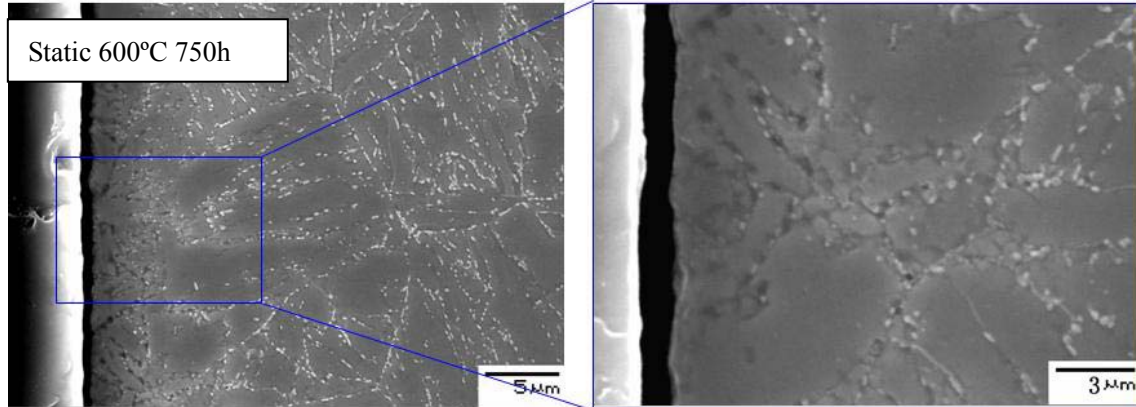
Figure 4-5. Disappearance of carbide precipitates after exposure at 600 ºC for 750h
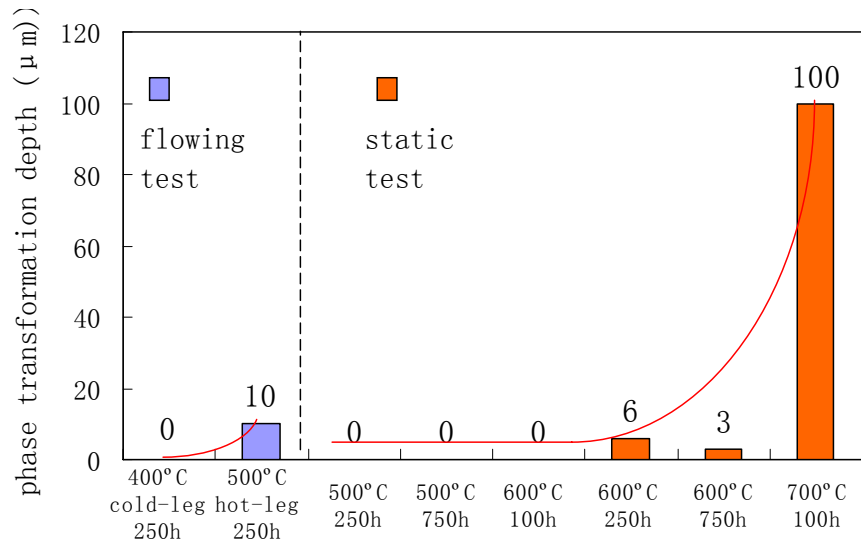
Figure 4-6. The phase transformation depth in different conditions

The phase transformation phenomenon was found under different exposure conditions. The relationship of phase change with temperature and exposure time is shown in fig. 4-6. The figure shows that the phase transformation depends on exposure time, temperature and flowing condition. In the static exposure, the phase transformation appeared when the temperature exceeded 600ºC and the exposure time was relatively long. At 700ºC, deeper phase transformation was observed. In the flowing test, however, phase change in 10μm depth was already found on the specimens after exposure at 500 ºC for 250h.

EDS surface analysis and line scan of the cross section were performed to determine the composition of the corroded region. The results of line scan of the cross section were presented in Fig. 4-7. The figures revealed a slight depletion of Cr and W near the surface after exposure at 500ºC and 600ºC. In the flowing test, on the other hand, the significant selective dissolution of Cr was found in depth (Fig. 4-7e).
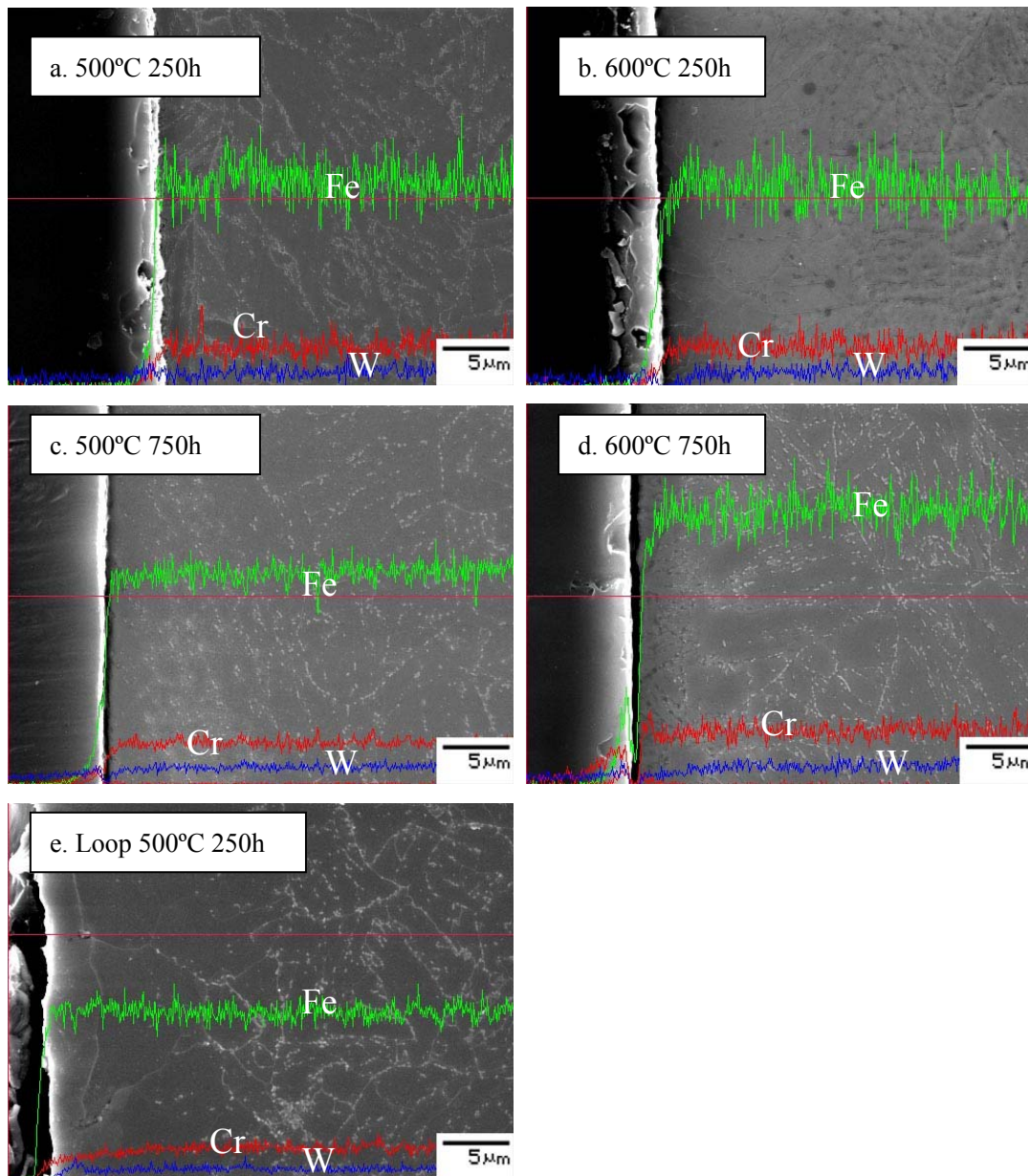
Figure 4-7. EDS line scan on cross section

4.2.3 Hardness measurement

To investigate the influence of Li corrosion on mechanical properties, Vickers hardness test was carried out before and after the Li exposure. The hardness was measured on the cross section of the specimens. Fig. 4-8 shows hardness change as a function of depth after exposure to Li for 250h at different temperature. The hardness before and after exposure at 700ºC for 100h are presented as well. As reported in the previous chapter, the hardness of JLF-1 drastically reduced from 250 to 140Hv when

specimens were exposed at 700 ºC for 100h. The softened range was around 100μm, which was consistent with the phase transformation range. In the case of 600ºC for 250h in static condition and 500ºC for 250h in flowing condition, the area where the hardness largely decreased also corresponded with the area where martensite changed to ferrite.
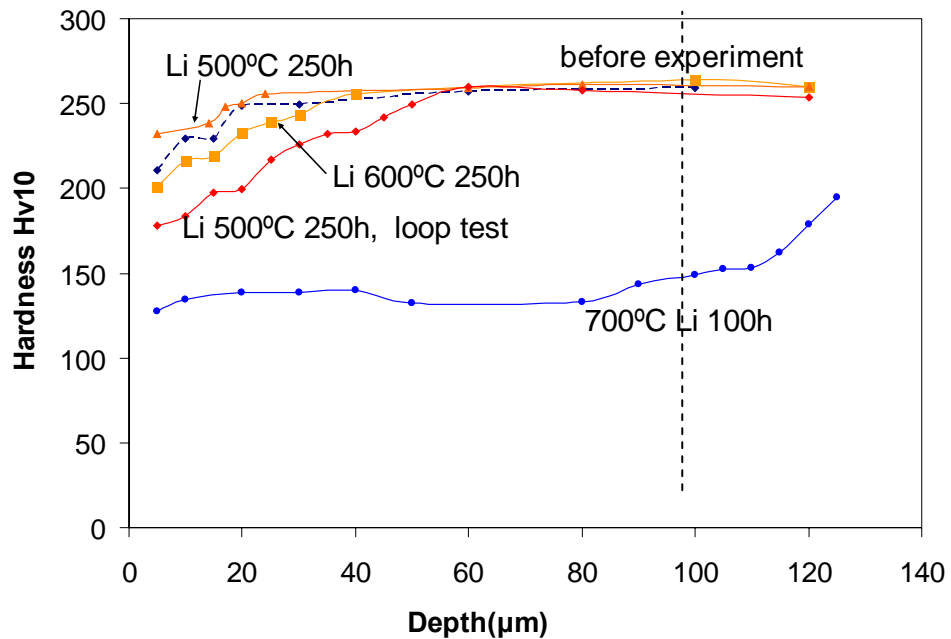
Figure 4-8. Hardness change on cross section of JLF-1 under various exposure conditions

4.3 Discussion

4.3.1 Mass change

In the static exposure, the average weight losses of JLF-1 specimens became constant for 250h exposure at the temperature of 500ºC and 600 ºC as shown in Fig. 4-2. This was probably caused by the saturation of Fe, Cr in bulk Li during the static exposure. However, Fig.2 also showed that the weight loss is very different with specimens in the case of static exposure. This suggests that the situation was different with specimens because of the variation of local flow in static test condition.

According to Table 4-2, the specimens lost weight in hot-leg, but gained weight in cold-leg after the exposure to flowing Li. This is thought to be caused by mass transfer during the loop operation. The elements which dissolved from specimen surfaces and the tube interior in high temperature area deposited on the specimens in lower temperature area following temperature gradient. This is supported by EDS measurement, in which Ni enrichment was detected on the surface of specimens exposed in lower temperature area, but not in the highest temperature area. Because of the mass transfer effect, the elements would not saturate in high temperature area. Thus the specimens in hot-leg continuously lost elements. The continued dissolution of the elements resulted in a significant corrosion compared with the static exposure. From Fig.4-2, 4-6 and 4-8, the specimens exposed in flowing Li (hot-leg) showed more serious weight loss, phase change and softening than the specimens exposed in static Li at the same temperature and exposure time. The results clearly suggest the need for systematic loop experiments with temperature gradient to evaluate the corrosion performance in the blanket condition. On the other hand, the specimen in cold-leg (region 1) gained weight after loop exposure. This was mainly due to the precipitation of Ni originated from the loop materials of SS316L. According to Fig.1.4-3, the solubility of Ni is an order magnification larger than Cr and Fe at Li in high temperature. Thus, during the exposure, significant amount of Ni was expected to have dissolved into Li from SS316L tube. Because of mass transfer effect, a large amount Ni precipitated on

the surface of specimens in cold-leg during the operation.

The major process for the weight loss of JLF-1 steel in the liquid Li seems to be dissolution of Cr, Fe and W in the alloy and the corrosion rate depends on the solution rate of Cr, Fe and W in the liquid Li. C has much high solubility than Cr and W in Li at the same temperature. However, since the concentration and mass of C in JLF-1 are much lower than those of Fe, Cr and W, the contribution of C depletion on the mass loss was small. On the other hand, the depletion of C played an important role in phase transformation and hardness reduction.

4.3.2 Phase transformation

The loss of C seems to be the driving force to phase transformation. Because of chemical interaction between C and Li, the solubility of C in Li is much higher than Fe and Cr, and decarburization of JLF-1 in liquid Li is possible. According to the chemical analysis results, 2/3 of C in JLF-1 dissolved in Li after 100h exposure at 700ºC. This agreed with the SEM result that more than 2/3 volume of JLF-1 specimen transformed from martensite to ferrite. Because of loss of interstitial element, C, the phase transformation from bct to bcc could happen at 600ºC or 700ºC. Additionally the depletion of carbides was observed on the cross section of JLF-1 specimens as shown in Fig. 4-5. After carbide depletion, small hole remained near the edge of cross section. Fig. 4-4 shows that the area where the precipitates disappeared was consistent with that of the phase change.

As shown in Fig. 4-8, liquid Li exposure has a strong effect on the mechanical properties of JLF-1. The softened area is consistent with the phase transformation area. According to the figure, the hardness decrease from center to edge gradually. This implies there was a transitional region where martensite and ferrite phase were mixed. This was verified by TEM observation in chapter 3.

According to the above results, two consequences will be caused by the corrosion of JLF-1 in liquid Li: the general weight loss and reduction of mechanical properties. These need to be taken into consideration when RAFM is used facing Li. The present

results also suggest the need for long time flowing experiments with temperature gradient for evaluating the corrosion performance in the blanket condition.

4.4. Summary

The compatibility of RAFM steel, JLF-1, with static and flowing Li was investigated. The main conclusions are:

(1) In static exposure, the weight loss became constant after 250h exposure, because of the saturated elements in liquid Li.

(2) The phase transformation from martensite to ferrite was caused by C depletion.

(3) The drastical softening of the surface area of JLF-1 by exposure to Li was due to the phase transformation.

(4) The flowing Li accelerated the weight loss, phase change and hardness reduction due to the mass transfer. The results clearly suggest the need for systematic loop experiments with temperature gradient for evaluation the corrosion performance in the blanket condition.

Chapter 5

The effect of composition of the container on
the corrosion behavior

In chapters 3 and 4, the corrosion behavior of the RAFM steel, JLF-1 (Fe-9Cr-2W), in a static and flowing Li was investigated. Two concerns arising from attacking of Li are (a) the weight loss (b) the loss of C destabilized the martensitic structure and led to form a ferritic layer on the surface of JLF-1 specimens. The corrosion in the form of dissolution of alloy elements might cause significant thinning of structure materials after long time application in fusion reactors. The phase transformation from martensite to ferrite resulted in degradation of mechanical properties of the structure materials. However, the mechanism of corrosion of JLF-1 in liquid Li is not clear so far.

In static test, the system consists with specimens, Li and container materials. The migration of alloy elements and impurities should be taken into consideration in the whole system. Furthermore, in the real reactor, the blanket will be made by different materials in various parts to achieve economical opinion. The influence of different materials in corrosion system should be studies. In the current experiment, the SUS316l, Mo and Nb were involved as container to study the corrosion characteristics of JLF-1 steel.

5.1 Experiment in different container

The JLF-1 specimens were prepared as chapter 2. The Fig. 5-1 showed the sketch of this experimental device. Static exposure experiments to liquid Li were carried out in a new Mo, SUS316L and Nb container separately. The size and shape of the three containers were the same. In each experiment, 10 JLF-1 specimens were exposed. The container was sealed in an autoclave filled with argon. The details of the static test facility were introduced in chapter 2.
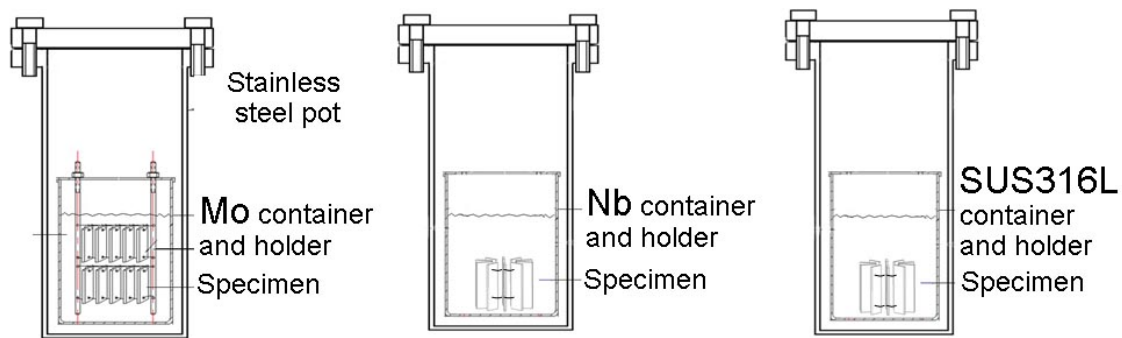
Figure 5-1 Sketch of experiment in Mo, Nb and SUS316L container

The JLF-1 specimens were exposed at 600ºC for 250h in three different containers. After the experiment, the specimens and the holder were cleaned by water. After Li exposure, the weigh loss was measured by electro-balance with the accuracy of 0.1mg. The surface morphology and composition checked by Scanning Electron Microscope (SEM) equipped with Energy Dispersive X-ray Spectrometer (EDS). The degradation of mechanical properties was analyzed by Vickers hardness testing machine with the load of 10g. To investigate the effect of impurities and the dissolution of transition elements in Li, the composition of Li was measured before and after experiment.

5.2. The investigation in effect of container materials

The results of the weight alteration of specimens exposed in all three cases for 250h at 600ºC are presented in Fig. 5-2. For comparison, the weight loss of specimen exposed in reused Mo container under the same temperature and exposure time was also shown in the figure. After exposure, JLF-1 specimens exposed in Mo and Nb container lost weight, while the specimens gained weight in SUS316L container after exposure. The transfer of Ni from the SUS316L container to specimen seemed to be the main reason for the weigh gain occurred during the exposure. The maximum value of weight loss was observed in new Mo container, which was 50% larger than that in reused Mo container. This suggested that the fresh Mo surface might play an important role in the process of corrosion in Mo container.
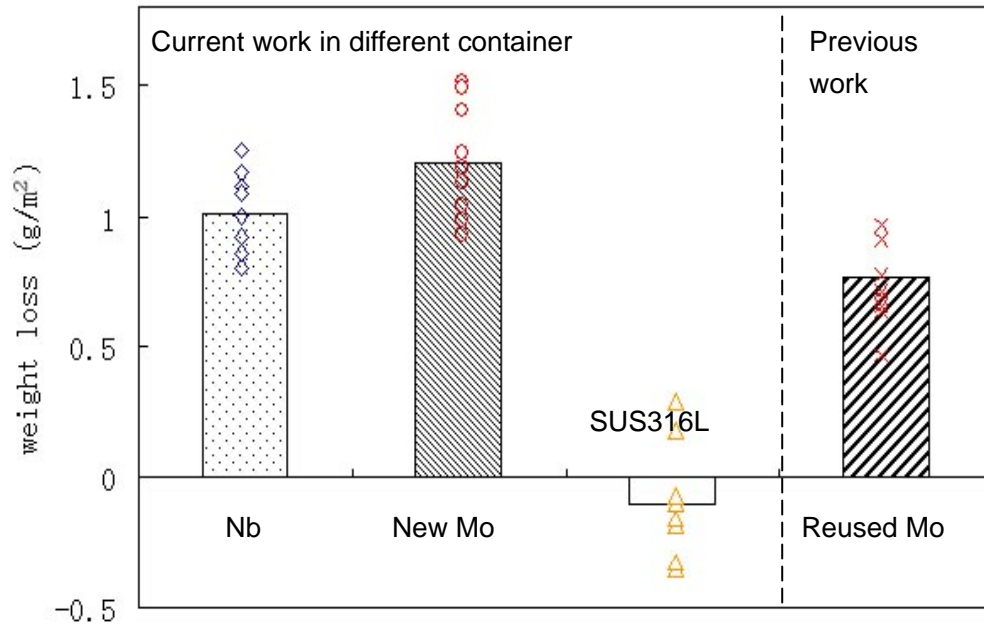
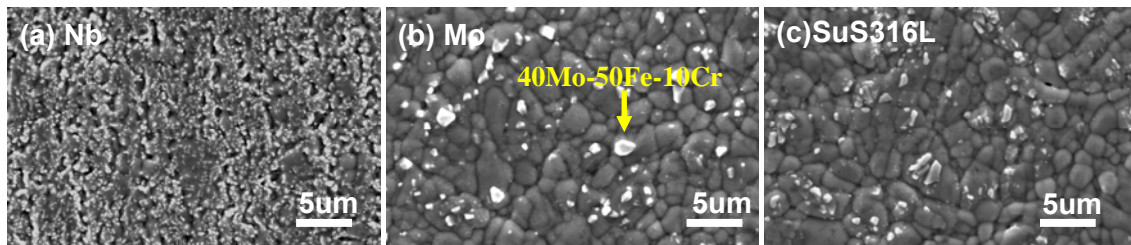Figure 5-2. The weight loss after Li exposure in different container at 600ºC 250h

Figure 5-3. SEM surface picture of specimens exposed in (a) Nb (b)Mo (c) SUS316L

Fig. 5-3 shows the surface morphology of the specimens exposed in Nb, Mo and SUS316L containers at 600ºC for 250h. The substrate of steels could be seen directly after clean with water, because the possible corrosion products, such as Li_2O, Li_9CrN_5 are soluble in water. As shown in Fig.5-3 (a), the specimens exposed in Li developed a porous surface in Nb case. Fig.5-3 (b) and (c) showed that phase transformation from matensite to ferrite was observed on the surface of specimens exposed in Mo and SUS316L container. According to the result of EDS surface analysis, the attack of Li resulted in the depletion of Cr on the surface of specimens in the all three containers.

The concentration of Cr in the surface decreased from 9% to 4~6%. After exposure in SUS316L container, around 4% of Ni was detected on surface of the specimen due to the Ni precipitation during the exposure. This could be one of the reasons that the specimens gained weight after Li exposure in austenitic steel container.

The corrosion products were observed on the surface of specimens in Mo and SUS316L cases. Ni enriched particles was found on the surface of specimens exposed in SUS316L container, as shown in Fig.5-3 (c). It might also contribute to the weight gain of the specimen. Fig.5-3 (b) showed that the Mo-Fe-Cr particles observed on the surface of specimens exposed in Mo container. The composition of these particles was around 40%Mo, 50%Fe and 10%Cr by EDS. These particles located in the sections close to the Mo wires which were used to fix the specimens. On the other hand, plenty of particles were observed on the surface of the Mo holder. Fig.5-4 (b) showed the same Mo-Fe-Cr particles covered the surface of Mo holder. These particles were also observed after 700ºC exposure on the surface of specimens and the Mo-holder, as shown in Fig.5-4(c) and (d). The composition of the particle is the same as those found at 600 ºC. The size of the particle was bigger at 700ºC than 600ºC. It's clear that high temperature promoted the growth of the particles.
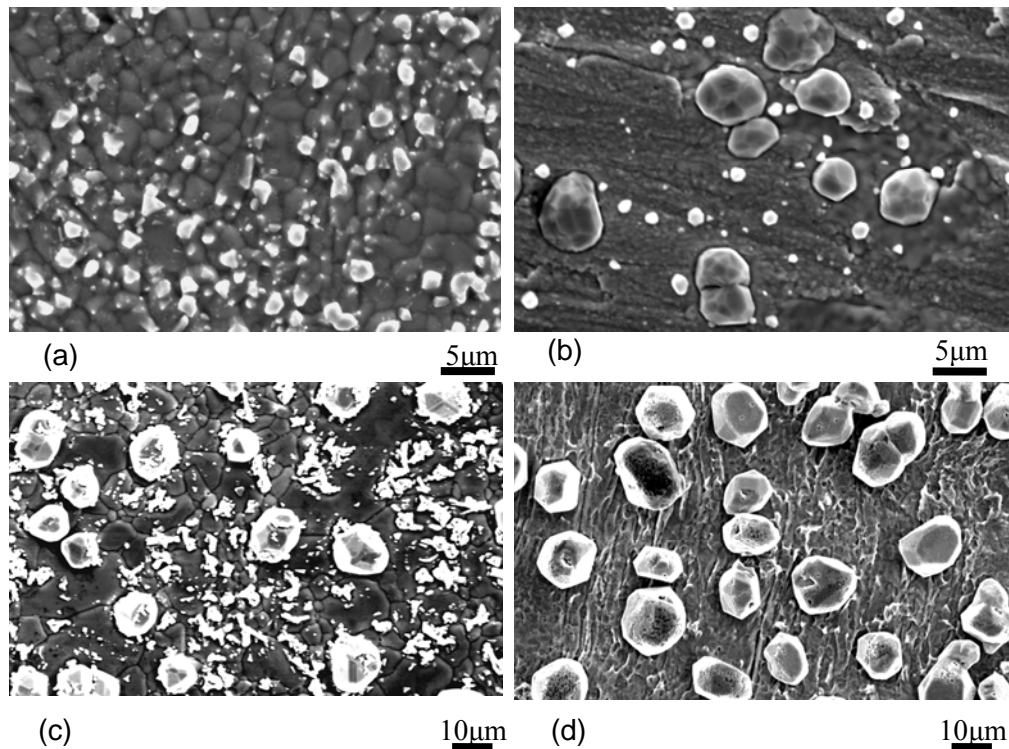
Figure 5-4. Mo-Fe-Cr particles on the surface of specimens and Mo-holder.

(a) and (b): surface of specimen and Mo-holder after 250h exposure at 600°C

(c) and (d): surface of specimen and Mo-holder after 100h exposure at 700°C

The metallographic observations and EDS line scan were carried out on the cross section of specimens to study the phase transformation in depth, as shown in Fig. 5-5. In Mo and Nb case, the phase transformation and disappearing of carbide were found. The phase transformation zone was not uniform along the edge of the specimen. On the other hand, no phase transformation was found in SUS316L container after 600°C exposure for 250h. The figures show that the depth of the phase change on JLF-1 specimens is about ~8μm and ~20μm in Mo and Nb case separately. In the phase transformation zone, the density of carbide precipitates decreased drastically. The depth of ferritic zone in Nb case is almost double that in Mo case. It seems that the Nb container strongly enhanced the phase change from martensite to ferrite during the Li exposure.
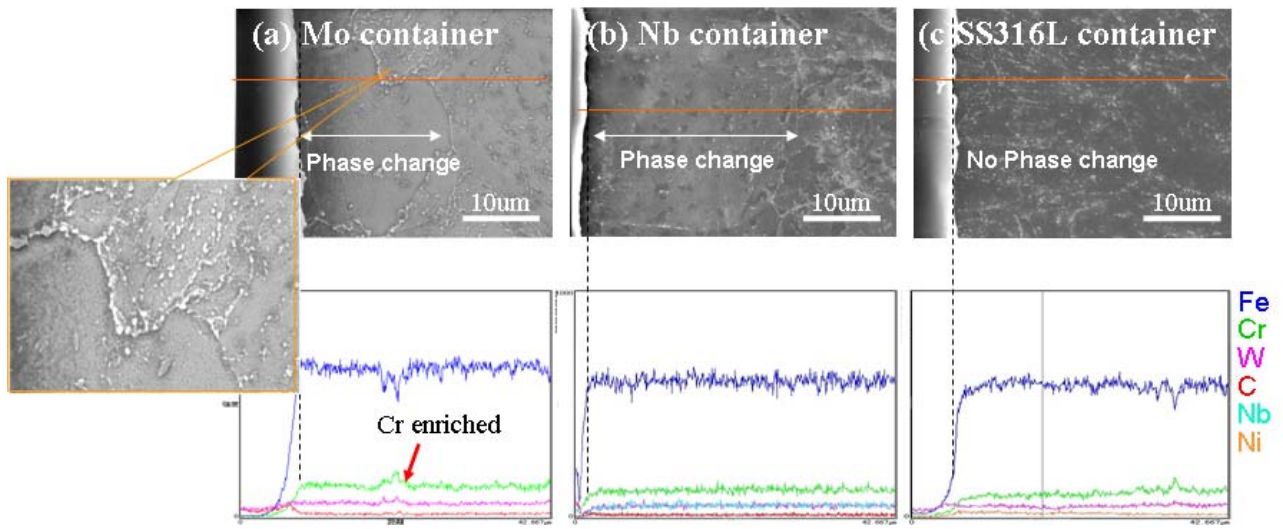
Figure. 5-5 The cross section after Li exposure in different container

The enhanced carbide was observed around phase transformation boundary, as shown in Fig.5-5 (a). According to the EDS line scan result, enrichment of Cr and W was detected in these sections. On the edge of the specimen exposed in SUS316L container, the Ni penetration was detected by EDS analysis, as shown in Fig. 5-5(c). The depth of Ni penetration zone was about 5μm. The Ni penetration seemed to be one reason that caused the weight gain after Li exposure in SUS316L.
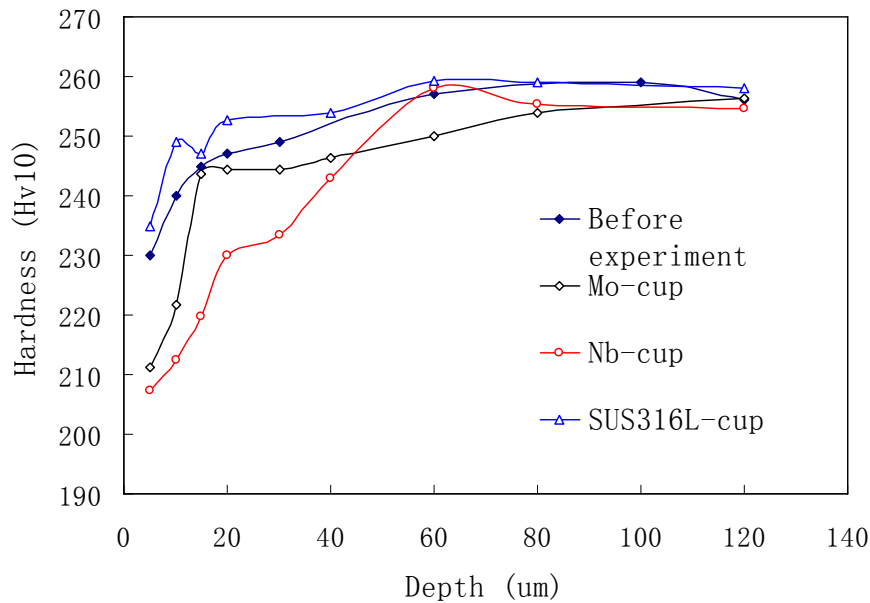
Figure 5-6. The hardness change in depth after Li exposure in different container

The Vickers-hardness measurement was carried out on the cross section to investigate the mechanical property change after Li exposure. The change of hardness in depth after Li exposure in Nb, Mo and SUS316L was presented in the Fig. 5-6. Due to edge effect, there was a reduction of hardness at the edge of specimen in all cases. The reduction of hardness was observed on the specimens exposed in Mo and Nb containers. The depth of softening was consistent with the depth of phase change. The C depletion and phase transformation from martensite to ferrite resulted degradation of mechanical properties of RAFM after Li exposure.

5.3. The role of container materials and decarburization

The gradient of C concentration in Li seemed to be the driving force of decarburization and phase transformation during the Li exposure. The decarburization is the main reason for the phase transformation from martensite to ferrite, as proved in the previous chapters. According to the cross section observation, the deepest phase change zone of around 20μm was observed on the specimens exposed in Nb container; only

6~8μm phase transformation occurred on the specimens in Mo container; however no phase change was found in SUS316L case. The thermodynamic data of carbide involved in the experiment was presented in Fig. 5-10. The order of stability of carbides is $NbC>Cr_{23}C_6>Mo_xC>Li_2C_2>Fe_3C$. It is clear that the Mo and Nb acted as C-trap during the Li exposure. They kept C concentration at very low level in Li. This promoted the dissolution of C from the steel and resulted in the phase transformation from martensite to ferrite. The thermodynamic data could explain the result that the phase transformation phenomenon was only observed in Mo and Nb cases. Because of high affinity of Nb and C, the most significant phase transformation was found in Nb container. The Vickers hardness test result agreed with the result of SEM observation. In Nb case, the most obvious reduction of hardness was detected, and the softening range was consistent with the phase transformation depth. Almost no reduction of hardness was found on the specimen exposed in SUS316L container.
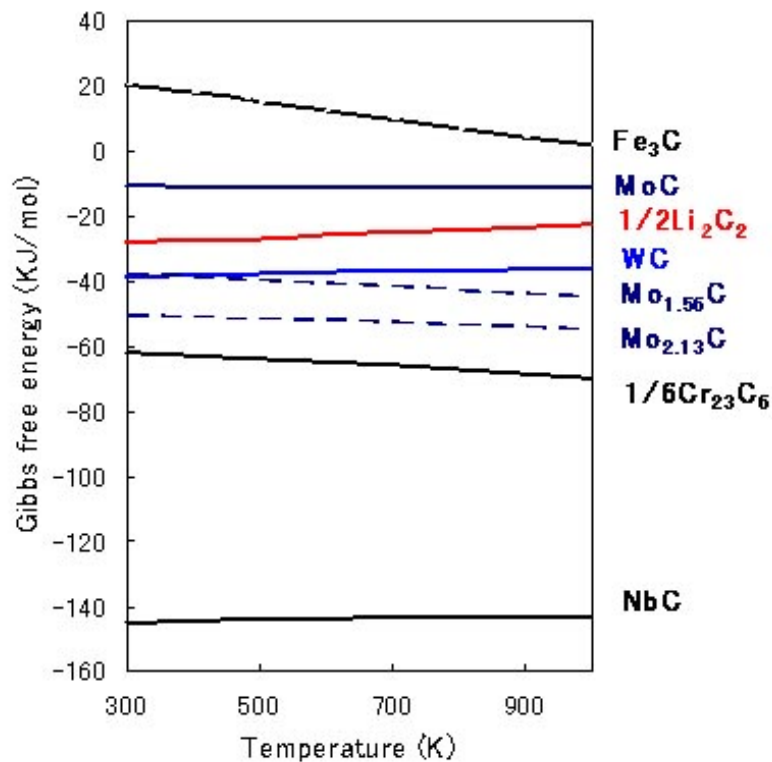
Figure 5-10. Thermodynamic data of several carbides

In the metal, C diffused from internal part to surface under the gradient of C concentration. Following the dissolving of C into Li, the C concentration became too low to keep the carbides stable in the specimen. This could lead to the decomposing of carbides, such as $Cr_{23}C_6$. Considering the low C concentration in bcc (0.02%), the formation of ferrite would promote the dissolution of C to Li. After the decomposing of carbides, the free Cr atom moved both to surface and the internal side under the gradient of free Cr atom. In the internal side of the specimen, the Cr captured C and formed new carbide. These carbides accumulated along phase change boundary or on the original austenitic grain boundary because of low formation energy, as shown in Fig. 5-11. Following the diffusion of C and the disappearing of carbides, the layer of ferrite grows up.
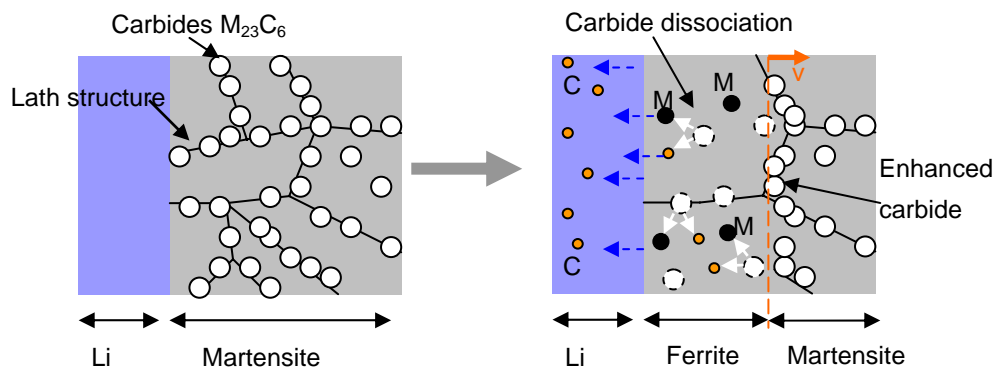
Figure 5-11. The growing up of ferrite in specimen

5.4 Summary

1) Weight loss was found in Mo and Nb containers, while weight gain was found in SUS316L container due to the precipitation and penetration of Ni from container materials

2) Mo acted as C-trap and resulted in phase transformation of JLF-1 specimen from martensite to ferrite during the exposure. The reaction among container materials, Fe and Cr took place in Mo container, but not in Nb container.

3) After the exposure in SUS316L container, phase transformation was very thin. The most significant phase transformation was observed in Nb container, because of high affinity of Nb with C.

4) The distribution of dissolved alloy elements in Li was not uniform. The inhomogeneous Li chemistry can cause data scatter.

5) The whole system, including specimens, Li, container materials and inhomogeneous Li chemistry should be taken into consideration when compatibility performance is characterized.

Chapter 6

Discussion and Modeling of corrosion behavior
of JLF-1 in Li

In the previous chapters, the corrosion characteristics were investigated in static and flowing conditions. In this chapter, the discussions on some factors affecting the corrosion are carried out. Furthermore, the models are developed to explain the corrosion and the growth of phase transformation layer.

6.1 N effect on the corrosion

6.1.1 N level in Li

Plenty of experiments proved that the non-metal impurities, especially N, have a strong impact on the corrosion behavior by forming binary or ternate compounds. [56,63,64] This could significantly increase the solubility of many elements in Li, such as C, Cr, Fe, etc, by the chemical equations:[51]

$$2Li_3N + Fe \ = \ Li_3FeN_2 + 3Li \qquad (1)$$
$$5Li_3N + Cr \ = \ Li_9CrN_5 + 6Li \qquad (2)$$
$$4Li_3N + Li_2C_2 \ = \ 2Li_2NCN + 10Li \qquad (3)$$
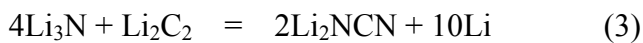
Therefore, N is highly suspected to cause the weight loss and decarburization. To investigate the role of N and alloy elements in liquid Li, the chemical analysis of Li was carried out before and after the experiments in Mo and in SUS316L containers at 600ºC for 250h. Furthermore, the Li in upper part and bottom part was analyzed separately to figure out the element distribution in the static system. The result of chemical analysis is given in table 6-1. For comparison, the result of chemical analysis of Li after exposure at 700ºC for 100h is also shown in this table.

Table 6-1 Composition of Li before and after exposure (wppm)

	Before exposure	After exposure in Mo container 600ºC 250h		After exposure in SUS316L container 600ºC 250h		Mo container 700ºC 100h
		Upper	Bottom	Upper	Bottom	
Fe	0.85	0.7	1.7	1.2	1.5	2
Cr	0.12	0.17	0.48	0.22	0.42	0.04
Ni	0.80	6.6	6.4	12	14	5
Mo	0.11	0.47	0.95	<0.01	1.1	0.32
W	0.31	1.4	1.5	0.15	2.1	0.39
N	65	30	60	40	80	**630**

As shown in Table 6-1, the concentration of N in Li is lower than 100ppm at 600ºC, while the N level goes up to 630ppm (roughly ten times higher) at 700ºC. The concentration of elements was not uniform in the container. The bottom part contained more elements than upper part. It seems that the heavy alloy elements deposit in bottom part due to gravity effect in Li. The possible small temperature gradient between upper part and bottom part of the container may also contribute to the inhomogeneous Li chemistry during the static exposure. The difference of concentration of the alloy constituent elements and the impurities by position resulted in the scatter of weight loss data.

It was reported that the impact of N was limited when N level is lower than 100ppm.[39,51] When concentration of N is lower than 65wppm, there is no reaction between Cr and N. [70] Therefore, the N level was usually controlled below 100ppm to suppress the impact of N in previous corrosion tests.[40,41,56] On the other hand, it was reported that the corrosion drastically increased with the increase of N concentration.[41] When concentration of N increased from 100 to 200ppm, the weight loss increased 2~4 times.

In the current experiment, level of N was very high in Li at 700ºC. The probable

chemical reaction may strongly promote the dissolution of alloy elements and depletion of C. Furthermore, the reaction products, such as Li_3FeN_2, Li_9CrN_5 and Li_2NCN, may deposit on the bottom of the container because of large mass. This process keeps low concentration of alloy elements and compounds in upper part of the container and results in further corrosion. Therefore JLF-1 steel suffers from severe corrosion at 700ºC. On the other hand, at 600ºC, it is believed that the impact of N in current experiment is limited in static Li, because N level is low in these cases. The source of N may come from the penetration of N_2 through the sealing part of SS316 pot at high temperature. The N released from the SS316 pot is another possible source of N contamination.

Table 6-2 Chemical analysis results of JLF-1 exposed in static Li (wt%)

	C	Cr	W	N	Fe
Before exposure	0.09	8.92	2.00	0.01	balance
700ºC 100h	0.03	8.88	1.95	0.01	balance
600ºC 250h	0.09	8.83	1.93	0.02	balance
500ºC 250h	0.09	8.80	1.95	0.01	balance

The compositional change on JLF-1 specimens was also measured after Li exposure at 500, 600 and 700ºC. The result is given in table 6-2. Because the compositional change occurs only near the surface of the specimen, the composition change of whole specimens is not obvious after Li exposure. The only exception is the case of 700ºC in which 2/3 of C dissolved into Li. In this case, almost whole specimen changed from martensite to ferrite, as shown in Fig.3-4 (b). No N penetration on the specimen was observed in any cases.

6.1.2 Estimation of N effect on weight loss

By chemical analysis, 60wppm N was found in Li (bottom part) after exposure at 600ºC, as shown in Table 6-1. Assuming that all the 60wppm N reacts with Fe following

the equation (1), 119wppm Fe will dissolve into Li. The concentration of Fe in Li is $Cs_1=60g/m^3$ (119Wppm).

On the other hand, the solubility of Fe and Cr in Li at 700°C are 16.0wppm (4appm) and 14.6wppm (4appm) respectively at 600°C. [52] If Fe and Cr dissolve in Li independently, the total concentration $Cs_2 = 15g/m^3$ (16.0+14.6=30.1wppm) assuming no reaction with N.

The weight loss of the specimen is a function of time and is expressed as:

$$\triangle m(t) = JSt \qquad (4)$$

Where J $[g/m^2 \cdot sec]$ is flux of dissolution elements; $S = 2.9 \times 10^{-4} [m^2]$ is surface area contact to Li; t [sec] is the exposure time.

From the experimental result, the average flux at 600°C for 100h is

$$J = 1.49 \times 10^{-6} g/m^2 s \quad (5)$$

The dissolved elements diffuse to bulk Li flowing the Fick's first law:

$$J = K(Cs-C(t)) \qquad (6)$$

Where Cs $[g/m^3]$ is the concentration of alloy element at the interface of specimen and Li; C(t) $[g/m^3]$ is the concentration of alloy elements in bulk Li at time t. The flux also can be shown as:

$$JS = V(dC(t)/dt) \qquad (7)$$

V $[m^3]$ is the volume of Li. In this work, ~92cm³ (~46.0g) Li was use in each static exposure.

$$K(Cs-C(t)) = (V/S) (dC(t)/dt) \qquad (8)$$

$$C(t) = Cs(1-Aexp(-KSt/V)) \qquad (9)$$

$$\triangle m(t)/S = VCs (1-Aexp(-KSt/V))/S \qquad (10)$$

When Fe reacts with N, a marginal condition of t=0, C(t) = 0.425 g/m^3 (Fe concentration in Li before experiment, 0.85wppm , from Table 6-1) and $Cs_1 = 60g/m^3$ is used in equation (6) and (9), and the following values are obtained

$A_1 = 0.99289; K_1 = 2.50 \times 10^{-8}$

When alloy elements dissolute without N reaction, a marginal condition t=0, C(t)=0.425 g/m^3 (Fe concentration in Li before experiment, 0.85wppm , from Table 6-1) and Cs$_2$ = 15g/m^3 is used in eq.(6) and (9), and then,

$A_2 = 0.971667; K_2 = 1.01 \times 10^{-7}$

Solving equation (10), Fig 6.1-1 is obtained. The experimental data at 600ºC are shown to compare with the estimation. The figure shows that the estimated rate of the weight loss decreases with the exposure time. This agrees with the experimental result and describes the saturation happening in the static test. The estimation by N reaction shows higher weight loss than that by solubility data. This means the existence of N can obviously enhance the corrosion at 600ºC. It seems that the estimation fit well the experimental result after the short term exposure of 100h and 250h. However, for long term exposure, the experimental data seem to be much lower than estimation by N reaction concept. It is possible that other factors affect the estimation of the weight loss in Li at 600ºC. This will be discussed later in 6.2.
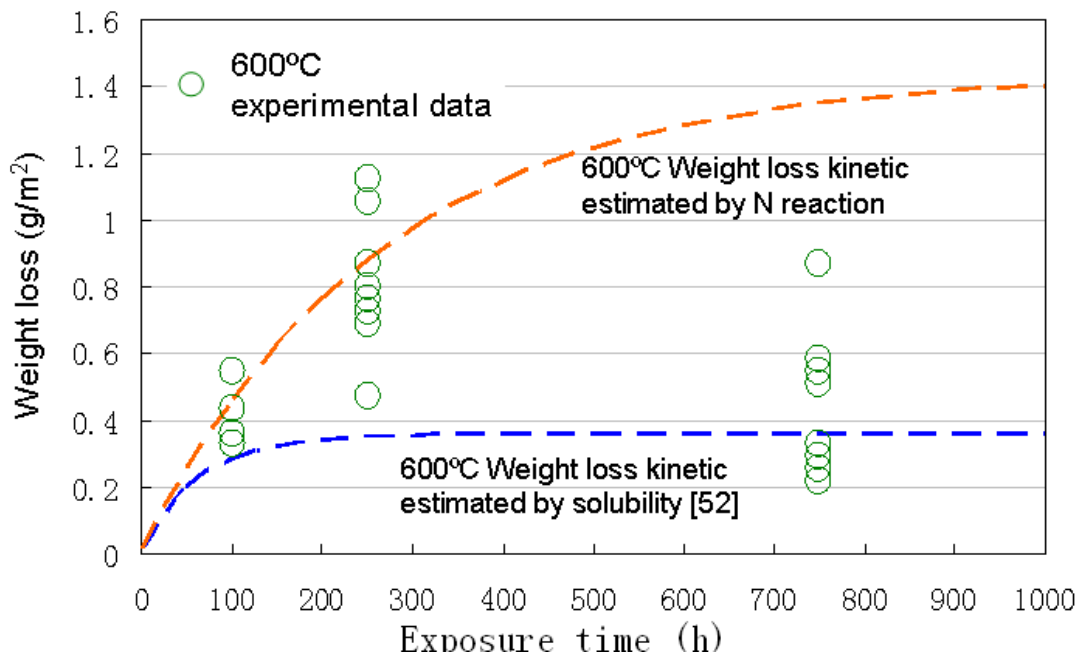
Figure 6.1-1 Estimation of weight loss kinetics at 600ºC

By the same method, the kinetics of weight loss at 700ºC was estimated. 630wppm N was detected in Li after exposure at 700ºC. After the chemical reaction following the equation (1), 1296wppm Fe will dissolve into Li. The concentration of Fe in Li is Cs_3=648g/m^3 (1296wppm).

The literature data shows that the solubility of Fe and Cr in Li at 700ºC are 31.0wppm (4appm) and 29.1wppm (4appm) respectively.[52] The total concentration is $Cs_4 = 30.7$g/m^3 (31.0+29.1 = 60.1wppm), without N reaction.

From equation (4), the flux at 700ºC for 100h is:

$J = 67.4 \times 10^{-6}$g/m^{2}s

When a marginal condition t=0, C(t) = 0.425 g/m^3 (Fe concentration in Li before experiment, 0.85wppm , from Table 6-1) and $Cs_3 = 648$g/m^3 is used in equation (6) and (9), and the following values are obtained

$A_3 = 0.99934$; $K_3 = 0.25 \times 10^{-8}$

When a marginal condition t=0, C(t)=0.425 g/m^3 (Fe concentration in Li before experiment, 0.85wppm , from Table 6-1) and $Cs_4 = 30.7$g/m^3 is used in eq.(6) and (9), and then,

$A_4 = 0.98609$; $K_4 = 1.34 \times 10^{-6}$

Solving equation (10), the results are shown in Fig 6.1-2. The estimated kinetic curve shows the saturation effect in static test. The weigh loss rate reduces with exposure time. The figure suggests that the JLF-1 suffers from severe corrosion at this temperature because of the reaction with high level of N in the Li.
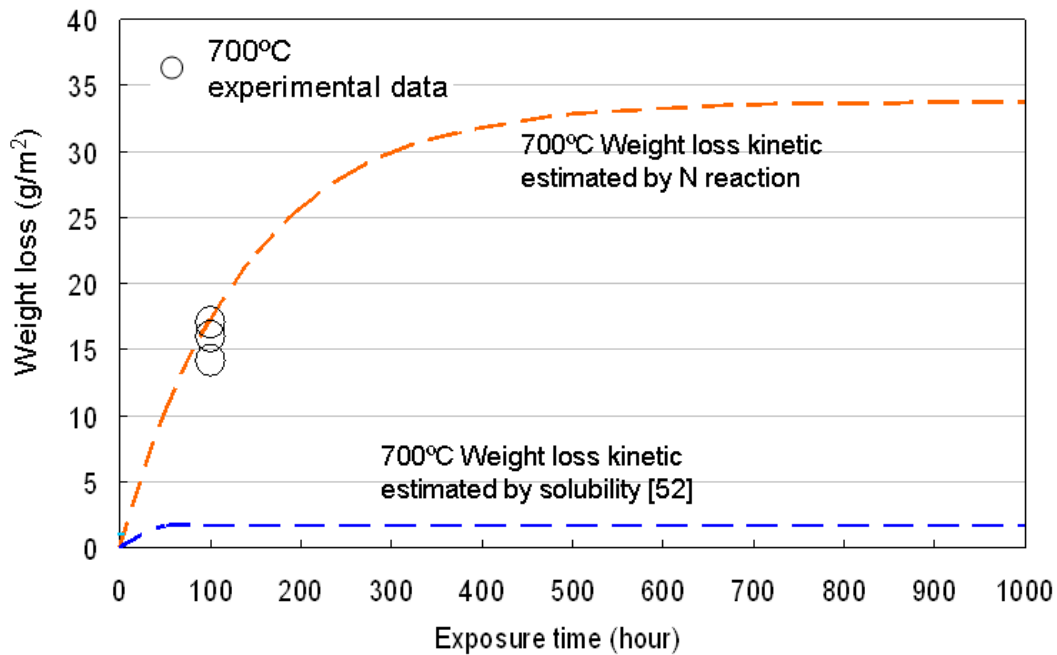
Figure 6.1-2 Estimation of weight loss kinetics at 700ºC

6.2 Dissolution of Mo

It is usually considered that Mo has good resistance to Li. So Mo was selected as the container in the present Li experiment. However, after Li exposure, Mo-Fe-Cr particles were observed on both Mo-holder and specimens, as shown in Fig.5-4. The particles were well developed crystal particles under SEM. It adhered firmly on the surface of the Mo-holder and the specimens after cleaning with flowing water followed by ultrasonic cleaning in acetone. These particles grew with temperature. The formation of the Mo-Fe-Cr particles indicated that the interaction between the Mo, Li and JLF-1 took place during the exposure to Li.

The dissolution of Mo in Li was investigated by the method of electro-transfer which is very sensitive to the form (state) of components into liquid solution.[67] The result shown in Fig.6-1 concluded that the solubility of Mo sharply increases when N level in liquid lithium exceeds 0.1 at% (at 1000° C). Experimental data showed that the formation of relatively stable triple complex Mo-N-Li is the reason for the additional

dissolution of Mo in the lithium.[67] After corrosion test of Cr-Mn steel in pure Li in Mo container at 600°C, the Mo enriched in corrosion products (63.8 Mo, 26.4 Fe, 4.8 Cr, 5.0 Mn) was found.[73] The experimental data illustrate that Mo is soluble when non-metal elements, such as N and C exit in Li at 600-700ºC.
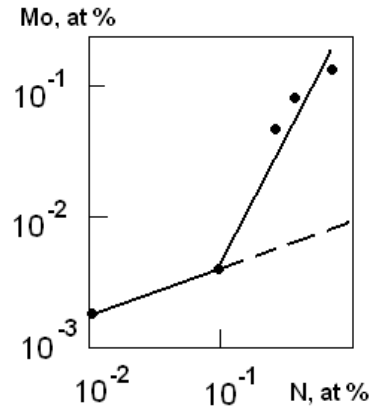
Figure 6.2-1 Solubility of Mo in Li depending on nitrogen content

in liquid metal (1000º C), [67]
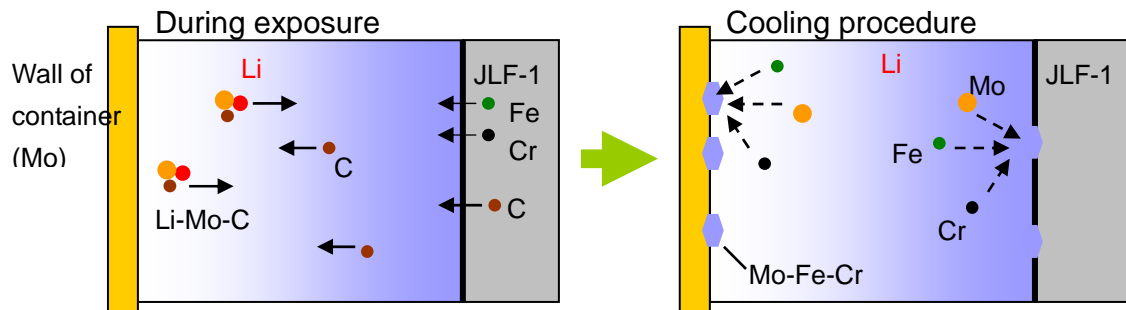
Figure 6.2-2 Formation of Mo particle

The probable process of the formation of Mo particle is described in Fig. 6.2-2. The C dissolves from JLF-1 into Li during the exposure. The non-metal impurities move to Mo under the concentration gradient and form the Li-Mo-C triple complex. This enhances the dissolution of Mo into Li. During the cooling procedure, the Mo precipitates on the surface of specimen as Mo-Fe-Cr particles. On the other hand, no Nb compound was found in Nb container. It seems that Nb is quite stable to Li attack.[68]

To study the impact of Mo corrosion products on the weight change, the

estimation of the weight of Mo particles was carried out. The size, density and distribution of Mo particle were used to evaluate the weight of Mo. The distribution of Mo particle was examined on the specimens exposed in new and reused Mo container at 600ºC for 250h and 750h. The sketch of distribution was presented in Fig 6.2-3.

(a) 250h exposure in Mo container   (b) 750h exposure in Mo container
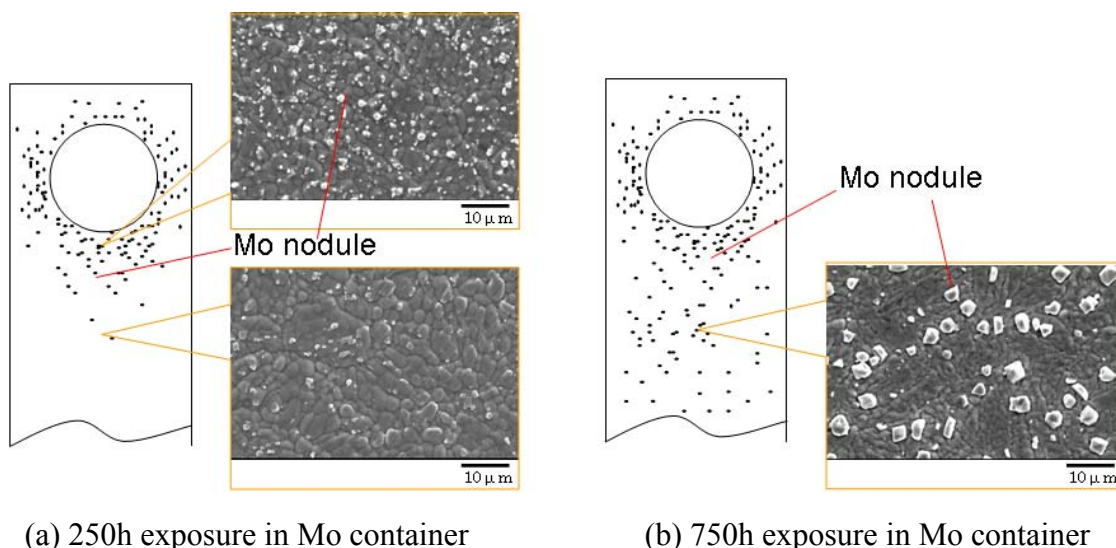
Figure 6.2-3 Distribution of Mo particle on the specimen exposed at 600 ºC in Mo container

As shown in Fig. 6.2-3, after exposure in Mo container for 250h, majority of Mo particles were located in the range of 500μm from the specimen hole where the Mo wire goes through. Closer to Mo wire, more Mo particles were formed. After long time exposure at 750h, the Mo particles were observed on whole surface of the specimens. The size of Mo particle was obviously larger than that in short term exposure. This may be because more Mo dissolved into Li during the long term exposure. The average distribution of Mo particles on the surface of the specimen is figured out, as shown in Fig. 6.2-4. After long time exposure, a large amount of Mo particles were observed compared with the specimens exposed for 250h.
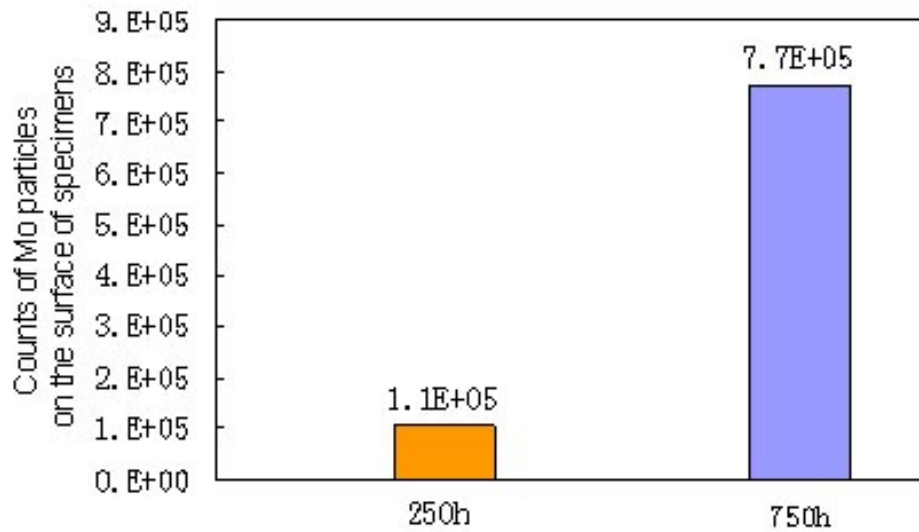
Figure 6.2-4 Estimated number of Mo particle on the surface specimen

The density of Mo particle was estimated as follows:

$$d_{Mo-nodle} = d_{Mo} \times 40\% + d_{Fe} \times 50\% + d_{Cr} \times 10\% \qquad (11)$$

d_{Mo}, d_{Fe}, d_{Cr} : as the density of pure Mo, Fe and Cr separately

The average sizes of Mo particles are:

(1) Exposure for 250h in new Mo container $\qquad \overline{D}_1 \sim 3 \mu m$

(2) Exposure for 750h in reused Mo container $\quad \overline{D}_3 \sim 4 \mu m$

Using the data provided above, the impact of Mo particles on the weight loss was shown in Fig. 6.2-5.
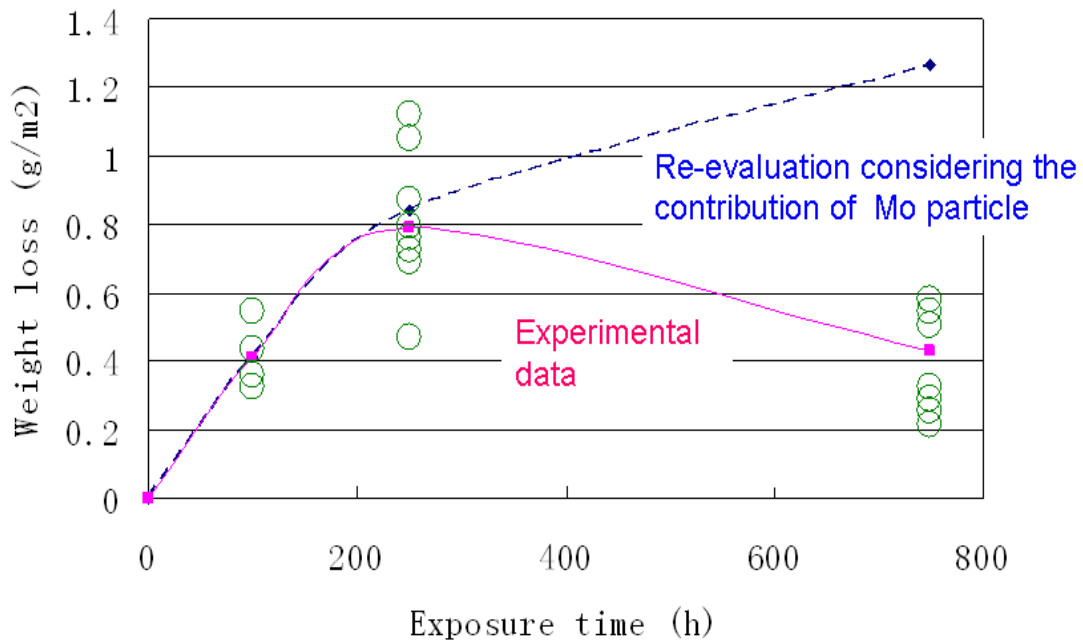
Figure 6.2-5 Impact of Mo particles on the weight loss at 600ºC

The figure shows that the weight loss rate of JLF-1 specimens reduces with exposure time at 600 ºC, because of the saturation of bulk Li in static condition. Contrary to previous conclusion, the weight loss has not suspended completely, if the weight of Mo particles on the surface of specimens was removed.

The estimation of N effect on corrosion in Chapter 6.1 is compared in Fig. 6.2-6. It can be seen that the re-evaluated weight loss considering the contribution of Mo particle fits the estimation of N reaction well. This illustrates that the N effect still cause continuous weight loss after exposure in Li for 750h. The corrosion in static test was not controlled by the solubility of alloy elements, but by the N level in Li at 600ºC as well as at 700ºC. The N reaction reduced the level of alloy elements in Li and promoted the corrosion.
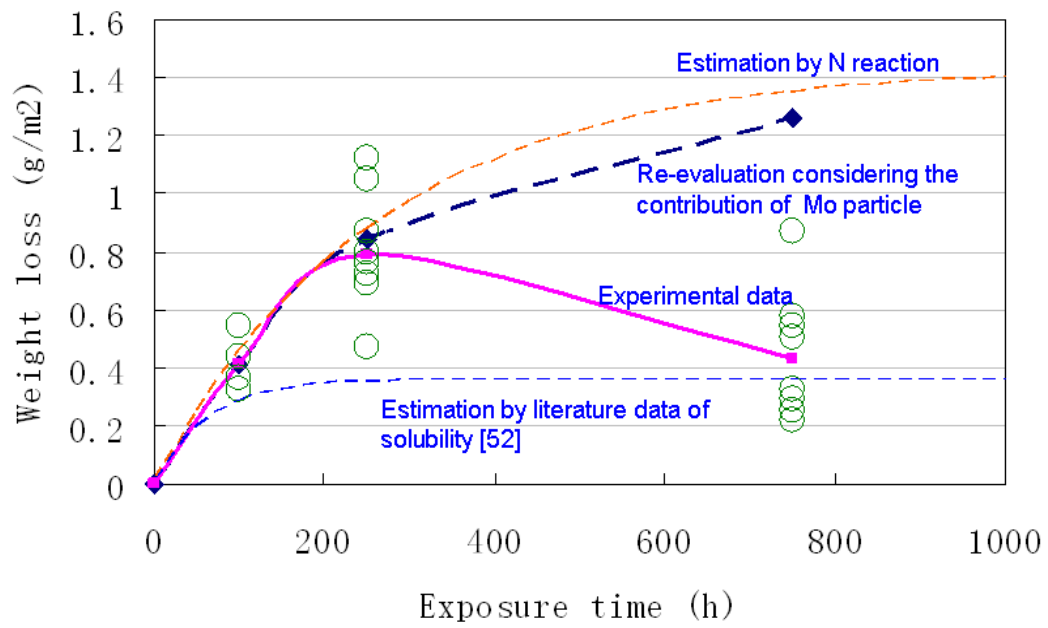
Figure 6.2-6 effect of N and Mo particles on weigh loss at 600ºC

6.3 Depletion of C and phase change

According to the previous chapters, one of concerns raised for RAFM exposed to Li is the phase change from martensite to ferrite, which led to a significant degradation of mechanical properties. Chemical analysis showed that the loss of C is the main reason causing the phase change. In this section, the behavior of C during the Li exposure is discussed.
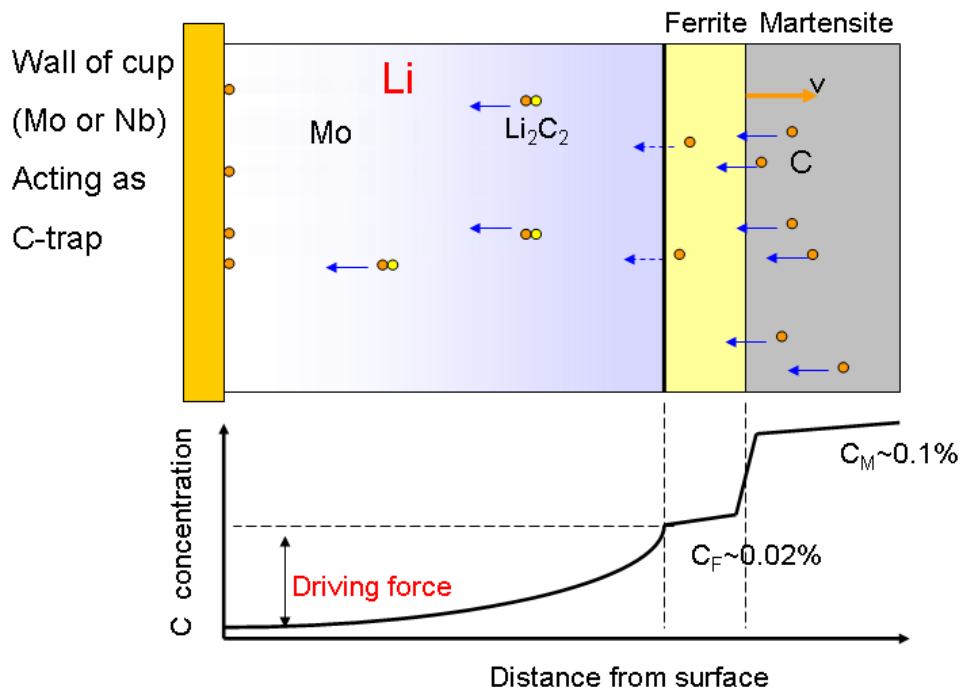

Figure 6.3-1 the model of C depletion

The model of the behavior of C was described in Fig. 6.3-1. It has been realized that the depletion of C into Li is not a simple dissolution, but a chemical reaction. Several C related chemical reactions take place on the surface of JLF-1 specimen and on the surface of the container materials during the corrosion test. The behavior of C is decided by the chemical potential in each reaction. The possible chemical reactions on the surface of JLF-1 are:

①. $0.33\ Cr_{23}C_6 + 2\ Li = 7.66Cr + Li_2C_2$

②. $2W_2C + 2Li = 4W + Li_2C_2$

③. $2C + 2Li = Li_2C_2$

④. $2Fe_3C + 2Li = 6Fe + Li_2C_2$

The spontaneity of a reaction at constant temperature and pressure can be judged by the reaction Gibbs energy ΔrG:

If $\Delta rG < 0$, the forward reaction is spontaneous,

If $\Delta rG > 0$, the reverse reaction is spontaneous,

If $\Delta rG = 0$, the chemical potential of, the reaction is at equilibrium.

For reaction $\quad\quad aA + bB = cC + dD$

The ΔrG can be obtained by flowing equation:

$$\Delta_r G = \Delta_r G^0 + RTlnK = \Delta_r G^0 + RTln\frac{c_A^a \cdot c_B^b}{c_C^c \cdot c_D^d}$$

ΔrG: reaction Gibbs energy (kJ·mol^{-1});

ΔrG^0:   standard Gibbs energy (kJ·mol^{-1});

K: equilibrium constant;

R: constants (8.314 kJ·mol^{-1}·K^{-1})

$C_{A\ (B,\ C,\ D)}$:   the concentration of certain compound.

The standard reaction Gibbs free energy can be got from data base.[66] For the reaction ③, the reaction Gibbs energy can be shown as:

$$\Delta_r G_3 = \Delta_r G^0_{\ 3} + RTlnK = \Delta_r G^0_{\ 3} + RTln\frac{(c_{Li_2C_2})^1}{(c_{Li})^2 \cdot (c_C)^2}$$

Since Li is a pure mono-atomic metal, $C_{Li}=1$. The concentration of Li_2C_2 of 1ppm is assumed at the beginning of reaction. Then we can get actual reaction Gibbs energy by different concentration of C. The reaction Gibbs free energy for reaction ①~④ are presented in Fig. 6.3-2.[66]
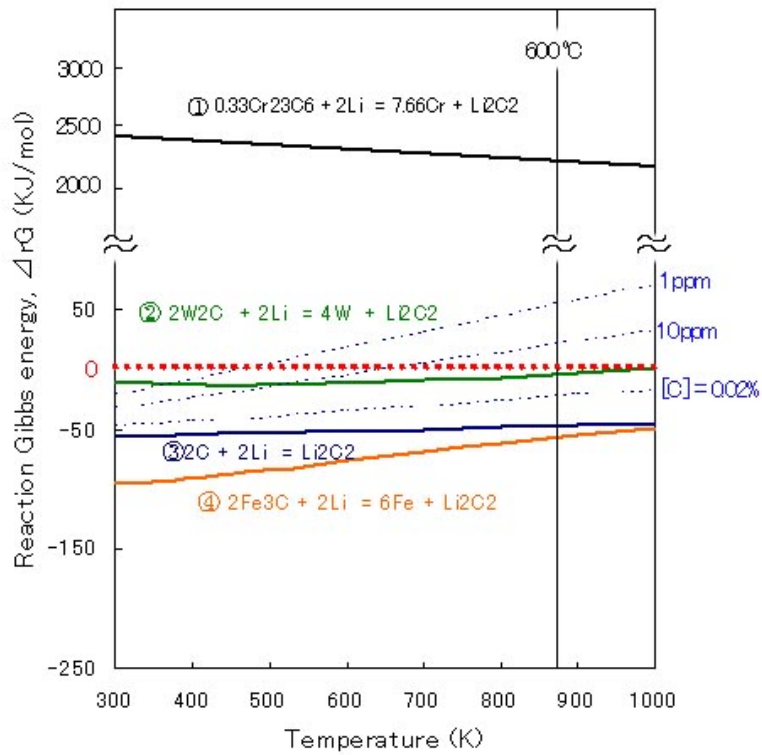
Figure 6.3-2 Gibbs energy of chemical reaction on the JLF-1 surface [66]

According to the figure, the standard reaction Gibbs energy (the concentration of all reactants and products are 1mol) of ②, ③ and ④ are lower than 0. This means that reaction ②, ③ and ④ are spontaneous in standard situation. The reaction ① cannot happen because of the high affinity between Cr and C. For reaction ③, actual reaction Gibbs energy with various concentration of C is presented in dots lines. This shows that the actual reaction Gibbs energy increases with the reduction of C concentration. When the actual reaction Gibbs energy comes to zero under certain temperature, this reaction will go to reverse direction. This can be expressed as the following equation at 600ºC:

$$\Delta_r G_3 = \Delta_r G^0{}_3 + RT\ln \frac{(c_{Li_2C_2})^1}{(c_{Li})^2 \cdot (c_C)^2} \qquad (12)$$

$\triangle_r G^0{}_3 = 0$, $\triangle_r G^0{}_{3(873K)} = -46.74$(KJ/mol); T = 873K, R=8.314(kJ/mol·K)

Then, C_c = 44ppm (mol ratio)

This indicates that reaction ③ will stop at 600ºC when concentration of C is lower than 44ppm (mol ratio) in steel. The minimum concentration of W_2C and Fe_3C are calculated to be 790ppm (mol) and 20ppm (mol) respectively at 600ºC. When the concentration of W_2C and Fe_3C are blow those levels, the attack of Li on W_2C and Fe_3C will be suspended.

The possible chemical reactions on the surface of container are:

⑤.　$6Fe + Li_2C_2 = 2Fe_3C + 2Li$　　　　(SUS316L container)

⑥.　$4Mo + Li_2C_2 = 4MoC_{0.50} + 2Li$　　(Mo container)

⑦.　$2Nb + Li_2C_2 = 2NbC + 2Li$　　　　(Nb container)
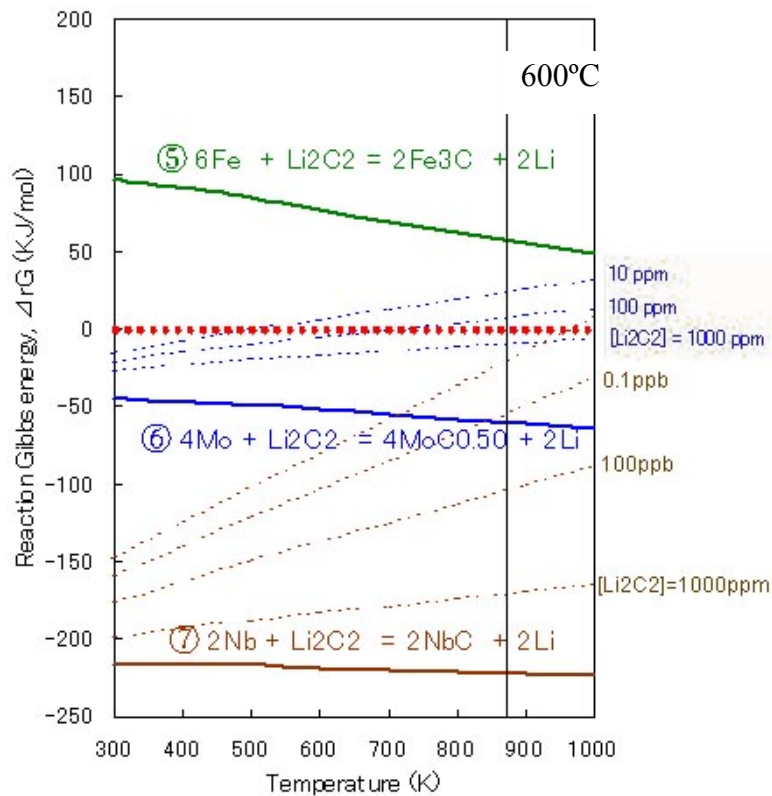
Figure 6.3-3 Gibbs energy of chemical reaction on the container surface [66]

The reaction Gibbs energy of these chemical reactions is presented in Fig. 6.3-3.[66] It illustrates that Mo and Nb tend to capture the C from Li when Mo and Nb

are used as container material for Li corrosion test. On the other hand SUS316 container does not react with Li_2C_2, because the reaction between Fe and Li_2C_2 is not a spontaneous reaction. This is consistent with SEM and EDS results in the previous chapter. Although both Mo and Nb act as C-trap during the Li exposure, Nb is a much stronger trap than Mo. When the reaction ⑦ goes to equilibrium, the C concentration on the surface of Nb can be calculated by:

$$\Delta_r G_7 = \Delta_r G^0{}_7 + RT \ln \frac{(c_{NbC})^2 (c_{Li})^2}{(c_{Nb})^2 (c_{Li_2C_2})} \qquad (13)$$

$\Delta_r G^0{}_7 = 0$, $\Delta_r G^0{}_{7(873K)} = -221.9$(KJ/mol); T = 873K, R=8.314(kJ/mol·K)

$C_{Nb} = C_{Li} = C_{NbC} = 1$

Then, $C_c = 1.3 \times 10^{-13}$ ppm (mol ratio)

The thermal calculation indicates that the reaction is suspended when the concentration of C near Nb surface is 1.3×10^{-13} (mol ratio) at 600ºC. By the same method, the corresponding C concentration near the Mo surface is estimated to be 2.8×10^{-4} (mol ratio) at the same temperature. The huge gradient of C concentration caused by Nb is the main driving force for significant migration of C and phase change on JLF-1 specimen in Nb container.

According to the above thermodynamic discussion, the migration of C becomes clear. The chemical reaction between Li and C causes the dissolution C from JLF-1 steel to Li. C dissolves into Li in the form of lithium carbide. The Li_2C_2 diffuses from surface of specimen to bulk Li and make the bulk Li saturated when SUS316L was used as a container. In the cases of Nb and Mo containers, the container materials act as C-trap and lead to continuous dissolution of C. The gradient of C concentration is the driving force of C migration from martensite to container materials. Especially, Nb container keeps the C concentration in Li very low and results in significant depletion of C in JLF-1. This procedure was shown in Fig. 6.3-1.

In the alloy side, continuous loss of C results in a phase change froms martensite

to ferrite in Mo and Nb container. A ferrite layer is formed on the surface of JLF-1 specimen. The depth of ferrite layer increases with exposure time. It should be notified that the solubility of C in martensite and ferrite are much different. Martensite contains more C than ferrite and the maximum solubility of C in ferrite is only around 0.02%. This means that the C will be driven out from the matrix of ferrite when phase change happened. This makes evaluation of C behavior in JLF-1 more complex, as well as the difference in diffusion coefficient of C in martensite and ferrite.

Fig. 6.3-4 shows a model on depletion of C. Here it is assumed that (1) the diffusion-controlled C transfers from the material to Li; (2) no carbon saturation in Li side on the JFL-1/Li interface.
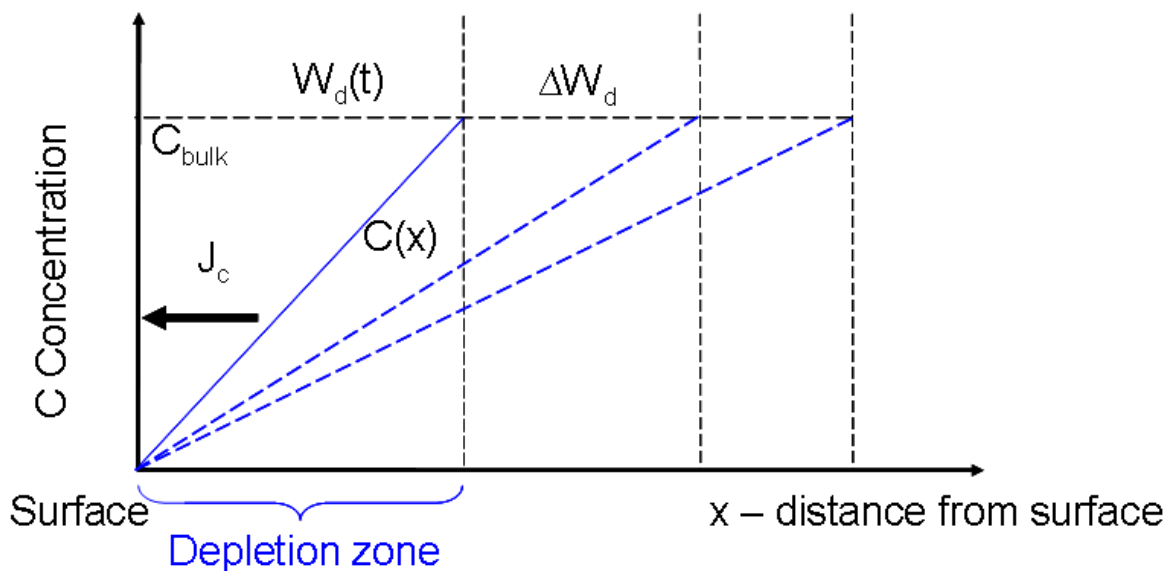
Figure 6.3-4 the model for depletion of C

Jc : flux of C   **Wd(t)** : thickness of C depletion zone

C bulk : C concentration in steel   **Dc** : diffusion coefficient of C in steel

C (x) : C concentration in C deletion zone

$$
\begin{cases}
J_c = D_c \cdot \dfrac{d[c(x)]}{dx} = D_c \cdot \dfrac{c_{bulk}}{W_d(t)} & \text{Flux proportional to the gradient of C concentration} \\
\\
J_c = \dfrac{c_{bulk}}{2} \cdot \dfrac{d[W_d(t)]}{dt} & \text{Flux equals to depletion rate of C}
\end{cases}
$$

$$\frac{d[W_d(t)]}{dt} = \frac{2}{c_{bulk}} \cdot D_c \cdot \frac{c_{bulk}}{W_d(t)} = 2D_c \cdot W_d(t)^{-1}$$

The kinetics of depletion of C following:

$$d[W_d(t)^2] = 4 \cdot D_c \cdot dt$$

$$W_d(t) = 2\sqrt{Dt} \qquad \text{(Parabolic law)} \qquad\qquad (1)$$

The extension of the depletion zone of C obeys parabolic law. Because the depletion of C led to phase change from martensite to ferrite, the growth of ferrite layer also follows parabolic law

The diffusion coefficient can be counted by Arrhenius Equation:

$$D = D_0 \cdot \exp(-\frac{Q}{kT})$$

D: Diffusion Coefficient

Do: Pre-Exponential term

Q: Activation Energy for Diffusion

k: Boltzmann Constant ($0.86 \times 10\text{-}4$ eV/K)

T: Absolute Temperature (K)

Put in the equation (1) and the experimental data

$T_1 = 500ºC$, $\quad t_1 = 250h$, $\quad$ depth of phase change W1= 10 μ m.

$T_2 = 700ºC$, $\quad t_2 = 100h$, $\quad$ depth of phase change W2= 100 μ m, then:

$$\begin{cases} \dfrac{10^2}{250} = D_0 \cdot \exp(-\dfrac{Q}{773k}) \\[3mm] \dfrac{100^2}{100} = D_0 \cdot \exp(-\dfrac{Q}{973k}) \end{cases}$$

Solute this equation and get

$$\exp(-\frac{E_m}{k}(\frac{1}{773}-\frac{1}{973}))=0.004$$
$$Q=1.79(eV) \qquad D_0=5.2\times10^{-5}(m^2/s)$$

With Q and D_0, the diffusion coefficient at certain temperature can be calculated. The diffusion coefficient of C in JLF-1 is compared with that in α-Fe and γ-Fe [69] in Fig.6.3-5.

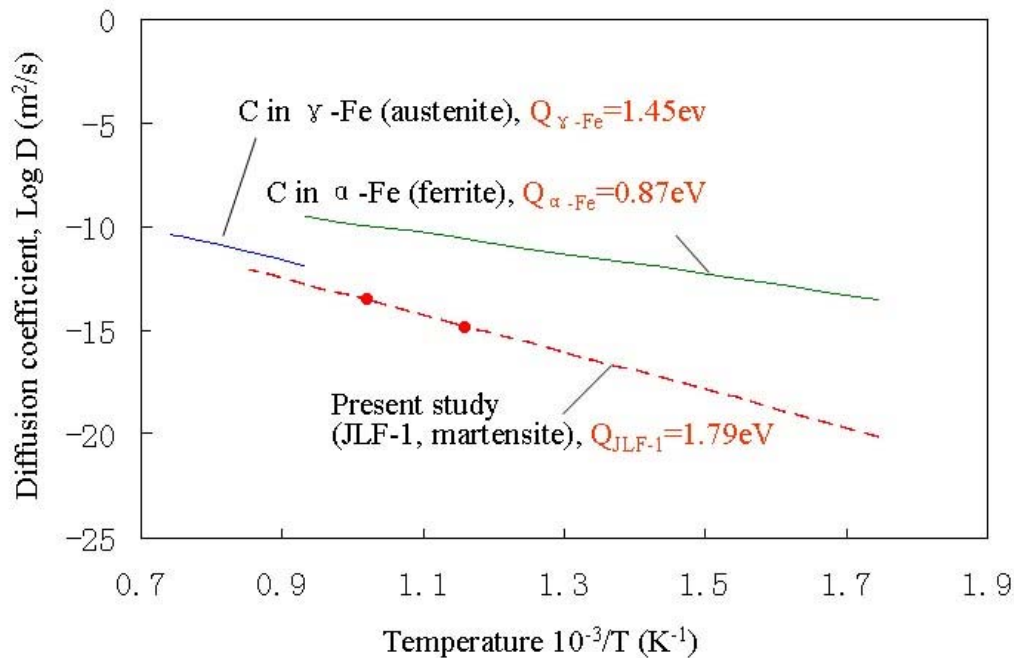Figure 6.3-5 Diffusion coefficient of C in JLF-1, α-Fe and γ-Fe

The diffusion coefficient is lower and the diffusion activation energy is higher for C in JLF-1 than those for C in α-Fe and γ-Fe. Trapping sites in martensite structure may suppress the diffusion of C. Possible trapping sites are dislocation, precipitates, lath boundaries and carbon vacancies in martensite phase. The effective trapping energy is estimated to be 0.92eV (1.79eV (Martensite)-0.87eV (Ferrite)).

6.4 Behavior of Ni in corrosion system

It is well known that Ni has high solubility in Li, as shown in Fig 1.4-3. According to the figure, the solubility of Ni increases with temperature in Li. At the same temperature, the solubility of Ni is much higher than other alloy constituent elements, such as Cr and Fe.

In the current experiment, corrosion products of Ni were observed on the surface of the specimens after exposure in Li in both static and flowing conditions, as mentioned in the previous chapters. The Ni corrosion products were shown in Fig.6.3-6. According to the figure, more Ni particles are found on the specimen surface at 700ºC than 600ºC. Almost no Ni particle was observed at 500ºC. Ni particle in SUS316 (Fe-Cr-Ni) container is larger than that in other cases. After loop test, the specimen exposed in cold leg of the loop was covered by Ni enriched layer. This layer may protect the JFL-1 specimen from further corrosion.
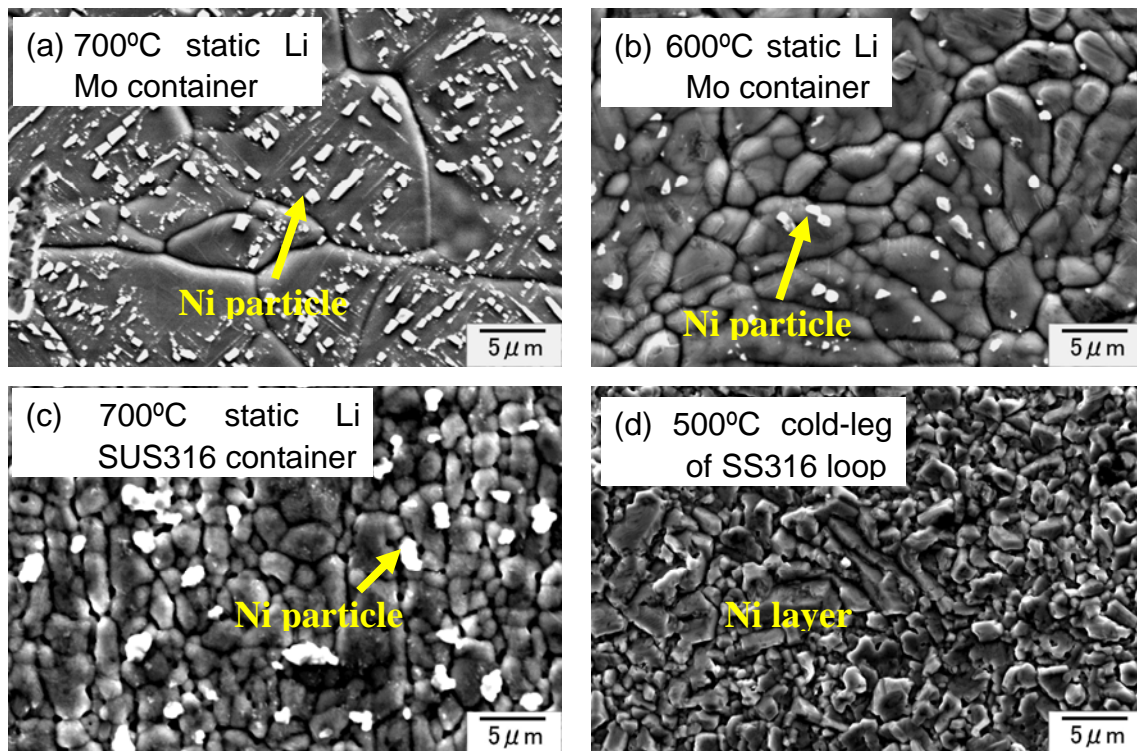

Figure 6.3-6 Ni corrosion products on specimens exposed in (a) Mo container at 700ºC; (b) Mo container at 600ºC; (c) SUS316 container at 600ºC; (d) cold leg of SS316 loop

at 500ºC

In the static tests in Mo container, the possible source of Ni may come from the SS316 spoon which is used to clean the melted Li before experiment. But the Ni dissolving from spoon seems to be limited because the contacting time is quite short. When SUS316 container was used as container, the austenitic steels containing large amount of Ni was the main source of Ni. During the cooling procedure in static exposure, the Ni dissolved in Li deposited on the surface of specimens.

In the flowing condition, migrant of Ni is more complicated than that in static exposure. The behavior of Ni in the loop can be described as figure 6.3-7. In the high temperature part, hot-leg, the alloy elements dissolved from the loop materials (SS316L, Fe-Cr-Ni) and the specimens into Li during the operation. Because of high solubility of Ni in Li, more Ni dissolved into Li than other elements. When Li flowed from hot-leg to cold-leg, the alloy elements precipitated on the surface of the specimen and the loop because of the reduction of solubility at low temperature.
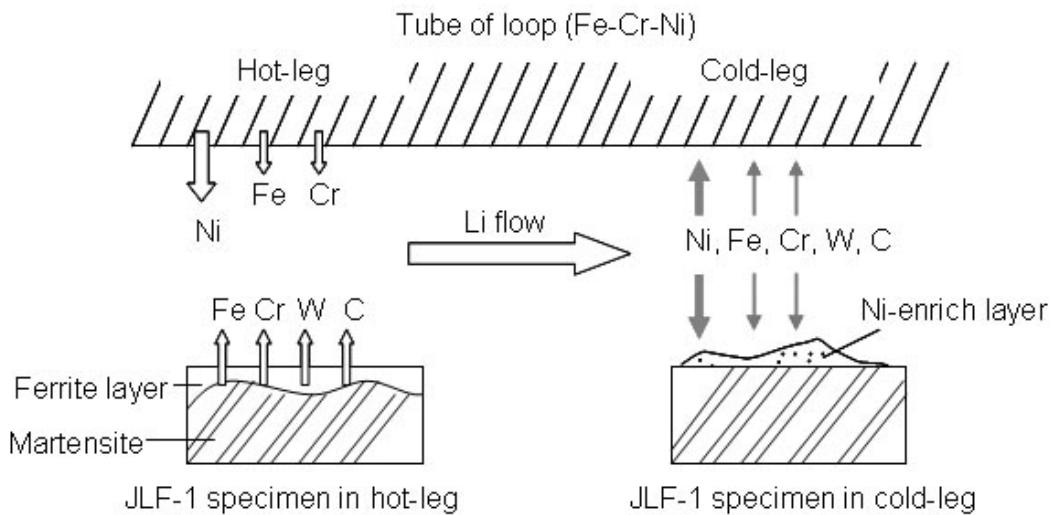

Figure 6.3-7 the transfer of Ni in loop

6.5 Summary

(1) The high N level measured in Li may be the main reason for significant corrosion of JLF-1 after exposure at 700°C.

(2) The formation of Mo particle on the surface of specimens and holder exposed in Mo container indicates that the Mo is soluble in Li when non-metal elements, such as N and C, exist. Mo particle on the surface of the specimen causes underestimation of the weight loss.

(3) The level of C in Li determines the phase transformation.

- In the static Li test, C trapping by the container surface reduces C level in Li and enhances the phase transformation.

- Diffusion of C in the materials controlls the extension of the phase change region.

- The dissolution model and comparison with the experiment suggests that (a) The extension of C depletion zone in the material obeys parabolic law and (b) The diffusion of C in JLF-1 is slower than that in α -Fe and γ -Fe

(4) Because of high solubility in Li, Ni was observed on the surface of specimens exposed in both static and flowing condition. In the flowing condition, the large amount of Ni precipitated in cold-leg and formed Ni enriched layer due to the mass transfer effect.

Chapter 7

Comparison with previous data

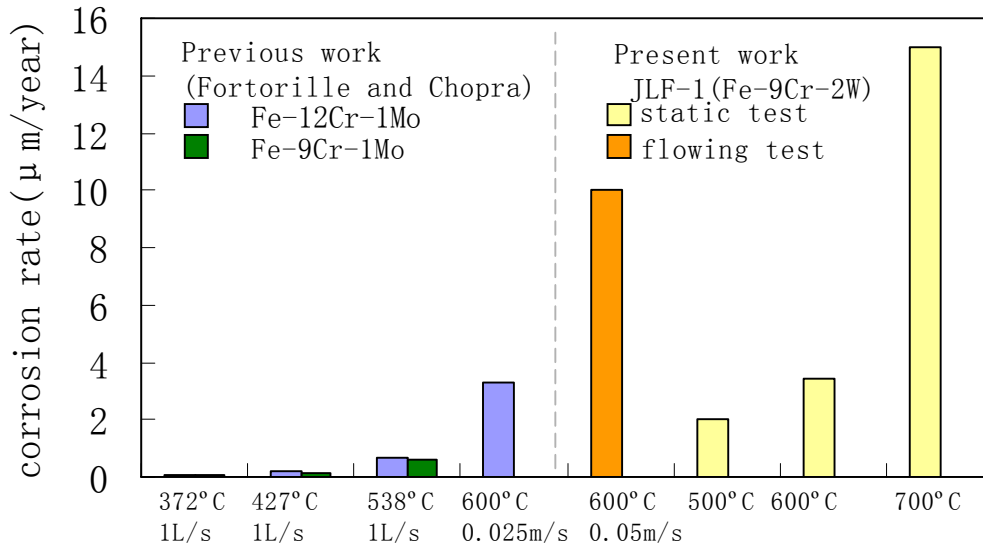## 7.1 Compare to the conventional ferritic steels in Li

Figure 7-1 Comparison of JLF-1 and ferritic steel in Li

The corrosion behavior of RAFM steel, JLF-1, was investigated in the static and the flowing conditions in the current work. The results were compared to the previous research on conventional ferritic steel in Li, [39,40,41,56] as shown in Fig. 7-1. According to the figure, the corrosion of JLF-1 seems to be more significant than the traditional ferritic steels. It was found that the corrosion rate increased with temperature during exposure in Li for both JLF-1 and the ferritc steels. Especially, the JLF-1 suffered from severe corrosion when it was exposed in Li at high temperature (700ºC). In both cases, the corrosion occurs by dissolution of alloy elements, such as Cr and Fe into Li. No protective layer was observed in the current and the previous work. It seems that the corrosion mechanism of steels in Li is mainly related the solubility of different alloy elements, when the effect of non-metallic elements such as O and N is small. As shown in Fig. 7-1, the corrosion of ferritic steel Fe-12Cr is higher than Fe-9Cr at different temperature. Also, it was shown in this work that the weight loss of JLF-1 is higher than that of Fe-Cr and pure Fe after exposure in Li under the same condition. This indicated that the steel containing more Cr and W may suffer more from the Li attack, because the solubility of Cr and W is higher than Fe.

Impurities, especially N, have strongly impact on the corrosion behave of conventional ferritic steels by forming ternary chemical compounds.[46-48, 51] The chemical reaction between N, Li and alloy elements can promote the corrosion of steels. In this work, when N level in Li increased from 60ppm to 650ppm, the corrosion rate of JLF-1 in static test increase more than one order of magnitude. This result agrees with the previous research on ferritic steel.[41,46-48]

6.5.2 RAFM steel in Li and Pb-Li

Fig. 7-2 is an estimation of corrosion rates of RAFM in Pb-Li predicted by Sannier based on different corrosion tests in Pb-Li and some modeling. [72] This figure shows the dependence of metal loss for the flow rate of 0.3, 0.05 m/s and 0.005 m/s. The last one represents nearly static conditions. The prediction based on the experimental data of the current work is inserted into this diagram. The closed circle represents the predicted corrosion of JLF-1 specimen after a year assuming constant corrosion rate. The open circle shows the predicted depth of phase change for a year assuming parabolic growth.

The figure shows that the all RAFM corrosion is sensitive to temperature in both Li and Pb-Li. With the increase in temperature, the corrosion of RAFM steel increases. At around 700ºC, significant corrosion is found in Li and Pb-Li. The severe corrosion at high temperature in Li may be due to the increase of N level. However, at relatively low temperatures, RAFM steels show more serious corrosion in Pb-Li than in Li. This indicates that the Li may be less corrosive to RAFM than Pb-Li once the N level is kept low.

The phase change from martensite to ferrite was observed only in the case of Li exposure. It was shown in this study that the dissolution of C was caused by the Li attack. The low Li activity in Pb-Li may be one of the reasons that no phase change was found on RAFM exposed in Pb-Li. It should be noted that the weight loss of RAFM steels with time usually obeys the linear in liquid metal, but the extension of phase change layer follows parabolic law. That means the development of phase change will slow down after long time exposure, comparing with weight loss.
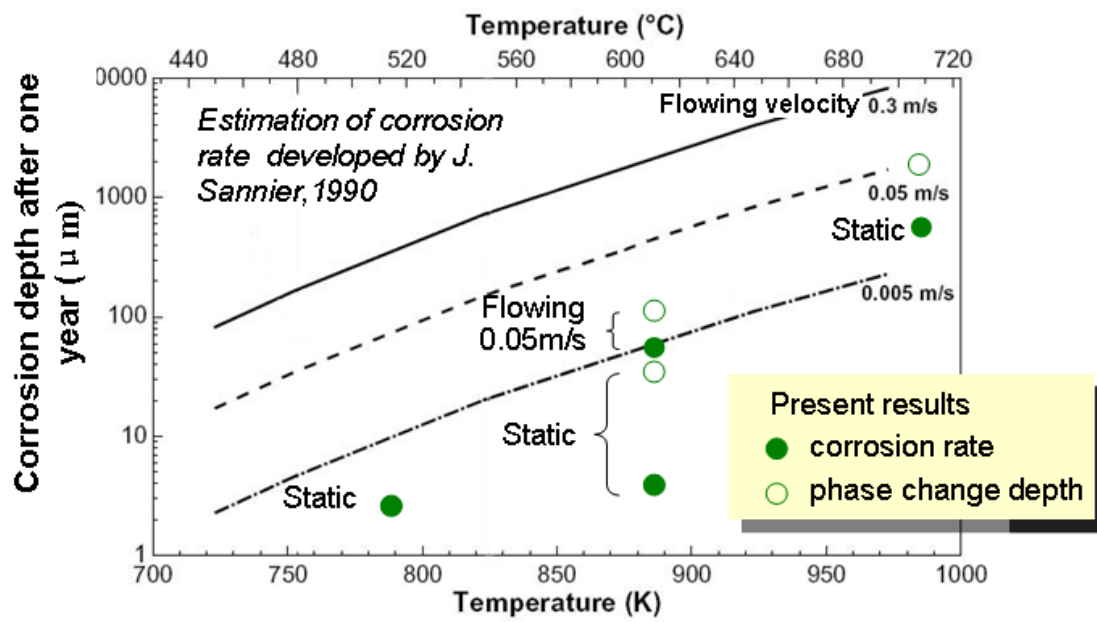
Figure 7-2 Corrosion behavior of RAFM in Li and Pb-Li

Chapter 8

Conclusion

The purpose of the present study is to examine the compatibility of RAFM steels with liquid Li with respect to corrosion rate and the degradation of mechanical properties and to clarify the underlying mechanism based on the element transfer and change of microstructure during the corrosion process.

For this purpose, a Japanese candidate RAFM steels, JLF-1, was chosen as the experimental materials. A series of static exposure tests were carried out at different temperatures for various exposure times to study the weight loss kinetics. The effect of alloy composition was investigated by comparing the corrosion behavior of JLF-1, Fe-9Cr and pure Fe. The static exposures in different containers were performed to find out the effect of container materials on corrosion. The flowing experiment was carried out in a loop to study the mass transfer and influence of flowing Li.

The conclusions of the present study are:

RAFM steel suffers the corrosion and phase transformation from martensite to ferrite by exposure in liquid Li

The driving force of corrosion is the level of Fe and Cr in Li. Saturation of the corrosion products in Li results in the suppression of corrosion. However, production of N, Li and the alloy element is the main driving force of the corrosion when N level in Li is high.

The loss of C leads to the phase change from martensite to ferrite and results in degradation of mechanical properties. The driving force of the decarburization is the level of C in Li. The trapping of C by the container materials can enhance the decarburization and the phase transformation. The extension of the phase transformation zone is controlled by C diffusion in the materials.

Flowing Li reduces the level of Fe, Cr and C in Li near the specimens and enhances the corrosion and phase transformation.

Limited comparison of the corrosion data with Li-Pb suggests that the corrosion rate of RAFM in Li may be lower than that in Li-Pb once the level of N in Li is kept low.

Reference

[1] IEA "Key World Energy Statistic"(2007)

[2] D. L. Klass, Energy Policy, 31 (2003) 353－367.

[3] Karine Fiore, "Nuclear energy sustainability: Understanding ITER", Energy policy 34 (2006) 3334-3341

[4] Yolanda Lechon, et al., "A global energy with fusion", Fusion Eng. Des.,75-79 (2005) 1141-1144

[5] J. Ongena, G. Van Oost, "Energy for Future Centuries - Prospects for Fusion Power as a Future Energy Source", Fusion Science and Technology 49 (2006) 3-15

[6] The promise of fusion energy, http://fusioned.gat.com/images/pdf/promise_of_ fusion. pdf.

[7] Zhenyu Yao, Doctor thesis 2005, The Graduate University for Advanced Studies.

[8] C. Neumeyer, P. Heitzenroeder, C. Kessel, et al, Fus. Engin. Des. 66-68 (2003) 139-145.

[9] M. D. Williams, Fus. Engin. Des. 36 (1997) 135-142.

[10] E. Bertolini, Fus. Engin. Des. 36 (1997) 119-133.

[11] J. P. Sharpe, P.W. Humrickhouse, C.H. Skinner, et al, J. Nucl. Mater. 337-339 (2005)1000-1004.

[12] Y. Shimomura, Fus. Engin. Des. 81 (2006) 3-11.

[13] E. Di Pietro, R. Andreani, D. Maisonnier, et al, Fus. Engin. Des. 81 (2006) 59-67.

[14] L. G. Golubchikov, V. A. Evtikhin, J. Nucl. Mater, Volumes 233-237, Part 1, 1 October 1996, Pages 667-672

[15] D.Ciazynski, Fusion Engin. Des. 82(2007)511-520.

[16] R. Aymar, J. Nucl. Mater. 307-311 (2002) 1-9

[17] M. Seki, M. Guseva, G. Vieider, et al, J. Nucl. Mater. 179-181 (1991) 1189-1192

[18] T. Muroga, T. Tanaka, S. Sagara, Fus. Engin. Des. 81 (2006) 1203-1209.

[19] L.V. Boccaccini, L. Giancarli, G. Janeschitz, et al, J. Nucl. Mater. 329-333 (2004) 148-155.

[20] M. Enoeda, M. Akiba, S. Tanaka, et al, Fus. Eng. Des. 81 (2006) 415-424.

[21] F. Najmabadi, Fus. Engin. Des. 41 (1998) 365-370.

[22] K. Ehrlich, E.E. Bloom, T. Kondo, J. Nucl. Mater. 283-287 (2000) 79-88.

[23] D. L. Smith, C. C. Baker, D. K. Sze, et al, Fus. Tech. 8 (1985) 10-44.

[24] M. Nagura, Mater thesis, 2008, Tokyo University.

[25] Zaixin. Li Doctor thesis, 2007. The Graduate University for Advanced Studies.

[26] T. Muroga, M. Gasparotto, S.J. Zinkle, Fus. Engin. Des. 61-62 (2002) 13-25.

[27] Jiming Chen. Doctor thesis. 2005, The Graduate University for Advanced Studies.

[28] R. L. Klueh, D. R. Harries, High-Chromium Ferritic and Martensitic Sttels for Nuclear Application, ASM Stoch, Number: Mono 03.

[29] R.L. Klueh, D.J. Alexander, J. Nucl. Mater. 233-237(1996) 336-341.

[30] A. Kohyama, A. Hishinuma, D.S. Gelles, R.L. Klueh, W. Fus. Engin. Des. 41 (1998) 1–6

[31] R.J. Kurtz, K. Abe, V.M. Chernov, V.A. Kazakov, G.E. Lucas, H. Matsui, T. Muroga, G.R. Odette, D.L. Smith, S.J. Zinkle, J. Nucl. Mater. 283-287 (2000) 70-78.

[32] S.J. Zinkle, H. Matsui, D.L. Smith, A.F. Rowcliffe, E. van Osch, K. Abe, V.A. Kazakov, J. Nucl. Mater. 258-263(1998) 205-214.

[33] T. Muroga, T. Nagasaka, A. Iiyoshi, A. Kawabata, S. Sakurai, M. Sakata, J. Nucl. Mater. 283-87 (2000) 711-715.

[34] R. H. Jones, C. H. Henager, Jr.G. W. Hollenberg, J. Nucl. Mater, 191-194 (1992) 75-83.

[35] L. Giancarli, V. Chuyanov, M. Abdou, etc. J. Nucl. Mater. 367–370 (2007) 1271–1280

[36] T. Muroga and M. Gasparotto, Fus. Engin. Des. 61-62, 13-2 (2002).

[37] Y. Kim and B.G. Hong, Fus. Engin. Des. 1067–1070 (2005) 75–79

[38] S. Malang , R. Mattas, Fus. Engin. Des. 27 (1995) 399-406

[39] O.K Chopra and Tortorelli J. Nucl. Mater 122 & 123 (1984) 1201-1212

[40] F.Tortorelli, J. Nucl. Mater. 155–157 (1988) 722–727.

[41] O.K. Chopra and D.L. Smith, J. Nucl. Mater 133&134 (1985) 861-866

[42] P. F. Tortorelli and J. H. Devan, J. Nucl. Mater. 85 & 86 (19791 289-293.

[43] D. G. Bauer,. W. E. Stewart, I. N. Sviatoslavsky, and D. K. Sze, Proc. Second Intl. Conf. on Liquid Matal Technology in Energy Production, U.S. Deaprtment of Energy Report CDNF-800401-P2 (1980) pp. 13.73-13.81.

[44] G. A. Whitlow, W. L. Wilson, W. E. Ray, and M. G. Down, J. Nucl. Mater. 85-86 (1979) 283-287.

[45] P.F. Tortorelli and J.H. DeVan, Proc. Topical Conf. on Ferritic Alloys for Use in Energy Technologies (1983), CONF-830659-1.

[46] J. M. McKee, United Nuclear Corp. (USA) Report NDA-40 (1957).

[47] F. Casteels et al., Trans. 5th Intl. Conf. Structural Mechanics in Reactor Technology, Vol. N. (North-Holland, Amsterdam, 1979), paper N2.5/3.

[48] D. L. Olson, G. N. Reser, and D. K. Matlock. Corrosion (Houston) 36 (19801 140-144.

[49] E. Rued1 and T. Sasaki, J. Nucl. Mater. 116 (1983) 112-122.

[50] M. G. Barker, P. Hubberstey, A. P. Dadd, and S. A. Frankham, J. Nucl. Mater. 114 (1983) 143-149.

[51] R. J. Pulham and P. Hubberstey, J. Nucl. Mater. 115 (1983) 239-250.

[52] M.W. Leabenworth, R.E. Cleary, Acta Metall. 9 (1961) 519–520.

[53] A. Kimura, R. Kasada, A. Kohyama, etc. Fus. Engin. Des. 81 (2006) 909–916

[54] G. C. Burrow, M. G. Down, and C. Bagnall, J. Nucl. Mater. 103 & 104 (1981) 657-662.

[55] P.F. Tortorelli, J. Nucl. Mater. 103 & 104 (1981), 633-638

[56] O. K. Chopra and D.L. Smith, J. Nucl. Mater, 141-143 (1986) 566-570

[57] J. Konys, W.Krauss, Z.Voss, etc. J. Nucl. Mater 329－333 (2004) 1379－1383

[58] J. Konys, W. Krauss, Z. Voss, etc. J. Nucl. Mater 367－370 (2007) 1144－1149

[59] H. Glasbrenner, J. Konys, H.D. Rohrig, J. Nucl. Mater 283-287 (2000) 1332-1335

[60] G.Benamati, C.Fazio, I.Ricapito, J. Nucl. Mater 307－311 (2002) 1391－1395

[61] A. Kimura, R. Kasada, A. Kohyama, etc. Fus. Engin. Des. 81 (2006) 909–916

[62] M.G. Barker, V. COEN, H. KOLBE, J. Nucl. Mater 155-157 (1988) 732-735

[63] M.G. Barker and S.A. Frankham. J. Nucl. Mater, 107 (1982) 218-221

[64] P. F. Tortorelli, J. Nucl. Mater, 722-727 (1988) 155-157

[65] R.J. Pulham and P. Hubberstey, J. Nucl. Mater 115 (1983) 239-250

[66] Thermodynamic database MALT2, Kagaku Gijutsu-Sha, 2004

[67] Beskorovaynuy N.M., Yoltuhovskiy A.G. Structural materials and liquid metal heat-transfers. Moscow, Energoatomizdat, 1983.

[68] O.Yeliseyeva, A report presented at NIFS, Japan, 2007

[69] Metal Data Book, Japan Institute of metal, 1993, p21-22

[70] T. Sakurai, T. Yoneoka, etc. Fus. Engin. Des. 61-62 (2002) 763-768

[71] R.J.Pulham and P. Hubberstey, J. Nucl. Mater, 115, (1983) 239-250

[72] J. Sannier, T. Flament, A. Terlain, in: Proceedings of the 16th, Symposium on Fusion Technology, 3-7 September, 1990, London, UK, p. 901.

[73] E. Ruedl. V. Coen, T. Sasaki and H. Koble. J. Nucl. Mater, 122 & 123 (1984) 1247-1251

LIST OF PAPERS

1. Qi. Xu, T. Nagasaka, T. Muroga, Compatibility of Low Activation Ferritic Steels with Liquid Lithium, Fusion Science and Technology, 52 (2007) 609-612

2. Qi Xu, Masatoshi Kondo, Takuya Nagasaka, Takeo Muroga, Masaru Nagura,Akihiro Suzuki, Corrosion Characteristics of Low Activation Ferritic Steel, JLF-1, in Liquid Lithium in Static and Thermal Convection Conditions, Fusion Engineering and Design, accepted and to be published

3. Qi Xu, Masatoshi Kondo, Takuya Nagasaka, Takeo Muroga, Olga Yeliseyeva, Effect of Container Composition on Compatibility of RAFM Steel with Liquid Li, in preparation

LIST OF PRESENTATIONS

1. Qi Xu, Masatoshi Kondo, Takuya. Nagasaka, Takeo Muroga, Masaru Nagura, Akihiro Suzuki, Compatibility of Reduced Activation Ferritic Steels with Liquid Lithium, Annual meeting of Atomic Energy Society of Japan (AESJ), 2007, Nagoya, Japan

2. Qi Xu Masatoshi Kondo, Takuya. Nagasaka, Takeo Muroga, Masaru Nagura, Akihiro Suzuki, Takayuki Terai, Compatibility of Reduced Activation Ferritic Steels with Liquid Lithium (2), Annual conference of AESJ, 2008, Osaka, Japan

3. Qi Xu1, Masatoshi Kondo, Takuya Nagasaka, Takeo Muroga, Masaru Nagura3, Akihiro Suzuki, Compatibility of Reduced Activation Ferritic Steels with Liquid Lithium, The Eighth International Symposium on Fusion Nuclear Technology(ISFNT-8), 2007, Heidelberg, Germany

4. Qi Xu, Masatoshi Kondo, Takuya Nagasaka, Takeo Muroga, Masaru Nagura, Akihiro Suzuki, Metallurgical Study on Corrosion of Low Activation Ferritic/Martensitic Steel, JLF-1, in Liquid Lithium, 24th Annual Meeting of The Japan Society of Plasma Science and Nuclear Fusion Research (JSPF), 2007, Himeji, Japan

ACKNOWLEDGE